Thesis for the Master's degree in chemistry

Samaneh Etemadi

Catalytic investigations of zeolite based methanol to hydrocarbons catalysts

60 study points

DEPARTMENT OF CHEMISTRY
Faculty of mathematics and natural sciences
UNIVERSITY OF OSLO 05/2015

Acknowledgments

I am taking this opportunity to express my gratitude to all inGAP group for providing office and laboratory facilities, academic resources and all helpful advises during these two years of my master studies. I would also like to thank Sharmala Aravinthan for her technical support related to equipment and Gloria Bostick for her useful comments on the writing and structure of this thesis.

Special Thanks to my main supervisor Prof. Unni Olsbye for giving me an opportunity to explore catalysis world with a great help especially in the discussion part with her strong and in-depth knowledge in this field of expertise. She led many weekly progress meetings whereby we lived the project and walked step-by-step along the whole path together. I would like to thank my co-supervisor Prof. Stian Svelle and also like to express my gratitude and respect to Dr. Selene Hernandez who acted as my co-supervisor and thanks to her great patience at the beginning of the road.

My deepest appreciation is expressed to my dear husband Hossein who supported me throughout entire my studies emotionally and financially. Also thanks to my mother and father in Iran for their emotional support from far distances.

Samaneh Etemadi

University of Oslo

April 2015

Abstract

Methanol-To-Hydrocarbons (MTH) process is a very important step to produce a range of hydrocarbons such as fuel and olefins from various carbon sources. Various hydrocarbons can be obtained as the final products using different zeolite topologies and reaction conditions. The aim of this study is to make a quantitative comparison of the life time stability of the materials studied as MTH catalysts. Different zeolite structures (1D and 3D) with different acid density and surface area but similar acid strength were selected, characterized and tested in MTH reaction: H-ZSM-22, H-ZSM-23, H-Mordenite, H-IM-5, H-ITQ-13, H-Beta and H-ZSM-5. All the samples were tested with three different weight hourly space velocity (WHSV) at 400 °C and methanol partial pressure of 13 kPa. Product yields and selectivities were plotted for all these topologies and compared to previous tested structures.

All catalysts were active for methanol conversion and gave initially full methanol conversion but their lifetime varied considerably and decreased in the order of: ZSM-5 >> ITQ-13 >> IM-5 > ZSM-23 ~ Beta > ZSM-22 > Mordenite. In addition, the studied catalysts showed different products distribution which explained well with dual cycle model of the MTH reaction. In general, 12-ring zeolite (H-Beta and H-Moredenite) deactivated faster than 10-ring structures, with higher aromatic yields and lower C_{5+} aliphatics. 10-ring 1D zeolites, H-ZSM-22 and H-ZSM-23, showed comparable stability toward deactivation, producing mainly aromatic free C_{6+} fraction. Finally, 10-ring 3D zeolite structures: H-IM-5, H-ITQ-13 and H-ZSM-5 presented longer lifetime and almost equal values for aromatics, C_{5+} aliphatics and C_2. For the studied catalysts, higher acid density led to higher activity of arene-cycle versus alkene-cycle. During a non-selective deactivation, the catalyst surface area declined significantly over the tested samples. However, changing the feed rate did not affect the accessible surface area and coke content for the spent samples. A higher coke content has been found over the zeolite with larger channels, higher acid site density and larger surface areas.

The autocatalytic kinetic model has been applied on the experimental data for these catalysts, by plotting the catalyst lifetime to 50% conversion against the applied contact time. In that way, the deactivation constant and the critical contact time can be calculated while giving the same stability trends as the total conversion capacity data. The autocatalytic deactivation model was only valid for 10-ring zeolites (ZSM-22, ZSM-23, ITQ-13, IM-5, and ZSM-5). For 12-ring zeolites (Beta with 3D and Mordenite with 1D channel) the model could not predict the deactivation behavior.

Table of contents

List of symbols and abbreviations

MTH	Methanol-to-hydrocarbon
WHSV	Weight Hourly Space Velocity
TOS	Time on stream
1D	One Dimensional
SBUs	Secondary Building Units
CBUs	Composite Building Units
DPE	Deprotonation energy
DFT	density functional theory
TPD	Temperature programmed desorption
FT-IR	Fourier Transform Infrared
MTG	Methanol-to-gasoline
MTO	Methanol-to-olefins
SAPO	silicoaluminophosphate
hexaMB	Hexamethyl Benzene
PMB	Polymethyl Benzene
HTI	Hydrogen Transfer Index
BET	Brunauer-Emmett-Teller
SEM	Scanning Electron Microscopy
XRD	X-Ray Diffraction
TGA	Thermo Gravimetric Analysis
EDX	Energy-Dispersive X-ray

TPO	Temperature-programmed oxidation
CSTR	Continuously Stirred Tank Reactor
PFR	Plug Flow Reactor
GC	Gas Chromatography
FID	flame ionization detector
DME	Dimethyl ether
MeOH	Methanol
He	Helium

Chapter1: Zeolites in catalysis

1.1. Catalysis

A catalyst is any substance that can accelerate the reaction without being consumed. The rate of a reaction can be increased using catalyst. Although the catalyst increases the rate of a chemical reaction, the overall thermodynamics of the reaction will not be altered. The catalyst can be atoms, molecules, enzymes or a solid surface which might be in different or the same phase with surroundings. A catalytic reaction can be considered as a cyclic event that in the first step the reactants attach to the catalyst to have reactions which lead to form products, and then the formed products desorb from the catalyst surface to make it available for further reactions (see Fig. 1.1). Although the catalyst participates in the reactions by making bond to the products and reactants, however it becomes unchanged as the products and reactants release from it [1].

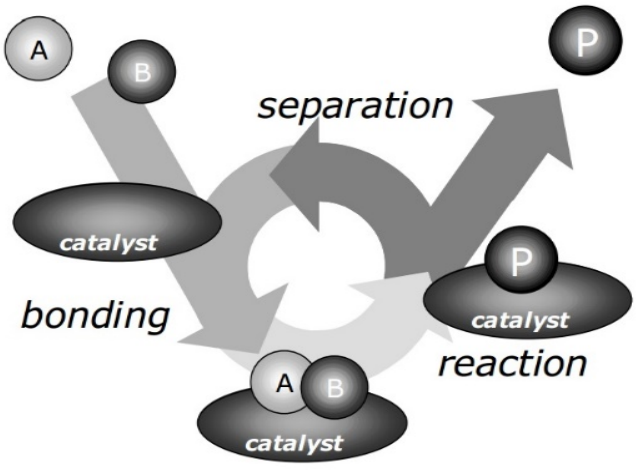

Figure 1.1: Elementary steps in a catalytic reaction: A and B as the reactants first bond to the catalyst surface and then after chemical reaction(s) which lead to product P, it desorbs from the surface to make it available for further reactions[1].

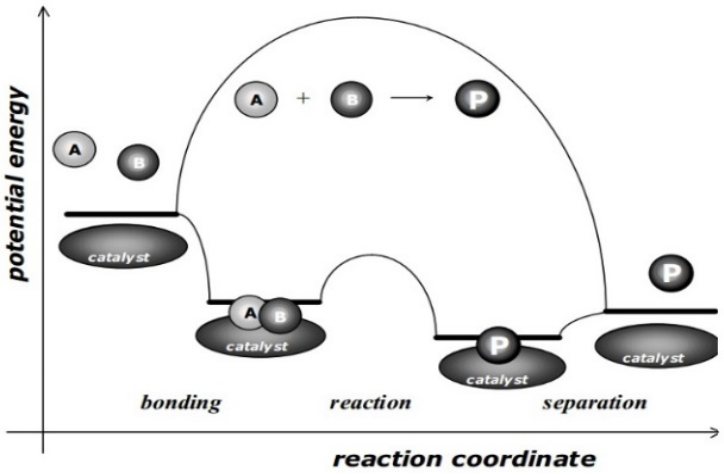

Figure 1.2: The potential energy diagram indicates lower energy path for a catalytic reaction (bottom path) compared to the non-catalytic reaction (top path). The catalyst lowered the energy by reducing the activation energy while the difference energy between the reactants and final product become unchanged [1].

Figure 1.2 shows the potential energy diagram which compares a catalytic (bottom path) and non-catalytic reaction (top path). As seen, the catalyst accelerates the reaction rate by reducing its activation energy. First both reactants (A and B) bond to the catalyst. As bond formation is always an exothermic reaction the potential energy decreases. In the next step the reaction between the adsorbed species occur. In order to have a reaction, the molecules should overcome the activation energy that is much lower respect to the energy barrier in non-catalytic reaction. Finally, the attached products will release from the catalyst [1].

If the catalyst and its reactants are in the same phase, they are categorized as homogenous catalyst. Whilst in heterogeneous catalysis, molecules in gas or solution are catalysed with a solid material. The reactants can diffuse into the inner pores of solid catalyst in case of porous materials such as zeolites or zeotypes, or can be adsorbed on the outer surface of non-porous catalyst (metal catalysts), while in both cases reactions are proceed on a catalyst surface. These types of the solid catalysts are widely used in industrial chemical and petrochemical processes.

1.2. Zeolites

Zeolites are well-defined crystalline structures in which $[SiO_4]^{-4}$ and $[AlO_4]^{-5}$ are connected together by sharing all oxygen atoms (see Fig. 1.3). Three dimensional framework structure

will be formed including various intra-crystalline cavities and channels in the molecular dimensions. The framework structure with linked cages, cavities and channels can accommodate molecules in and provide a pass way to diffuse compounds in and out of the zeolite structure. The size of each channel can be described as the number of Si or Al atoms (T-atom) in the ring as 8MR, 10MR and 12MR and assigned for small, medium and large pore sizes, respectively. Channels are one dimensional (1D), two dimensional (2D) or two dimensional (3D). In 2D channels, any point in a plane of pore system can be accessed from other points in the plane. Channels are called 3D, if each point in the pores system is approachable from any points within the crystal structure [2].

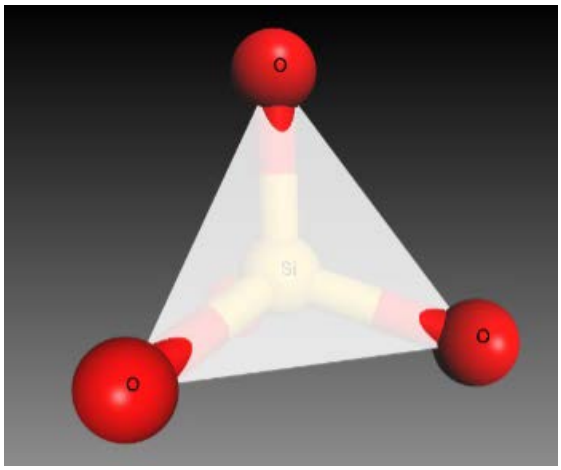

Figure 1.3: primary building unit of zeolite framework with Si, Oxygen and their connections.

The primary building units are simply TO_4 tetrahedral units as shown in Fig. 1.3. Connecting TO_4 tetrahedral up to 16 T-atoms can form the secondary building units (SBUs) as seen in Fig. 1.4. The framework structure can be assumed to build by only one type of SBUs (see Fig. 1.4). The SBUs consist of a single ring of 4, 6 and 8 tetrahedral called respectively as S4R, S6R and S8R. The SBUs can be arranged further in different unit types called Composite Building Units (CBUs) as depicted in Fig. 1.5. As representative examples of CBUs, various cages / cavities that repeated in several framework types are presented in Fig. 1.5. These subunits which are repeated in several topologies might be useful while comparing similarities between structures [2, 3].

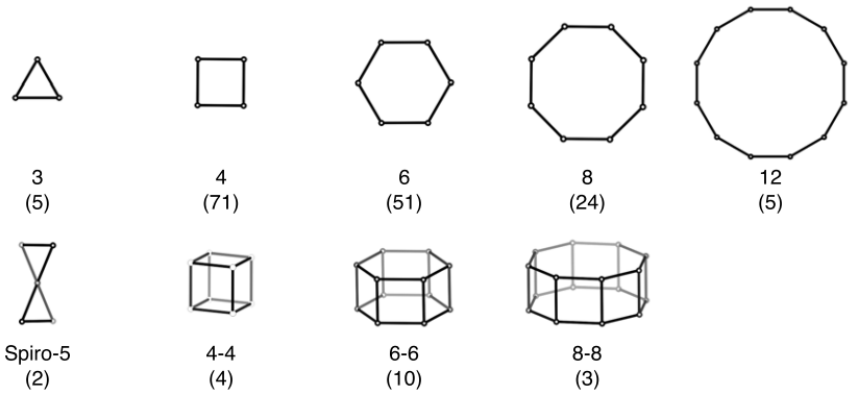

Figure 1.4: Secondary building units (SBUs) of zeolite framework structure [3]

Looking deeply into the zeolite structure, one can also distinguish characteristic chains besides polyhedral SBUs. Five different types of chains that can be created by mirror plane or centre of inversion are depicted in Fig. 1.6. These Tetrahedral, SBUs/ CBUs and chains build a huge three dimensional porous zeolite structure.

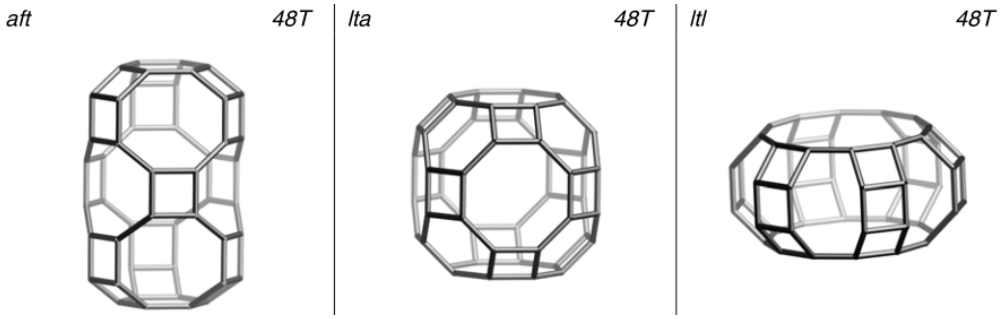

Figure 1.5: Various cages/cavities repeated in several frameworks as representative examples of Composite Building Units (CBUs) [3]

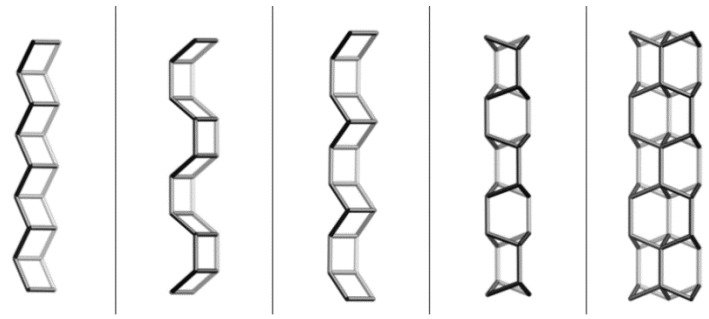

Figure 1.6: Selected Chains [3]

In case of presenting Al in the framework structure, in order to balance the total charge an extra-framework cation (i.e. K^+, Na^+) or proton located in pore space may be exerted. In the first case a weak Lewis acid site and in the latter a Brønsted site as shown in Fig. 1.7 will be form. The cations can be exchanged due to the high mobility and this property is giving rise to use zeolites as acid-base catalyst and ion-exchanged material [4].

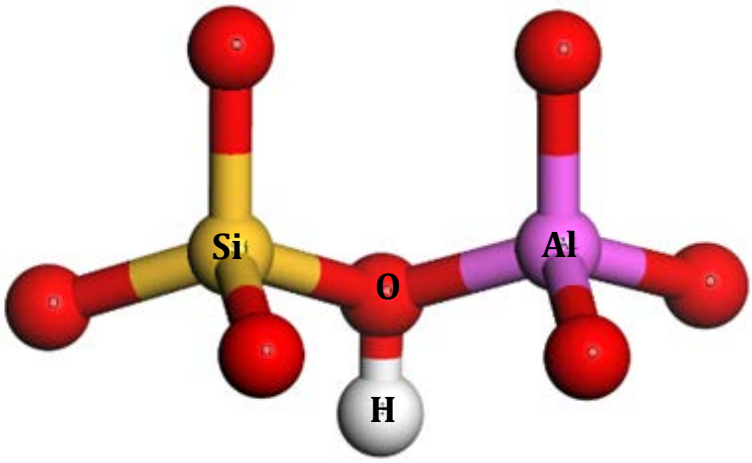

Figure 1.7: The bridged hydroxyl group, Si (OH) Al, called as Brønsted acid site in zeolite structure.

1.3. Zeolites covered in this study

As the purpose of this work is to study different topologies (1D and 3D channels with different ring sizes) in catalytic properties, it is vital first to dig into the framework structure and find the similarities as well as contrasts by comparing the cavities, pores and channels dimensions. Thus, 7 zeolites are grouped into 1D and 3D materials and will describe in details in the following sections.

1.3.1. 1D zeolites: ZSM-22, ZSM-23 and Mordenite

A three-letter code is assigned for each zeolite by International Zeolite Association [2]. For instance, MTT, TON and MOR named after ZSM-22, ZSM-23 and Mordenite respectively. MTT and TON structure with 1D and 10-ring channel differed slightly in shape and size of

the channel pore as depicted in Fig. 1-8. The TON (ZSM-22) channels are more elliptical while compared to the MTT teardrop-shaped channels where straight 1D channel with a small side pocket can be considered for MTT channels. Calculating the channel cross-section with two perpendicular diameter of the largest channel while assuming the perfect elliptical channel shape, showed a slightly lower value for MTT (18.4 $Å^2$) compared to TON (20.8 $Å^2$) as shown in Table 1.1. MOR structure consists of one dimensional 12-ring main channels (7.0×6.5 Å) with 8-ring side pocket (5.7×2.6 Å) as seen in Fig. 1.8. A high channel cross-section of 35.7 $Å^2$ are calculated for MOR as shown in Table 1.1 [5].

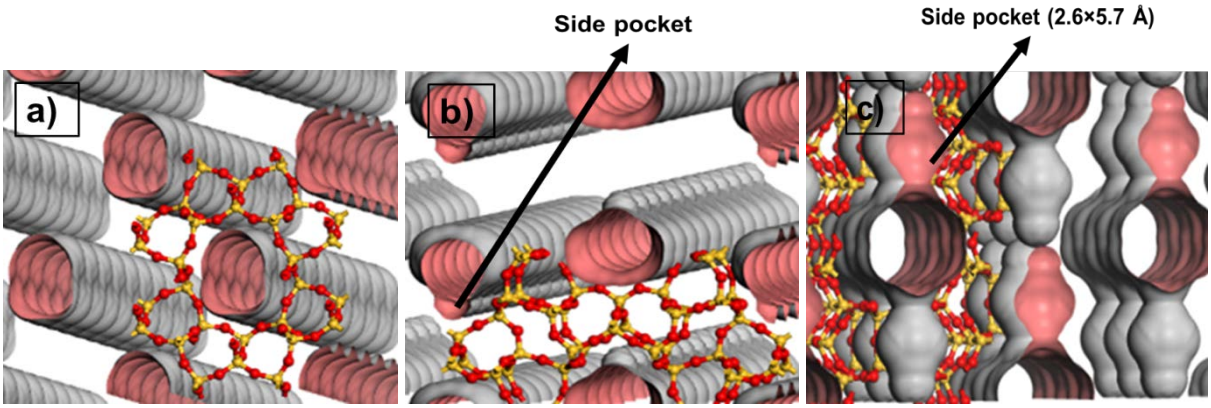

Figure 1.8: Illustrations of a) TON (ZSM-22), b) MTT (ZSM-23) and c) MOR (Mordenite) channels structure.

Table 1.1: Characteristics of 1D zeolites

Topology	Material	Channel size	Largest channel dimension (Å)	Cross section of channel $(Å)^2$	Side pocket	shape
TON	ZSM-22	10-ring	5.7×4.6	20.8	none	elliptical
MTT	ZSM-23	10-ring	5.2×4.5	18.4	very small	teardrop
MOR	Mordenite	12-ring	7.0×6.5	35.7	2.6×5.7 Å	elliptical

1.3.1. 3D zeolites: ITQ-13, IM-5, ZSM-5 and Beta

Fig. 1.9 depicts zeolite topologies and channel connections of IMF (IM-5), ITH (ITQ-13), *BEA (Beta) and MFI (ZSM-5) zeolites. All of these zeolites have three dimensional channels with 10-ring size for IMF, ITH and MFI and 12-ring channels for *BEA structure. IMF has connectivity of three 10-ring channels with slightly different in size as pictured in Fig. 1.9. ITH framework represents three sets of medium pore channel size of; two 10-rings with 4.8×5.3 Å and 4.8×5.1 Å dimensions which then connected to 9-ring channel with 4.0×4.8Å to build the 3D structure. This is the only zeolites reported till now that have 10 and

9-ring channels together [6]. Relatively large 12-ring pores with dual nature channels of (7.3×7.1 Å) and (5.6×5.6 Å) dimensions are present in BEA*(Beta). Such channel connectivity creates a disordered 3D porous structure (see also Table 1.2). MFI-type has two different sizes of 10-ring channels: zig-zag with almost circular cross-section and the straight channel with elliptical shape while all of intersections provided in the similar size.

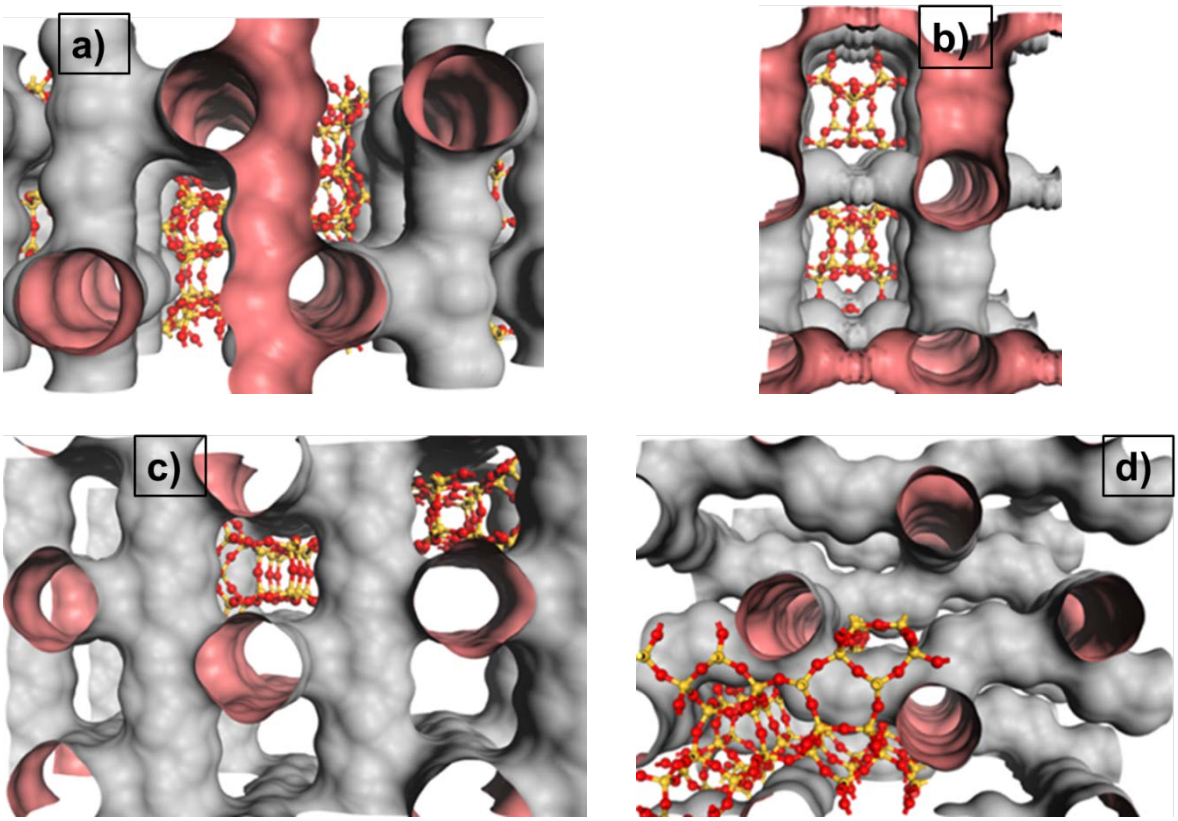

Figure 1.9: Illustrations of a) IMF (IM-5), b) ITH (ITQ-13) and c)*BEA (Beta) and d) MFI (ZSM-5) channels structure.

Table 1.2: characteristics of 3D zeolites

Topology	Material	Channel Dimension (Å)			Cross section of channel (Å)^2
ITH	ITQ-13	9-ring 4.8×4.8Å[100]	10-ring 4.8×5.1Å[010]	10-ring 5.3×4.8Å[001]	20
IMF	IM-5	10-ring 5.3×5.4Å[100] center 10-ring 5.1×5.3Å[100] Side	10-ring 5.3×5.9Å[010]	10-ring 5.5×5.6Å[001] center 10-ring 4.8×5.4Å[001] side	24.1
MFI	ZSM-5	10-ring 5.1×5.5Å[100]	10-ring (zig-zag) 5.3×5.6Å[010]	-	23.3
***BEA (polymorph A)**	Beta	12-ring 6.6×6.7Å<001>	-	12-ring 5.6×5.6Å[001]	34.7

1.4. The acidic property of zeolites

As described before, if a proton used as a charge balancing species in the framework, Brønsted acid site will be formed (Fig. 1.7). The solid acids and acidic zeolites have been appreciated as a catalytic cracking material in petrochemical processes. In zeolite material, two different acid sites can be found, Lewis and Brønsted sites. The Lewis sites are the electron pair acceptors and can interact with basic molecules by hydrogen bonding. These sites can be assumed as SiOH groups (or alkali cations) or unsaturated cations like Al^{+3} in extra framework structure as well as higher metal cations in exchanged positions [7]. The Lewis sites can be presented in the structure by ion exchanging or steaming process which creates aluminium extra-framework as a defect. The Lewis sites are more available in zeolites with very high Al contents or in the material that have had background of thermal/steam treatments [8].

The bridged hydroxyl group, Si (OH) Al (Fig. 1.7), with the capacity of exchanging the proton, is the typical Brønsted acid site. An ideal defect-free protonated form of zeolite has only Brønsted acid sites in the framework structure [9]. By choosing proper characterization techniques, it is possible to distinguish these two different acid sites (Lewis and Brønsted). The more emphasis in catalytic process has been on Brønsted than Lewis acid sites as it has been found a linear relationship between the concentrations of protonated tetrahedral aluminum in SiO_2 framework and the catalytic activity of aluminosilicate materials [10].

Although acid density and acid strength are two different properties, but sometimes both are called acidity property. The acid density in the aluminosilicate zeolites refers to the number of acid sites that is ideally equal to the number of substituted atoms in the lattice. The Si/Al ratio or equivalently SiO_2/Al_2O_3 is reversely proportional to the acid density [9]. The acid strength would be described as the intrinsic property of zeolite shown in presence of basic molecules. The main factor which determines the acid strength is the overall chemical composition of the framework structure, however some other parameters such as the exchanged metal cations and topology of the framework effects are minor [11]. In general the concentration of framework aluminum is directly proportional to the concentration of the acid sites and indirectly proportional to the acid strength. It was reported for zeolites (i.e. ZSM-5) with high Si concentration that the Brønsted sites show a uniform behavior in catalytic reactions such as isomerization and cracking. However, it is also shown that the acid density and acid strength are not totally independent terms. For instance, the same structure of zeolites (HX and HY)

with different Si/Al (ca. 1 and 3) shows stronger acid strength in lower acid density cases [11].

The required energy to separate a proton infinitely far away from the conjugated base is defined as deprotonation energy (DPE). Although this energy or enthalpy of deprotonation is theoretically (i.e. density functional theory) used as the value of intrinsic acid strength of zeolites, but it is rather difficult measurement in practice [9, 12]. Calculation of acid strength based on density functional theory (DFT) was claimed to be more accurate as it was not dependent on the stabilization of the base [9, 12]. Correlating the interaction enthalpy of the proton with probe molecules with the acid strength does not seem a proper basis due to its dependency on electrostatic stabilization of the ion-pairs.

There are various methods to identify the acid strength as well as the density of acid. Among them, the elemental composition of the zeolite is a recognized way to determine the acid density. However this method does not distinguish the framework and extra-framework acid sites in the material. The accessibility of the acid site also plays an important role in catalytic reaction. As another disadvantage, elemental analysis includes any potential defects in the framework structure while working out the elemental ratio [9, 12].

Temperature programmed desorption (TPD) is a technique to measure the acidic properties of a material (number and strength of acid sites). In this technique, chemisorbed probe molecules (as ammonia, NH_3-TPD) on the zeolite are slowly desorbed by increasing temperature. Acid strength of the zeolite can be evaluated by the temperature of desorption. Desorption peaks at low temperature indicate weak acid sites, while higher temperature peaks are due to stronger acid sites. The amount of desorbed NH_3 is used to calculate the number of acid sites. Similar to the previous method, there are some inaccuracies using this method. For instance, the probe molecules can interact strongly with Lewis acid sites and also another defects in the structure [9, 12].

In addition, Fourier Transform Infrared (FT-IR) with probe molecules (i.e. CO, pyridine) can be used to determine the acid sites. As the probe molecule is used, only the number of accessible acid sites can be obtained using such a procedure. FT-IR with a weak probe molecule such as carbon monoxide at a low temperature can be a good measurement of acid strength. The OH shift in the spectrum can be a good scale for comparing acid strength. The stronger the acid the longer the shift of OH band is [9, 12].

1.5. Shape selectivity concept in zeolites

Zeolites are very often used in shape selective catalysis. Indeed, the porous three dimensional framework of zeolite offer limited available space for molecules and species to diffuse in and out of the material. The topology is also responsible for restricted transition state formation, in which the formation of spacious species is avoided. Fig. 1.10 depicts three different shape selectivity types in zeolites as reactant shape selectivity, transition state and product shape selectivity. Reactant and product shape selectivity based on mass transfer limitations where the bulkier reactants and products are not allowed to go in or out of pores opening. In contrast, in transition state shape selectivity there is no possibility to form species which are bigger that the limited available space. Thus, only the intermediates which can fit in the pores will be formed [13].

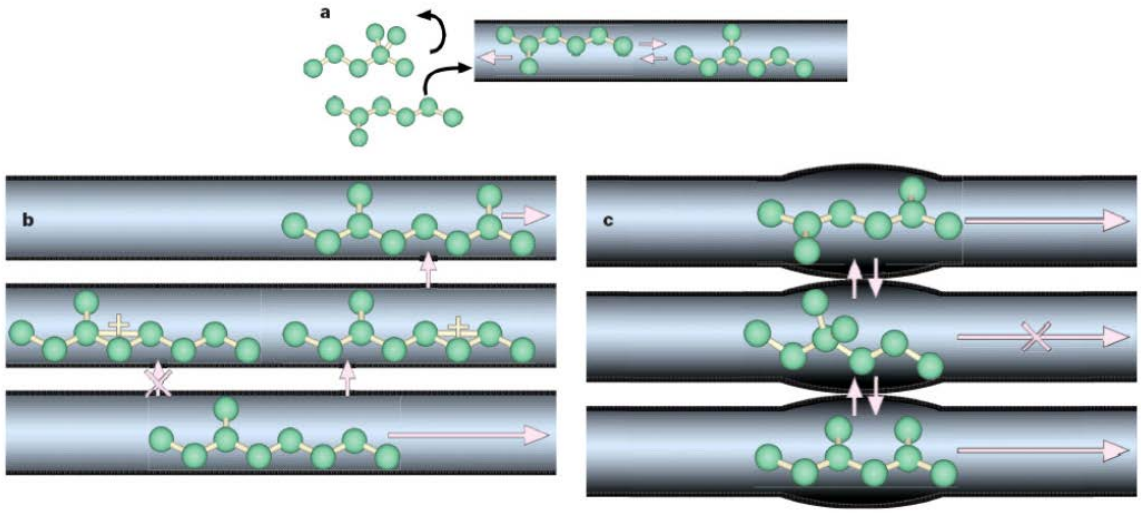

Figure 1.10: Illustration of a) Reactant b) transition state c) Product shape selectivity concept in zeolites [13]

Chapter2: Methanol- to- hydrocarbons (MTH)

2.1. Historical introduction

In the 1970s, two teams of Mobil scientists who were working on methylated isobutene to improve the octane number of gasoline using synthesized ZSM-5, accidentally discovered the formation of diverse hydrocarbons over this zeolite; later the process was called “methanol-to-gasoline (MTG)”. After that, Mobil’s central research tried to perform hypothetical reactions over ZSM-5 and this led to another discovery called “methanol-to-olefins (MTO)”. Several types of other zeolites were synthesized for MTG, MTO and MTH (methanol to hydrocarbons) process since then.

First and second oil crises between 1973 and 1978 were the driving force for commercializing MTG process. As the oil price was increasing, looking for other feed stocks such as natural gas, biomass or coal was crucial which could be converted via different pathways to fuel (gasoline and diesel), olefins and other hydrocarbon products (see Fig. 2.1). Mobil built a commercialized MTG plant in New Zealand, where natural gas converted to methanol first and subsequently methanol output was fed into producing high-octane gasoline. In 1986, silicoaluminophosphate (SAPO) was used in the process developed by Union Carbide to convert methanol to olefins. Further commercial development projects were stopped due to economic reasons as the oil price dropped significantly, however bench scale studies continued [14]. Table 2.1 depicts the historical root of MTH development.

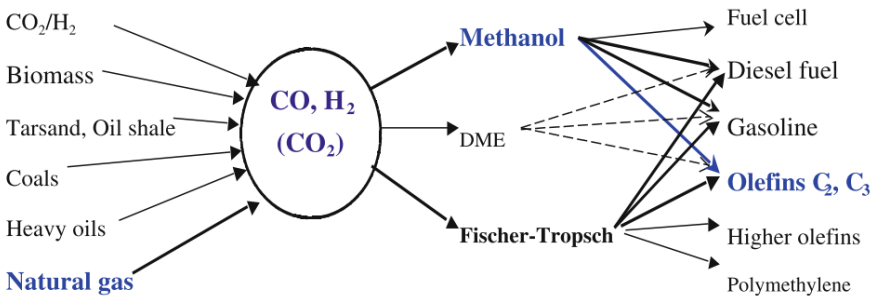

Figure 2.1: illustration of different feed stock used to form syngas (mixture of H2 and CO) which then can be converted into methanol and via catalysis process where zeolites involved in, form various hydrocarbon products [14]

Table 2.1: History of MTH process development [13]

Year	Developed by	Process	Statues
1981–1984	Mobil	MTG	Demonstrated on a 4 b/d plant in Paulsboro, NJ, USA.
1981–1984	Mobil	MTG	Demonstrated on a 100 b/d plant in Wesseling, Germany.
1985	Mobil	MTG	Commercialized in New Zealand (14500 b/d).
1980s	Haldor Topsøe	TIGAS[b]	A demonstration plant developed based on ZSM-5 (1 t/d).
2009	Shanxi Coal Institute	MTG	A demonstration plant brought on stream in Shanxi, province, China (100 kt/y).
2009	UOP/INEOS and Total OCP[a]	MTO	A semi-commercial demonstration unit built in Feluy, Belgium (10 t/d).
2010	CAC Chemnitz	STF	Currently in a demonstration phase syngas-to-fuel unit, developed in Germany.
2010	Haldor Topsøe	TIGAS	Currently being demonstrated in Des Plaines, USA, where a wood gasifier is running.
2010	Dalian Institute for Chemical Physics	DMTO[c]	A plant based on SAPO-34 started in Baotou, China (600 kt/y).
2010	Lurgi	MTP	First plant started in China (500 kt/y propene and 185 kt/y gasoline).
2011	UOP	Advanced MTO	Construction of a plant in Nanjing, China announced (295 kt/y).
2012	ExxonMobil	MTG	Announced a licensing agreement with Sundrop Fuels Inc. (3,500 b/d).
2012	UOP	Advanced MTO	Announced a licensing agreement with China's Jiutai Energy (Zhungeer) Co. Ltd. (600 kt/y).
2012	UOP	Advanced MTO	Announced a licencing agreement with Shandong Yangmei Hengtong Chemicals Co. Ltd. (295 kt/y)
2013	UOP	Advanced MTO	Announced a licensing agreement with Jiangsu Sailboat Co. Ltd. (833 kt/y)

2.2. Reaction mechanism

After Mobil's innovative method of using zeolites to convert methanol to hydrocarbons, several categories of studies carried out to understand the reaction mechanism. A variety of hydrocarbons such as heavy/light aromatics compounds, branched/unbranched alkenes and alkanes form via MTH reaction. It was found that the product selectivity depends on the zeolite framework structure used in the reaction as well as the processing condition in the MTH reaction such as pressure and temperature.

The simplest illustration of MTH reaction over the acidic zeolite can be seen as follows:

$$CH_3OH \xrightarrow{H^+} \text{"}CH_2\text{"} + H_2O$$

In which "CH_2" indicates to both aliphatic and aromatic compounds. The reaction initiated with equilibrium mixture of methanol, DME and water which then converted to hydrocarbons as shown in Fig. 2.2.

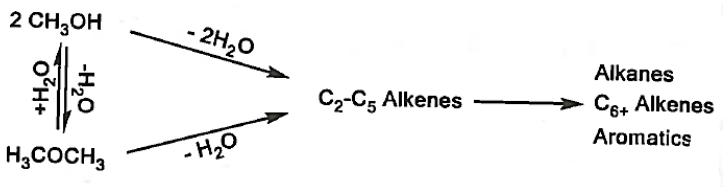

Figure 2.2: Simple illustration of the MTH reaction [15]

The earlier studies focused more on the possibility of direct C-C bond formation. However, it was proved to be less efficient as the result of further research works due to the high energy requirement for such formation. Although initiation of the "induction period" which leads to form the first hydrocarbons is still unclear, but the later works showed that the presence of low amount of organic impurities or trace of products increases the rate of the reaction and leads to an autocatalytic mechanism. Wei Wang and co-workers claimed that methoxy groups [SiO (CH_3) Al] formed by the equilibrium mixture of methanol and dimethyl ether play an important role in initial hydrocarbons. They also concluded that at the temperature above 523K, the surface methoxy group can react and form the first hydrocarbons even without any aromatic compounds [16].

MTH process is currently understood to be an indirect reaction in which intermediate hydrocarbons such as alkenes, aromatics or both are the central part of the process. First studies of MTH mechanism in 1980s of isotopic labeling and co-feeding studies over ZSM-5 zeolite performed by Dessau and coworkers from Mobil led to a proposed mechanism for the MTH reaction based on methylation and cracking of alkene intermediates. They suggested the autocatalysis mechanism for the reaction, without considering the reason of formation of first

alkenes. A small amount of alkene can be the starting point of autocatalytic reaction. In Dessau's mechanism, cyclisation and aromatization form the aromatic compounds which together with alkanes are the final products [17, 18].

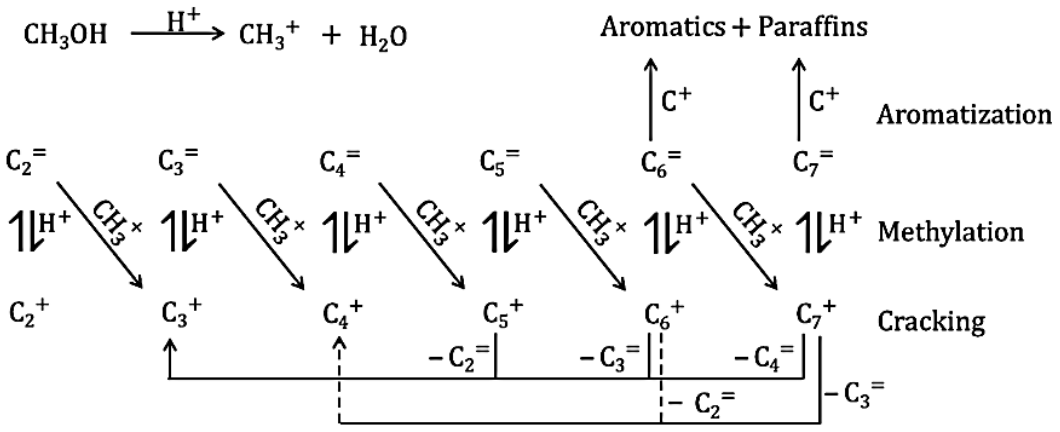

Figure 2.3: The MTH mechanism proposed by Dessau based on methylation and cracking of alkenes as the intermediates and aromatics and alkane as the final products [18]

High yield of isobutene formed by hydrocracking of hexamethyl benzene (hexaMB) led to paring mechanism proposed by Sullivan and coworkers [19] as depicted in Fig. 2.4 (left-hand cycle). They suggested a mechanism based on cyclic ring-contractions and expansions that is initiated from hexaMB and caused isobutene formation as a product [19]. Further works by Mole and coworkers gave rise to another cyclic mechanism in which exocyclic double bond reforms to ethyl side-chain which can be separated as ethene [20, 21] as illustrated in Fig. 2.4 (right-hand cycle). The main products in the paring cycle would be isobutene and propene, while in side-chain cycle ethene and propene can be found as the main products. Several isotopic labelling studies showed that in paring reaction a carbon ring contribute to the mechanism while it is not the case in side chain mechanism [22, 23].

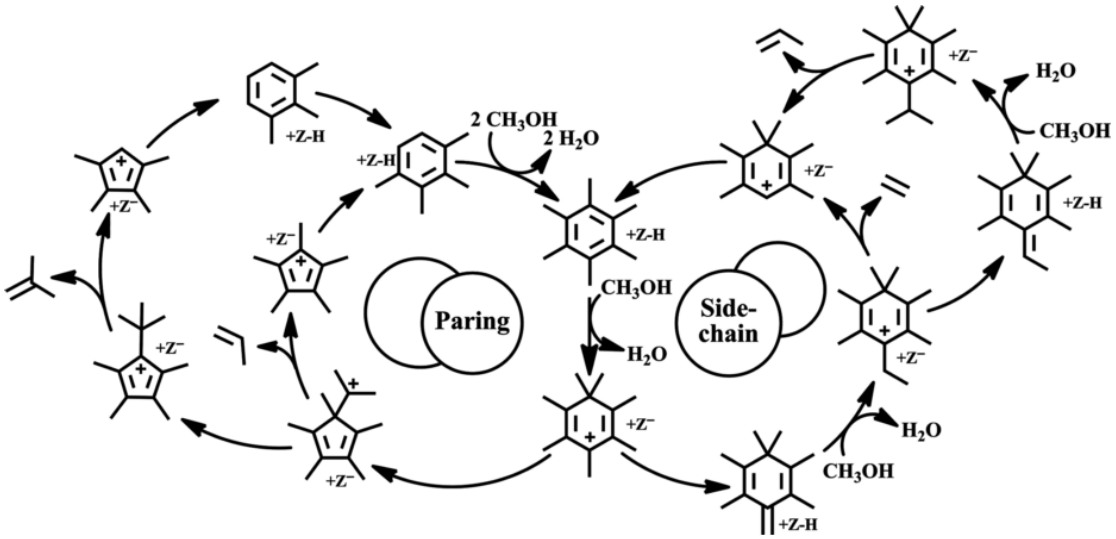

Figure 2.4: paring and side-chain mechanism proposed by Sullivan and Mole, respectively [24]

Co-feeding and isotopic labelling experiments over SAPO-34 done by Dahl and Kolboe proposed a new indirect mechanism named “hydrocarbon pool mechanism” in which unknown hydrocarbons called hydrocarbon pools were the central part of the MTH reaction. As can be seen in Fig. 2.5, the methanol added continuously to the adsorbed intermediate pools $(CH_2)_n$, which then convert to the final products such as ethene, propene, butane, aromatics and alkanes. Thus, the concept of hydrocarbon pool mechanism includes alkene, aromatics or other species as the intermediates [25].

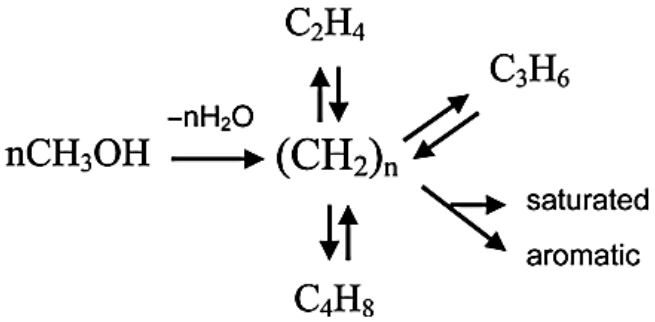

Figure 2.5: The hydrocarbon pool mechanism proposed by Dahl and Kolboe [25]

More studies over ZSM-5 revealed that although the methanol conversion can proceed via aromatic and alkene based cycle, but not all alkene can form via aromatic intermediates [26, 27]. The outcome of the studies led to the evolution of the hydrocarbon pool mechanism which was later called “dual cycle mechanism” as pictured in Fig. 2.6. This model suggests that either arena or alkene (or both) intermediates should be considered as hydrocarbon pools. The alkene cycle involved methylation/cracking reaction. In contrast to Dessua’s model, in this model a very small portion of ethene can be produced by alkene catalytic cycle. Due to the different special limitations, formed intermediates in each cycle vary over different zeolites topologies.

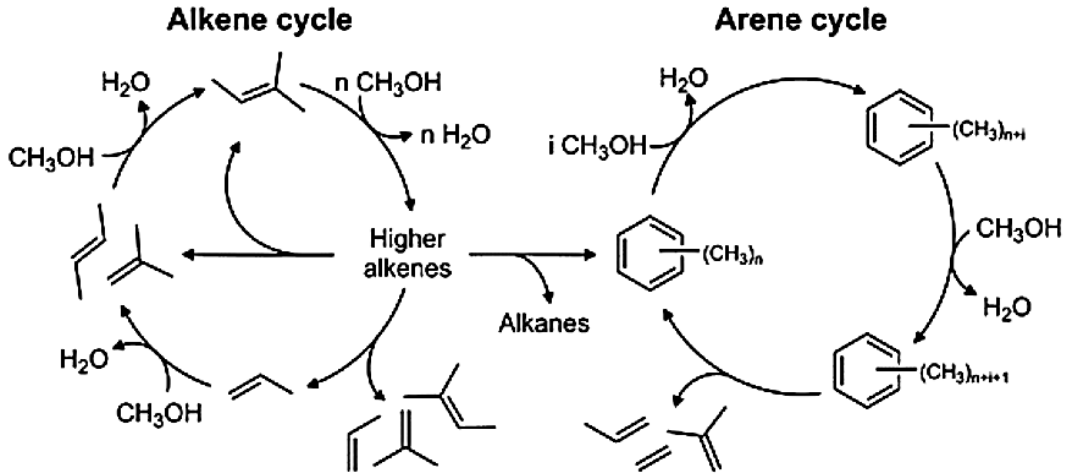

Figure 2.6: The dual cycle mechanism for the MTH reaction based on two intermediate cycles: alkene-cycle and arene-cycle. The alkene intermediates can convert to aromatic compounds via cyclisation and aromatisation which also produce alkane as product [24]

More spacious structures prefer the cycle with the aromatic intermediates as claimed by Svelle and Bjørgen et al. [28, 29] while studying the MFI and BEA* structures. In 2007, based on the studies over H-ZSM-5 and H-Beta, Svelle et al. proposed that penta- and hexamethylated benzene were the key aromatic intermediates in H-Beta, whilst less methylated benzene was more reactive in H-ZSM-5 in the same reaction conditions. In agreement with Haw et al. [30] they concluded that the less methylated aromatic intermediates favored the formation of ethene in arena cycle whereas higher polymeteylated benzene (penta- and hexa methylbenzene) favors propene. In addition, they concluded that higher alkenes form via mechanisms which are different from the ethane formation based on dual cycle module [28, 30].

Bjørgen et al. also confirmed that intermediate hydrocarbons pool in catalytic cycles can be affected by topological properties of zeolite. For instance, product selectivity and conversion per active site of catalyst are dependent on the zeolite topology as well as other factors such as reaction conditions. The hydrocarbon pool and PMBs were detected over H-ZSM-5 and H-Beta, and suggested that these intermediates are the key precursors for alkene formation. The relative rate of ethene and propene formation was terminated [29].

2.3. Coke formation and deactivation mechanism

During the catalytic reactions such as the MTh reaction, the catalysts become gradually deactivated with time-on-stream. There are several reasons for catalyst deactivation and can be named as: first, poisoning the active site by reactant, other impurities or by deposited carbonaceous species. Second, limitation to access to the active sites which can cause by carbonaceous deposited species or by extra-framework aluminum formed via dealumination. Third, deactivation due to altering the framework structure. Fourth, sintering which happens in metal supported catalysts [31-33]. Two main reason lead to deactivation of acidic zeolites can be categorized into: active site poisoning and pore blockage [31]. By irreversible adsorption of molecules on the active sites, these sites become poisoned. Since the zeolite channel sites are slightly larger than molecular dimensions, large molecules such as organic compounds or coke species can easily block the pores and deactivate the catalyst. Coke is referred to any carbonaceous species deposited on the surface of catalyst (internal and external) and limits its diffusion or masks the active sites [34-39]. As coke burn in air/oxygen flow, the catalyst activity can be recovered. Many studies have been devoted to this topic and approved that zeolite topology is more responsible in terms of coke formation [40-43].

Schulz and Wie studied the mechanistic coke formation over H-ZSM-5 at low (270-300 °C) and high temperature (400-500 °C). Two different mechanisms were proposed. At low temperature, long incubation and fast deactivation occurred, whilst slow deactivation without initiation period caused catalyst deactivation at high temperature. Composition analyses of both retained and volatile products proved that the specious retained materials that could not easily diffuse out at low temperature are the main reason of deactivation. However, in higher temperatures the external coke species block the pores opening and prevent the methanol molecules to diffuse in for further reactions. At low temperature, the decomposition energy

was not provided to break down the molecules, leading to blockage of the pores and fast deactivation while it is not the case in higher temperature [42].

The main reactions in MTH process over ZSM-5 leading to the volatile products and retained coke materials are summarized in Fig. 2.7 [42]. Alkylation/Dealkylation of aromatic rings (reaction 1 in Fig. 2.7) and dimerization/olefins cracking (reaction 2 in Fig. 2.7) are very important reactions to control the size of olefins in the hydrocarbon pool. Although the cracking probability depends on the stability of carbenium ion and its reactivity, but olefins with six or higher carbon contents favorably will undergo cracking reaction. The aromatic ring would form through cyclization and hydride transfer reactions (reaction 3&4 in Fig. 2.7). Less methylated compound can be found in equilibrium with higher methylated molecules according to reaction 5 of Fig. 2.7 [42].

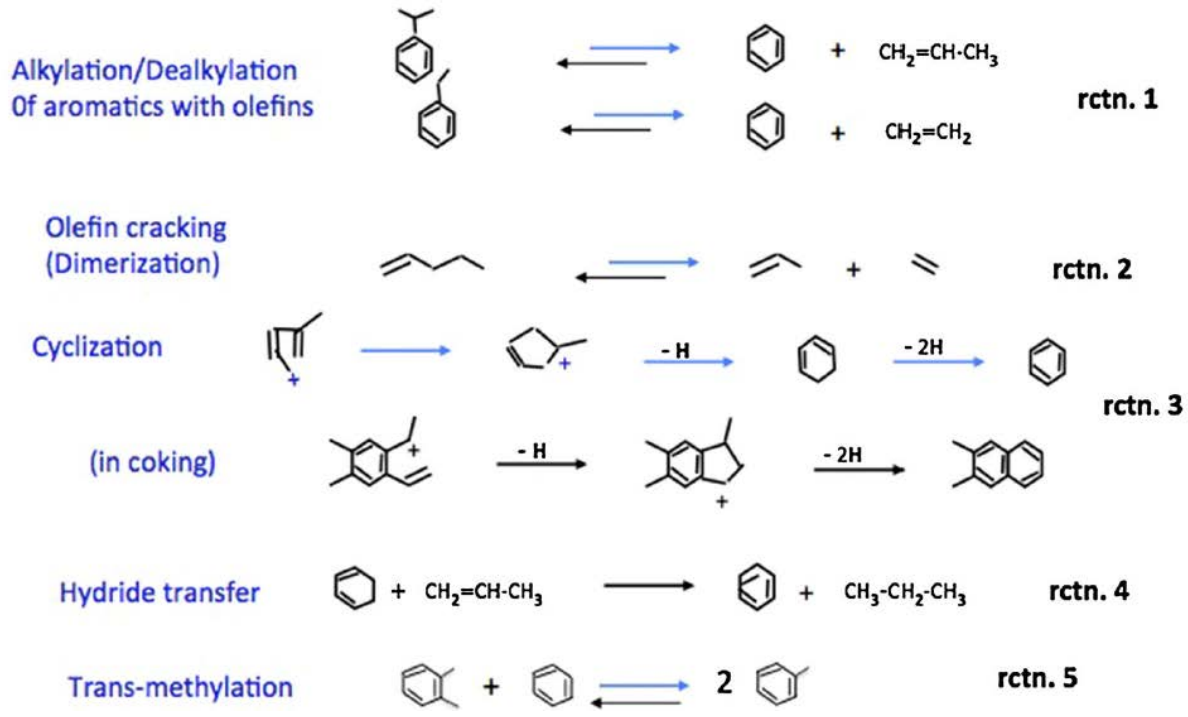

Figure 2.7: Main reactions during the MTH process over ZSM-5 proposed by Schulz and Wie[37]

Li and coworkers studied [44] the MTO reaction mechanism over ZSM-22 zeolite by ^{13}C labeling and computational modeling techniques. The retained material in the zeolite channels was computationally simulated. They suggested the deactivation mechanism of the blockage of the pores opening with the coke species. In fact the large transition-state intermediate could

not be the reason for deactivation due to the narrow one dimensional channel. In 2009 Janssens proposed a new model which was independent of the deactivation causes [40, 41]. This model is built on the observation that the product distribution over the catalyst life time is similar to the product distribution by changing the contact time. Therefore, he related the deactivation to reduced effective amount of catalyst or number of active acid sites with time on stream. The intrinsic activity of the acid sites will not change during the methanol conversion. A first order reaction for methanol conversion over H-ZSM-5 zeolite was assumed where the deactivation is proportional to methanol conversion. Considering various contact time for each zeolites, at a specific conversion level (50%) the lifetime will not depend on the catalyst activity when the initial conversion was close to 100%. Using this model, the deactivation coefficient and reaction rate constant can be calculated from the experimental data set.

In 2013 Janssens and coworkers [45] studied the deactivation modeling of catalysts and compared the theoretical models with the experimental data obtained from ZSM-5 and ZSM-22 during MTH reaction at 350 °C. A non-selective deactivation reported for the mentioned catalysts. In other words, the product distributions will not change with deactivation. The deactivation of catalysts was studied with two different models, autocatalytic and dual-cycle kinetic model. In autocatalytic deactivation kinetic model, the methanol conversion proceeds via an initiation step followed by an accelerating step with a faster rate constant compare to the first step. Therefore, the MTH reaction was assumed to be an autocatalytic and not a first order reaction as proposed in 2009. Plotting the lifetime to 50% methanol conversion versus applied contact time gave the deactivation coefficient and the critical contact time which might be different as the catalyst changes. The critical contact time can be defined as the required time to have enough concentration of hydrocarbons in which the autocatalytic reaction controls the reaction rate. The critical contact time would be constant for a given condition. The reaction between methanol and aromatic species (PMBs) in dual-cycle deactivation model, will lead to coke formation and finally deactivation of catalyst. The time which is needed to build up the hydrocarbon phase inside the channels at the beginning of the MTH reaction is called induction period. During the induction period the deactivation rate is not proportional to the methanol conversion. The dual-cycle model was used to predict the coke profile for partially deactivated catalyst [41].

Characterisation Part

Chapter3: Characterisation techniques

As the main goal of this work is to make a quantitative comparison of the life-time stability of different zeolites during Methanol-To-Hydrocarbons (MTH) reaction, this chapter is devoted to various methods and techniques used to get different characterization information on the zeolites which were subjected to MTH reaction. Thus, the primary aim of catalysts' characterization was to ensure about having the porous, well-crystalline structure with the desired phase. Secondary, identification of the varied parameters between these zeolites might be useful to interpret different catalytic performance during MTH reaction. In addition, characterization of the spent zeolites might give some clues to investigate more about deactivation.

Therefore, all 7 zeolites: H-ZSM-22, H-ZSM-23, H-Mordenite, H-IM-5, H-ITQ-13, H-Beta and H-ZSM-5 were characterized by a number of common techniques such as X-ray powder diffraction (XRD), scanning electron microscopy (SEM), surface area measurement based on: Brunauer-Emmett-Teller (BET) and t-Plot theory, Infra-Red Spectroscopy (FT-IR) and Thermo gravimetric analysis (TGA). While the characterization of all 21 spent catalysts together with three fresh samples were performed by the author, characterisation of the fresh H-ZSM-22, H-ZSM-23, H-IM-5 and H-ITQ-13 were performed in parallel master studies by S. Kwak [46].

This chapter is divided into three sections; Theory, Experimental and Results/Discussion parts. Note that only the characterisation results of the fresh zeolites will be shown in the results part while data related to the spent catalysts will come later in the following chapters.

3.1. Theory and Background

3.1.1. Powder X-ray Diffraction (XRD)

X-ray diffraction gives information about the lattice parameters of crystalline phases. Such information is achieved by high energy X-ray photons. X-ray beams can be produced by bombardment of a target with high energy electrons. If the incident electrons have enough

energy to make electrons of different shells excited, for instance K-shell electron, then the excited electron will eject and create an unstable vacancy. When an electron from L-shell (upper shell) jumped to K-shell (lower shell) to fill a core hole created by primary electron, a characteristic Cu K_α X-rays with 8.04 keV energy and 0.154 nm wavelength would be emitted. Elastic scattering of X-ray photons by atoms of an ordered lattice produces X-ray diffraction pattern according to Bragg's Law as follows:

$$n\lambda = 2d\,\mathrm{Sin}(\theta) \qquad \text{n =1, 2, 3, …}$$

Where n is an integer called as the order of the reflection, λ is the wavelength of the incident X-ray beam, d is the space between planes of the lattice and θ is the scattering angle [1].

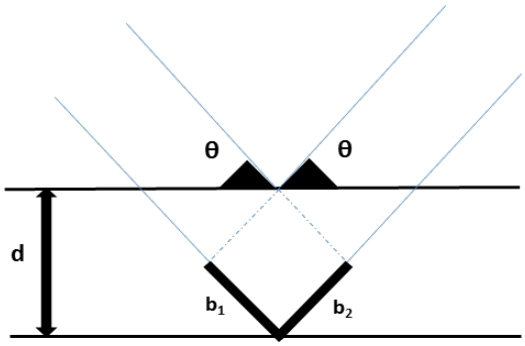

Figure 3.1: The constructive interference happens if the path differences between two diffracted beams (b_1+b_2) is the integer number of wavelength according to Bragg's Law [47].

Fig 3.1 shows the constructive interference of beams. The beams will have a constructive interference if the scattered beams are in the same phase meaning that the difference in their path length, sum of b_1 and b_2, is an integer number of wavelength (see Fig. 3.1 and Bragg's equation). The lattice space (d) which is the characteristic of crystal structure is determined using Bragg's Law and measuring the angle between scattered and incident beam.

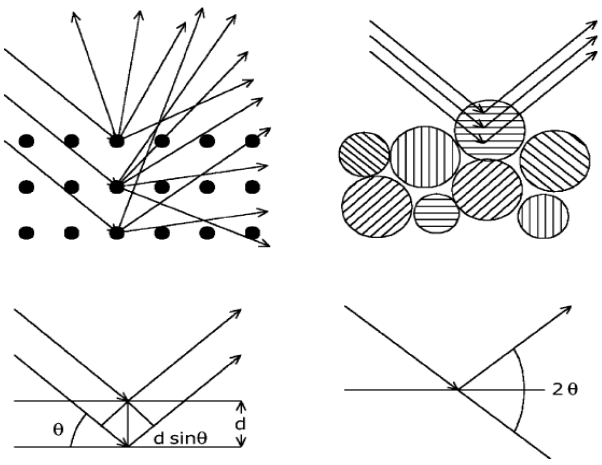

Figure 3.2: The constructive interference would be obtained if the beam diffracts according to the Bragg's law. In polycrystalline samples a small portion of crystals oriented such that a constructive interference could be achieved. If either sample or detector rotates during measurement a bigger portion of crystals contribute in the diffraction pattern **[1].**

Diffraction pattern can be obtained either for single crystal or powdered (polycrystalline) samples. In case of powdered sample X-ray source like Cu K_α with a rotating detector can be used to get diffraction pattern. With these samples, the beam would be constructively scattered from a small portion of crystal planes which randomly oriented at a correct θ angle, as shown in Fig. 3.2. Thus rotating either the sample or detector results in contribution of more crystals in diffraction pattern [48].

As zeolites can be rarely found in single crystal form, powder X-ray is mostly applied to obtain diffraction pattern for these materials [49]. For a known synthesized zeolite, it is possible to have a quality control of the structure by comparing the diffractogram with the computer-generated standard patterns from "The International Zeolite Association (IZA)" [50]. Therefore, the XRD pattern can be used as a fingerprint for different materials as well as zeolite structures [49]. Various crystallographic phases which are present in a material would be determined by comparing the peaks' position and intensity/width with the reference XRD pattern. A broad peak can be interpreted as a poor crystallinity, while narrow sharp peaks show well-crystalline structure. The peaks would be clearly visible if the material possesses a long-range order which could be a disadvantage of the XRD measurement.

From a diffractogram, the crystal size can be also determined considering the width and shape of peak according to Scherrer formula as follows [1]:

$$\langle L \rangle = \frac{K\lambda}{\beta \cos\theta}$$

Where:

$\langle L \rangle$ is dimension of particle perpendicular to the reflecting plane (in Å), λ is the wavelength of incident X-ray beam (in Å), K is a dimensionless shape factor that mostly consider as 1, β is the line broadening at half the maximum intensity named as FWHM (in Radian), and θ is the Bragg angle.

3.1.2. Scanning Electron Microscope (SEM)

Scanning electron microscopy (SEM) is one of the easiest and mostly used techniques to determine the morphology of a material [1]. The main parts of SEM instrument are illustrated in Fig. 3.3. Various sources such as single crystal/filament of tungsten or lanthanum hexaboride (LaB_6) can be used to produce a focused beam of electrons. Several lens used to make a tiny spot of the electron beam. After the beam passed through scanning coil/objective lens, the beam scan along the surface sample in a raster fashion [1]. The instrument operates under vacuum condition to avoid further collisions between electrons beam and gas molecules to preserve their energy [51].

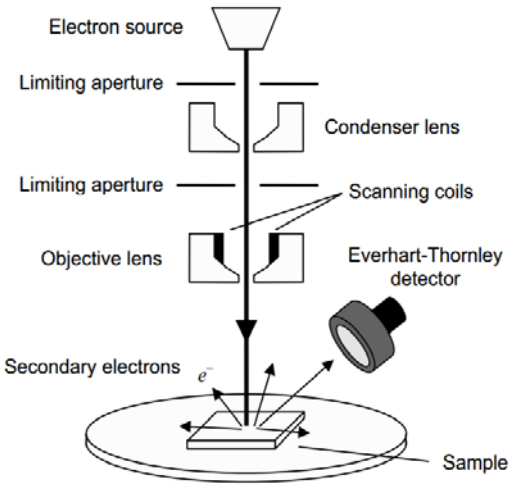

Figure 3.3: Schematic picture of a scanning electron microscopy [51]

When the primary electrons collide with the specimen's surface atoms, a number of signals such as backscattered (BSE), transmitted, auger, diffracted and secondary electrons (SE) will

be emitted. As seen from Fig. 3.4, when the primary electrons hit to the sample's surface, the energy transfers to the surface electrons. The transferred energy excites the sample's electrons and results in emission of secondary electrons. These electrons which come from atoms located in outer part of surface, have low energy approximately 5-50 eV with can be collected by a detector to create an image. The yield of secondary electrons strongly depends on the angle of incident beam with sample surface [51]. Depending on the electron microscopy and detectors, different information on composition, particle size, morphology and crystallography can be obtained.

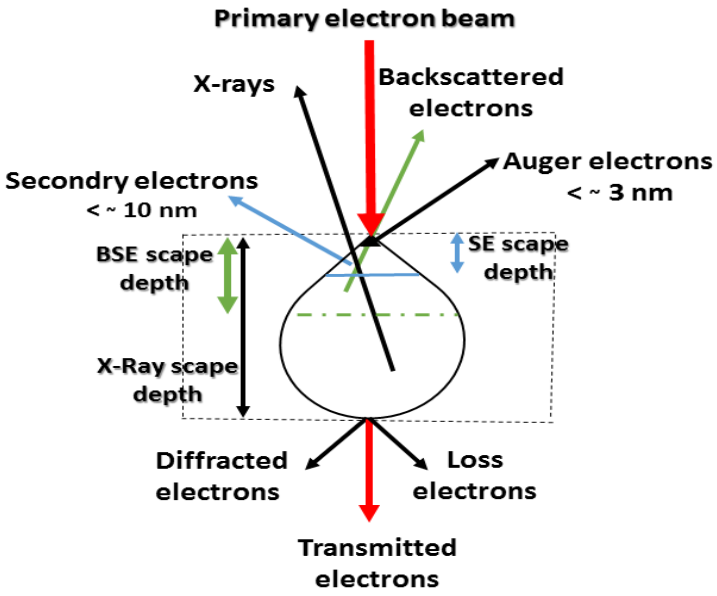

Figure 3.4: A schematic of various possible emitted signals as a result of the electron-surface interaction and approximate traveling distance for electrons [52].

In addition to SE, the high-energy backscattered electrons (BSE) which is the elastically (no loss of energy) reflected beam of the incident electrons, can be detected (see Fig. 3.5). Especially the interactions between the primary electrons and the atomic nucleus of specimen result in BSE that come from deeper distance of the surface. Therefore these electrons carry more information on the composition of the material although the resolution is not good as the secondary electrons. The backscattered electrons' yield depends on the atomic number of the constituent elements of the sample. Consequently, the image would be brighter for the element with higher atomic number.

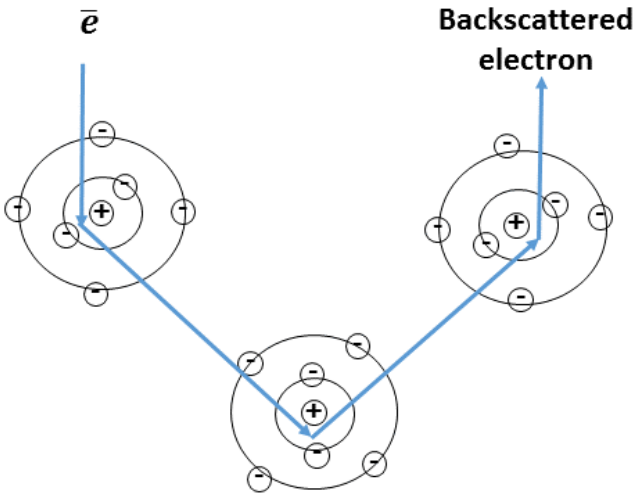

Figure 3.5: A schematic of backscattered electron

When the incident beam strike to the surface, it is possible for the inner-electron of sample to get the energy and become exited. The excited electron ejects from its shell while making a hole. This vacancy of inner shell can be filled by an electron from outer-shell with higher energy. To balance the energy difference, a characteristic X-ray would be emitted. The energy difference is unique for each transition and element. This event can occur several times for the element. Using the X-ray detector, number of emitted X-ray can be counted and used to determine the elemental composition analysis. For instance if the detector counts 60 times of characteristic Si X-ray with counting of 120 times for characteristic oxygen X-ray, it can be concluded that the surface possess oxygen as twice as Si, possibly has SiO_2 phase. This method which is widely used in the SEM instrument is called energy-dispersive X-ray analysis (EDS) [51].

3.1.3. Surface area measurement by N_2 adsorption

Catalyst surface area and its properties might be interesting parameter to determine as most of catalytic reactions occur on the surface. Thus, surface characterization of zeolite is also important to determine its porosity (i.e. the fraction of voids over total volume), surface texture, the pore sizes, the shape of pores and their pore distribution. Furthermore, zeolites' surface can be divided into internal and external areas. The latter refer to the surface area of those pores that are wider than deep, without considering the surface of the pore walls. Combining the adsorption theories with experimental data obtained with adsorption-

desorption of a probe molecule onto the material surface, quantitative and qualitative information on accessibility and availability of surface atoms can be obtained. Hence, adsorption of probe molecules, such as nitrogen, argon, or krypton, is one of the main techniques for catalysts to get information on surface properties of these porous materials [53].

The Physical and chemical reactions that occur on the surface of a material, is closely relates to the surface energy of the atoms. In order to understand why the probe molecules can easily adsorb on the material surface, it would be useful to recall energy differences between the bulk and surface atoms of a substance (see Fig. 3.6). Surface atoms of a powder material possess unsaturated bonds and they may establish new weakly bonds to their neighbors to form second particles named as aggregate or may join stronger together under mechanical force or elevated temperature named as agglomerate particles [53]. There is also a possibility for the surface particles to bond to the surrounded gas molecules to reduce their surface energy.

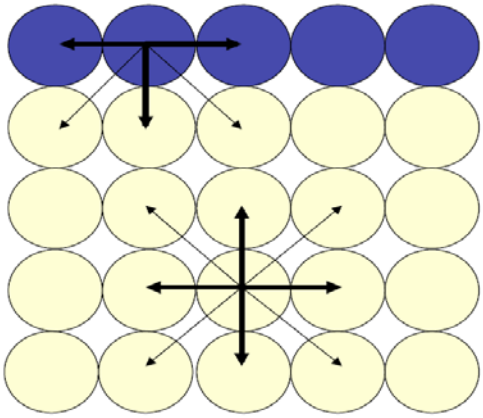

Figure 3.6: the picture shows the surface atoms in blue with unbalanced forces and the bulk atoms in pink which possess balanced forces.

During adsorption process, the catalyst surface (adsorbent) is exposed to an inert gas molecules (adsorptive) for instance N_2, in a controlled temperature and gas dosage. The gas molecules adsorb on to the surface to make monolayer/multilayer of adsorbate [53]. The physical adsorption has low adsorption heat result in no disruptive structural changes. The amount of adsorbed molecules and the relative pressure of gas phase (p/p_0) at a fix temperature can be plotted called adsorption isotherm. Different theories can be used to interpret isotherms which lead to valuable information on surface properties.

A porous material might have pores range of micro (< 2 nm), meso (2-50 nm) and macro (>50 nm) size, according to "International Union of Pure and Applied Chemistry" (IUPAC) classification. The minimum pore sizes which can be determined by sorption measurement depends on the size of adsorptive molecule, in case of nitrogen it is limited to 0.4 nm [53]. The internal surface is defined as the surface of all cracks, pores and cavities that have more depth than width, while the external surface area comprises of the areas of cracks' surface which are wider than they are deep [53]. Pore shape, adsorptive property and adsorbate-adsorbent interactions determine the pore filling mechanism.

Most of the physisorption isotherms can be categorized into six types according to IUPAC classification. As can be seen from the isotherms in Fig 3.7, the y-axis displays volume of adsorbed gas on material surface, while the x-axis reveals relative pressure of the gas (adsorptive). Isotherm of type I or Langmuir isotherm is assigned to microporous materials with rather small external surface having voids/pores in the range of micropores (<2 nm). At a very low gas pressure, the adsorbed gas only covered a small fraction of surface areas called as submonolayer as shown in Fig. 3.7. In this isotherm, the limited amount of adsorbed gas is determined by accessibility to the micropores.

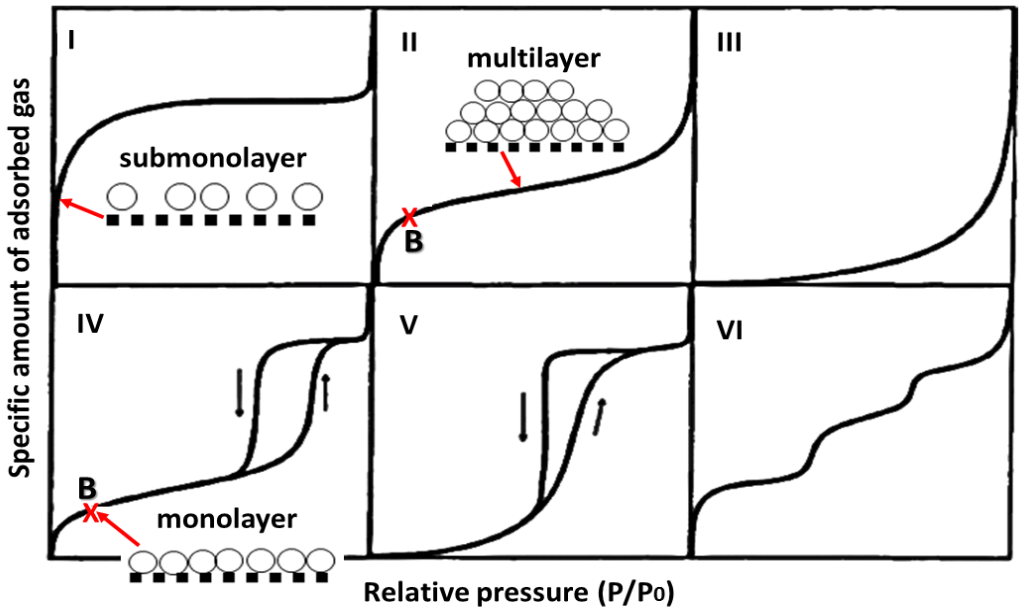

Figure 3.7: Various types of physisorption isotherms according to IUPAC classification. Most of the isotherms can be classified into these six isotherms. Reproduced from [54].

From Fig. 3.7, the monolayer coverage of adsorbate will be achieved at knee, as indicates by point B in the isotherms. From point B with increasing relative pressure of gas, the monolayer coverage will be form. Type II and IV are typical isotherms of zeolite materials.

The hysteresis effect shown as a close loop in type IV and V, might be an indication of capillary condensation in the mesopores meaning that the residual space after multilayer adsorption filled with condensate at higher equilibrium pressure of gas [53, 54].

3.1.3.1. Brunauer, Emmett and Teller (BET)

Brunauer, Emmett and Teller (BET) theory [55] consider multilayer adsorption of gas on the material surface. In this adsorption model, the surface of adsorbent divided into different parts (θ where each surface fraction covers with a number of layers of adsorbed gas molecules, as displays in Fig. 3.8. The first part with θ_0 coverage, shows zero layer of adsorbed gas, while θ_1, θ_2 and θ_3 and so on refers to one, two and three monolayer of adsorbed gas, respectively. Also, a limited number of active sites (N_0) where molecules can be adsorbed on, is considered in this theory.

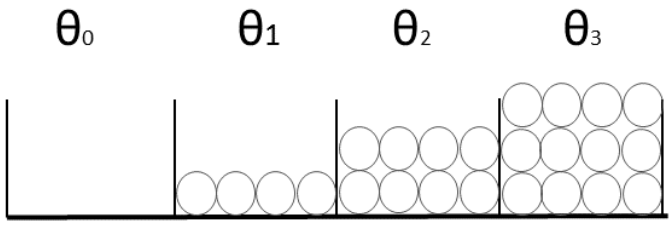

Figure 3.8: In BET method, the adsorbent surface is divided into several regions with different monolayer of adsorbate coverage seen as θ_i fractional coverage. The sum of all fractional coverage is equal to 1. Reproduced from [1].

If gas phase and adsorbent are in equilibrium with each other, the adsorption would occur via an equilibrium process meaning that the rate of adsorption and desorption is equal. Thus, the BET surface area can be determined using the isotherm data as bellow formula:

$$\frac{P}{V_a(P_0 - P)} = \frac{1}{V_0 C} + \frac{C - 1}{V_0 . C}\left(\frac{P}{P_0}\right)$$

Where: V_a is the volume of adsorbed gas on the surface at P/P_0, V_0 is defined as the volume of adsorbate in the first monolayer, P/P_0 is the relative pressure while P_0 is the condensation pressure of the gas at the temperature used and C is referred to the BET constant that depends on the shape of isotherm.

The main assumptions in BET method can be summarized as:

- Adsorbate and adsorptive are in dynamic equilibrium
- All the adsorption sites are equivalent
- There is no interaction between the adsorbed molecules/species
- The adsorption energy for the molecules from second to higher layers are equal to condensation energy
- the thickness of the multilayer has infinite value at saturation pressure ($P = P_0$)

3.1.3.2. Determination of surface area using BET theory

According to BET method, plotting the $P/ (V_a (P_0-P))$ versus relative gas pressure (P/P_0) gives a straight line with slop of $(C-1)/ (V_0. C)$ and intercept to y-axis as $1/ (V_0.C)$, shown in Fig. 3.9. When the monolayer volume of the adsorbed gas is known (V_0), the number of adsorbed gas molecules can be calculated easily using ideal gas law ($N_0^g=PV_0/ k_BT$). Taking into account the adsorptive cross-section area, in case of N_2 as 0.162 nm^2, the BET surface area can be obtained as $S_{BET} = 0.162N_0^g$. Finally, the area per gram of catalyst or specific BET surface area can be calculated by dividing BET surface area over the mass of catalyst [1].

However, the range of linearity limited to the part of isotherm with relative pressure below 0.3 [53].

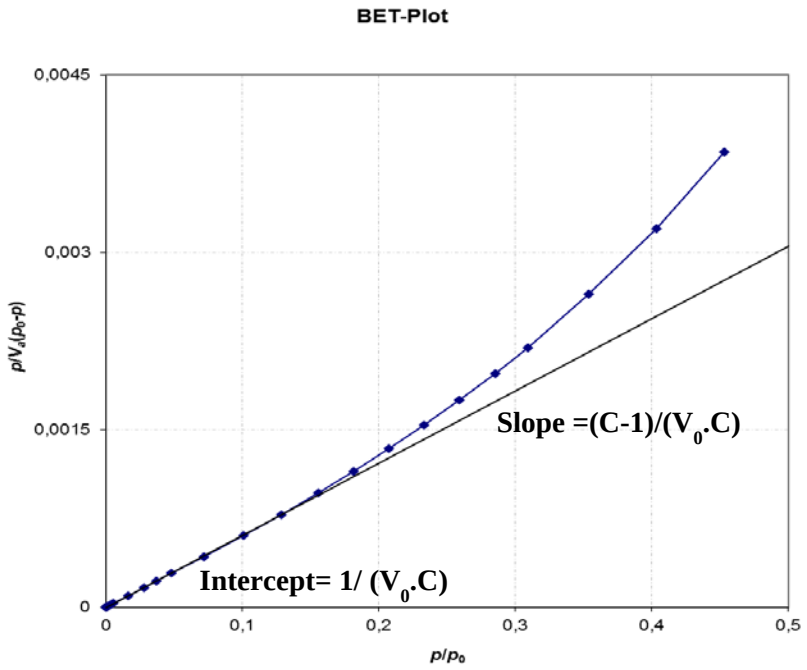

Figure 3.9: BET plot for the H-Beta sample which shows how V_0 and C can be derived from the graph. The black straight line of BET is only coinciding with the measured adsorption data points in blue at relatively low pressure of gas, below 0.3.

3.1.3.3. t-plot method and Micropore analysis

t-method was introduced by Lippens and de Boer in 1964 [56]. Simply, the statistical thickness of the adsorbed gas for a non-porous material can be calculated as:

$$t\,(P) = N_0(P)/\,(\rho \times S)$$

where: t(P) is the statistical thickness of adsorbed film on the surface, N_0 is the moles of gas adsorbed to one gram of a flat non-porous surface at pressure P, S (m^2/g) is the calculated specific surface area, and ρ (mol/m^3) is the density of the adsorbed phase.

The graph which relates the film thickness and pressure of gas (P) is known as t-curve. Now, consider another material with unknown surface geometry, but with the similar surface chemistry of the above material. t-plot of this surface can be obtained by plotting the amount of the adsorbed gas (N_{ads}) at P versus t(P). If the plot shows a straight line, then the surface can be considered as a flat non-porous surface, while any deviation from the linearity indicates the porous surface. The pressure in which the deviation occurs can be used to estimate the pore sizes , i.e. first micropores are filled at lower pressure and then meso and macropores become filled at relatively higher gas pressure [57]. As seen from Fig. 3.10, the slope of the line is considered as the external surface area, while the intercept to y-axis shows the micropores volume of the surface material. Furthermore, the micropores surface area can

be obtained by subtracting the external surface area from the total surface area (S_{BET}) as below [56]:

$$S_{micro} = S_{BET} - S_{ext}$$

Galarneau and co-workers [57] showed that this method can be used with high accuracy, if V_{micro}/V_{total} ratio is lower than 20%. Thus, in case of higher microporosity the uncertainty of using t-plot method may be raised to 40%. This huge error comes from the fact that in calculating of the adsorbed film thickness, the curvature in the micropores was ignored [57].

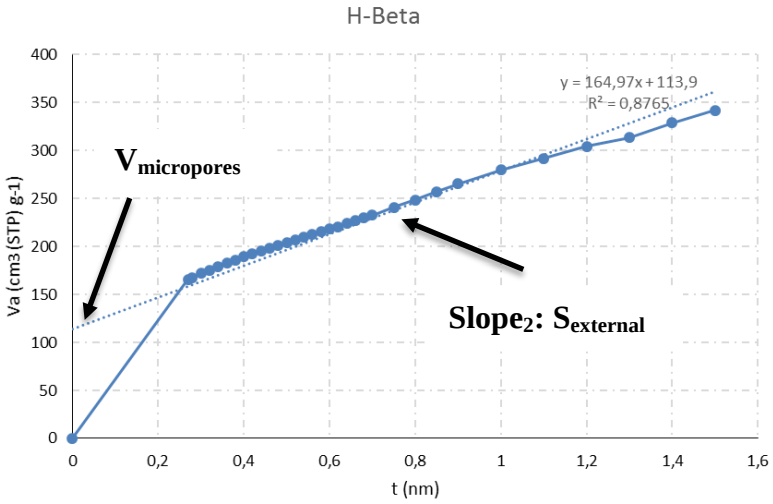

Figure 3.10: A representative t-plot graph of the fresh H-Beta sample. The external surface area can be extracted from the graph considering the slope of the line, while the intercept to the y-axis shows the micropores volume for the Beta sample.

3.1.4. Fourier Transform Infra-Red Spectroscopy (FT-IR)

FT-IR spectroscopy is the first modern method used in catalysis which use widely in catalysts characterization due to its simplicity and availability [58, 59]. This method provides valuable information on zeolite chemistry, formation of zeolite, structural vibration and surface nature in addition to identify varies adsorption and active sites of zeolites [58]. In some cases where X-ray diffraction cannot be used, FT-IR technique can give information on phase transition, composition changing of bulk material and crystallinity of the catalyst materials [60].

FT-IR is based on exiting vibrational modes of molecules via absorption of photons. Among different categories of infrared radiation, the mid-infrared region (wavenumber = 200-4000 cm^{-1}) which is capable to detect the molecular vibrations much more interested in catalysis.

Molecules possess strict vibrational and rotational levels. The vibration levels can be changed by absorption of photon with frequency (ν) in the mid-infrared region. The potential energy for small deviation from equilibrium state can be calculated resembling to the harmonic oscillator as:

$$V_r = \frac{1}{2} k \left(r - r_{eq}\right)^2$$

While V_r stands for potential energy, r is the vibrating distance of atoms, r_{eq} is equilibrium vibrating distance and k is the force constant of vibrating bond.

And the corresponding vibrational energy can be given by:

$$E_n = (n + 1/2)h\vartheta$$

$$\vartheta = \frac{1}{2\pi} \sqrt{\frac{k}{\mu}}$$

Where: E_n is the vibrational energy of nth level, n is integer, ϑ is the frequency of vibration, h stands for the Planck's constant and μ refers to the reduced mass. Thus, the vibrational frequency or wavenumber ($\tilde{\vartheta} = \frac{\vartheta}{c}$) will increase by increasing bond strength (k) or decreasing bond length [59].

The changes in vibrational frequency which originates from changing in band length can be observed by IR if dipole moment changed during vibration [59]. The intensity of IR peak is also proportional to the changes in dipole moment.

In the zeolite materials, surface OH groups might be assigned to several species such as bridged acidic OH, silanol groups on the external surface or defect sites, hydroxyl groups attached to di- or tri-valent cation, OH group attached to non-framework Al or other different sources. Using FT-IR, all types of the hydroxyl group can be characterized [58]. Permanent dipole moment of O-H group, which originates from different electronegativity of oxygen and hydrogen atom, makes it possible for direct IR study [61].

Although studying Brønsted acid sites can be performed with or without probe molecules, but for Lewis sites and extra-framework species a suitable probe molecule should be used [62]. It is better to use the reactant as the probe molecule to calculate the acidity of Brønsted or Lewis sites although in most of cases it is not applicable [58]. Choosing a proper probe molecule depends on the system in use as well as the purpose of studying. The probe molecule should

be able further to distinguish between the Brønsted/Lewis sites as well as their acid strength. The size and accessibility of the probe molecule into zeolite pores and intra-crystalline is another parameter must be considered [58]. Many different probe molecules such as ammonia, pyridine, CO_2 and CO can be used for this purpose. When a new bond forms, i.e. via hydrogen bonding of CO as a probe molecule and OH, the O-H bond becomes weaken and the band shifts to a lower wavenumber. Therefore, IR with a probe molecule allows us to calculate the relative acid strengths by monitoring these shifts of OH groups via adsorption and desorption of the probe molecule. In general, in case of stronger acid site the OH group shifts more to a lower wavenumbers [58, 59].

IR spectra in the O-H stretching region can be a good source of structural information of zeolites. The weak band at ~3740cm^{-1} is assigned to SiOH groups at the external surface. The O-H region in zeolites is typically broad which might reveal the heterogeneity of OH groups. It might be possible to split the OH region into high-frequency (HF) and low-frequency (LF) regions. The first region appears in the range of 3600-3660 cm^{-1} frequency assigned to the Si(OH)Al placed in large cages/pores of 10-ring or larger. While for the LF region (3540-3580 cm^{-1}), the band assigned to Si(OH)Al placed in smaller pores, like sodelite cages or 8-ring pores in which the hydroxyl proton can interact further with the oxygen atom in vicinity via hydrogen bonding [61].

3.1.5. Thermo gravimetric analysis (TGA)

Thermo Gravimetric Analysis **(**TGA) is one of the analytical methods to study the stability or fraction of volatile components of a material by monitoring the weight loss along a temperature range. It is also possible for some TGA apparatus to measure either temperature or heat flow differences between a specimen and one/two references to calculate the energy of adsorption/desorption of a reaction [31]. A precise microbalance, crucible which is then loaded by sample and a programmable furnace are the basic requirements of TGA apparatus.

There are two different operation modes of TGA; TPD (temperature-programmed desorption), where an inert gas is fed over the sample at increasing temperature, TPO (Temperature-programmed oxidation), where oxygen or air is fed over the catalyst. Accordingly, the weight loss of sample as a function of temperature or isothermally as a function of time in a controlled gas atmosphere can be obtained. TPO experiment may be used to elucidate the

coke content of a catalyst after testing. TPO experiment of the spent sample might be programmed such that to allow us to differentiate coke precursors into soft or hard coke depending on the temperature/atmosphere weight loss occurs [31, 63, 64].

Fig. 3.11 illustrates a representative TGA plot of a deactivated zeolite, which indicates two different weight loss stages. In the first stage, at the temperature range of 21-200 °C, a small decrease in the weight is attributed to water loss, whilst a considerable weight loss occurs in the second stage. In the second region, the trapped and coke species release from the catalyst as temperature increases to 600 °C.

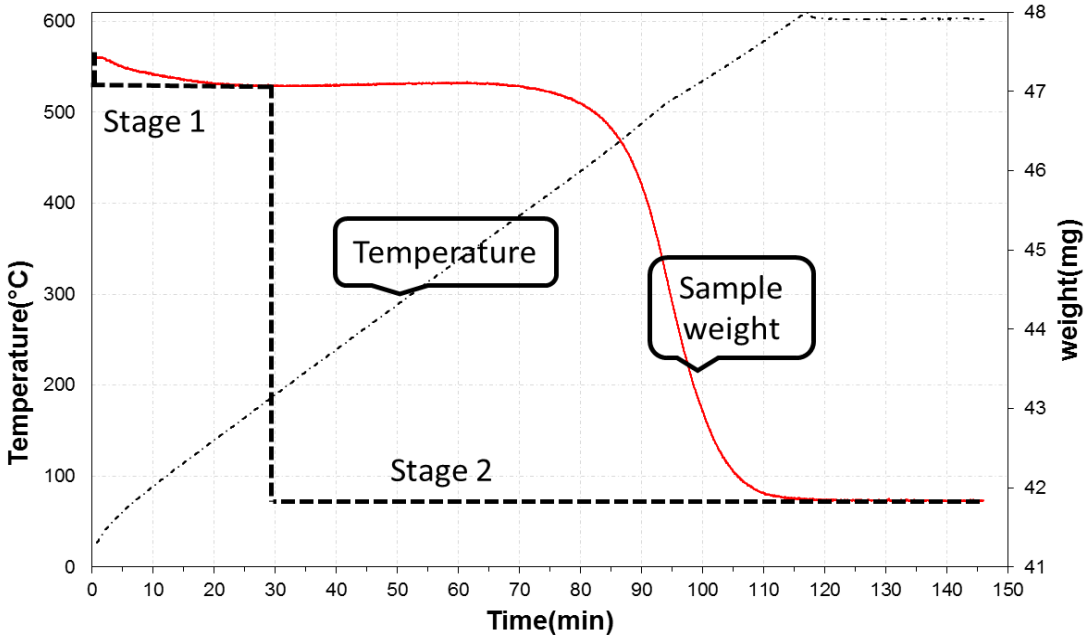

Figure 3.11: TGA plot of deactivated H-IM-5 during MTH reaction with WHSV=2 gg-1cat h-1, T = 400°C and Pp (MeOH) =13 kPa. The graph shows the weight loss as a function of time (min) and temperature (°C). The graph indicates two stages of weight loss.

3.2. Experimental

7 different zeolites as listed in Table 3.1 are covered in this study. As the protonated form of the zeolites used in catalytic testing, several calcination and ion exchange steps were employed on those samples which were not in the protonated form.

Table 3.1: List of zeolites employed in this work

Sample	Manufacture	Si/Al	Treatment
ZSM-22	Zeolyst	45	Calcination in O_2/ion exchange/calcination in muffle
ZSM-23*	Zeolyst	23	Calcination in O_2/ion exchange/calcination in muffle
Beta	SÜD CHEMIE	27	Calcination in muffle
Mordenite	VENTRON	22	Calcination in muffle
IM-5*	Homemade	15	None
ZSM-5	Süd Chemie	45	None
ITQ-13*	Homemade	50	Calcination in O_2/ion exchange/calcination in muffle

* Samples were treated and characterized by S. Kwak [46].

3.2.1. Calcination and Ion-exchange

As-synthesized samples such as ITQ-13 or ZSM-22 were calcined in the tubular furnace under a flow of pure oxygen at 550 °C for 9 h to remove the structural directing agent used in synthesizing process. The furnace was programmed to increase the temperature from 25 °C to 550 °C within 2 h under a flow of Nitrogen/Oxygen (70:30) and then 2 h with (50:50) N_2/O_2 mixture flow. The temperature was kept constant at 550 °C, while the flow was changed to (30:70) N_2/O_2. Afterwards, sample was kept at 550 °C for 9 h in a pure flow of oxygen. The calcined sample was ion exchanged 3×2 h with 1M NH_4NO_3 at 70 °C water bath. Final step to remove ammonia from ion-exchanged sample was performed at 550 °C for 5 h under static air in muffle furnace.

A milder calcination process with static air was performed on the ammonia form of Beta zeolite.

3.2.2. Characterisation methods

In order to characterize the samples, X-Ray Diffraction (XRD), infrared spectroscopy (FT-IR), N_2 adsorption measurement and Scanning Electron Microscopy (SEM) were performed due to the availability and popularity. The characterization was conducted on the protonated form of the zeolites.

3.2.2.1. Powder X-ray Diffraction (XRD)

X-ray diffraction measurements were carried out using Bruker D8 Advance diffractometer with Bragg-Brentano geometry and Germanium (111) Johansson monochromator. Cu $K_{\alpha 1}$ radiation with wavelength of λ= 1.5406 Å was used. The powdered samples were packed in the deep cavity-type sample holder as shown in Fig. 3.12, gently pressed to get a flat and smooth surface. The diffractograms were collected at 0.05° intervals (Δ) and between 2-60° (2θ) using a count time of 2 minutes.

Figure 3.12: Sample holder used in powder XRD characterisation. The powder sample is placed in the center of cavity type sample holder while making the flat and smooth surface by gently pressing the powder.

3.2.2.2. Scanning Electron Microscope (SEM)

Scanning electron microscopy (SEM) was carried out by Hitachi SU8230 instrument while data were analysed with QUANTAX software. The instrument was equipped with both secondary and backscattered electron detectors in addition to the detector for elemental analysis of energy-dispersive X-ray spectroscopy. A small amount of powder sample was placed on the carbon tape on the circular sample holder. The working distance of about 4 mm and acceleration voltage of 3-10 kV with vacuum condition was used to take the micrographs.

Energy-dispersive X-ray spectroscopy (EDS) was used to determine the chemical composition of the selected part of each sample. At least two different parts of the sample were chosen to obtain the Si/Al ratio.

3.2.2.3. Surface area measurement by N_2 adsorption (fresh catalysts)

Surface area measurements were performed in BELSORP-mini II apparatus by adsorption of nitrogen at its boiling point (77 K). For both fresh and deactivated catalyst, approximately 50 mg of powder sample was weighted carefully. In case of the fresh sample, it was outgassed at 80 °C for 1 h followed by 4 h at 300 °C under vacuum prior to sorption measurement.

3.2.2.4. Surface area measurement by N_2 adsorption (spent catalysts)

All the spent catalysts, deactivated catalysts after the MTH reaction, were removed out of the reactor and kept for coke analysis. The surface area was obtained by nitrogen adsorption onto their surfaces. The sorption measurement was done for all seven zeolite samples: ZSM-22, ZSM-23, Mordenite, ITQ-13, IM-5, Beta and ZSM-5. As MTH reaction was performed with three different space velocities for each zeolite topology, in total 21 sorption measurements were carried out with the same apparatus as mentioned above.

It is worth to note that a milder pre-treatment condition was performed during the outgassing process in case of the spent catalysts. The sample was heated up to 80 °C for 1 h followed by 3 h at 200 °C in order to outgas the sample and make it ready for nitrogen sorption measurement.

3.2.2.5. Fourier Transform Infra-Red Spectroscopy (FT-IR)

FT-IR spectroscopy measurements using CO as a probe molecule were performed by FT-IR Bruker vertex 80 instrument and spectra were collected with MCT (Mercury Cadmium Telluride) detector and KBr Beam Splitter. Samples were prepared by pressing the powder into a thin wafer while a gold envelop was used to hold the thin wafers in the transmission quartz cell with KBr window. Prior to adsorption of CO, all the samples were treated under vacuum for 1 h at 120 °C, 1 h at 300 °C and finally 1 h at 450 °C to release water and other hydrocarbons from the catalyst pores. Then, the cell and sample were cooled down to 77 K using liquid nitrogen to be ready for CO adsorption. The temperature was kept at 77 K during the adsorption/ desorption process of CO on the sample. While the highest coverage of CO reached, the spectra continuously were collected during the desorption process of CO. By

opening and closing the line valve in a short interval, CO would be desorbed from the zeolite during the equilibrium process.

3.2.2.6. Thermo gravimetric analysis (TGA)

Temperature-programmed oxidation (TPO) of the spent catalyst was carried out on a Rheometric Scientific SAT 1500 instrument. When the MTH reaction finished, the reactor was disconnected and quenched normally in air to room temperature and spent catalyst was removed and kept for characterisation measurements. As the amount of each catalyst was only ~50 mg, and ~30 mg was needed for TPO analysis, it was necessary to perform N_2 adsorption measurements before they were subjected to TPO analysis. N_2 adsorption measurements were carried out with mild pretreatment conditions (see Section 3.2.2.4) to ensure not to lose any retained compounds.

As the main aim of the TGA analysis in this work is to obtain the total amount of coke, a simple method of using a flow of pure oxygen (20 ml/min) in a temperature range of 21-600 °C with a heating rate of 5 °C/min and a holding time of at least 2 hours at 600 °C, was used to ensure all coke formed during MTH reaction were burnt off. After the experiment was done, the colour of the tested sample became totally white, indication of no coke remained in the zeolite.

First, the microbalance was calibrated with the empty platinum crucible and then approximately 30 mg of the grinded sample was filled into the crucible and pressed gently. As the cylindrical oven elevated, the crucible was surrounded by the oven.

3.3. Results and discussion

Part of the results obtained from the characterization instruments are presented in this section. The TGA and surface area data for the spent catalysts were shown in the result and discussion part (chapter 5). While the results of all samples are present in this part, the relevant graphs of those samples which characterized by S. Kwak [46] can be found in Appendix 1.

3.3.1. Powder X-ray Diffraction (XRD)

In this study, X-ray diffraction (XRD) was used to confirm the crystalline structure and phase purity of all the zeolite catalyst. Fig. 3.13 shows the collected XRD pattern of H-Beta in pink. For comparison, the reference XRD pattern from "The International Zeolite Association (IZA)" [50] (in black) is also included. All the main peaks of *BEA material are presented in H-Beta XRD pattern, although most of the peaks in H-Beta sample became broaden.

In general, peak broadening might be an indication of poor crystallinity [47]. However, it is also possible to have peak broadening due to incomplete destructive interference of beams for crystal size below 100 nm or when the internal strain presence within the crystal [65]. The broad peak at $2\theta = 7.6°$ and a narrow peak at about $2\theta = 22.5°$ were reported before by Yu et al. [66] while studying H-Beta sample with SiO_2/Al_2O_3=25. They related these peaks to the well-ordered structure of Beta sample. Shangjiao and co-workers [67] have previously reported that the intensity of XRD peaks decreased by decreasing the Al contents of Beta sample. They compared three samples of Beta structure with different SiO_2/Al_2O_3 ratio of 5, 10 and 25. The decreasing peak intensity is due to presence of more defects and poor crystallinity of Beta structure with higher Al content. The similar conclusion previously reported by other researchers as well [68, 69].

The presence of background in diffractogram might suggest a mixture of amorphous and crystalline phases which is an indication of phase impurity [48, 70]. Beta structure is known as a structure with intergrowth of planes. These planes have the similar reflection angle and may cause peak broadening or presence of background in the Beta diffractogram [71], as seen from its diffractogram.

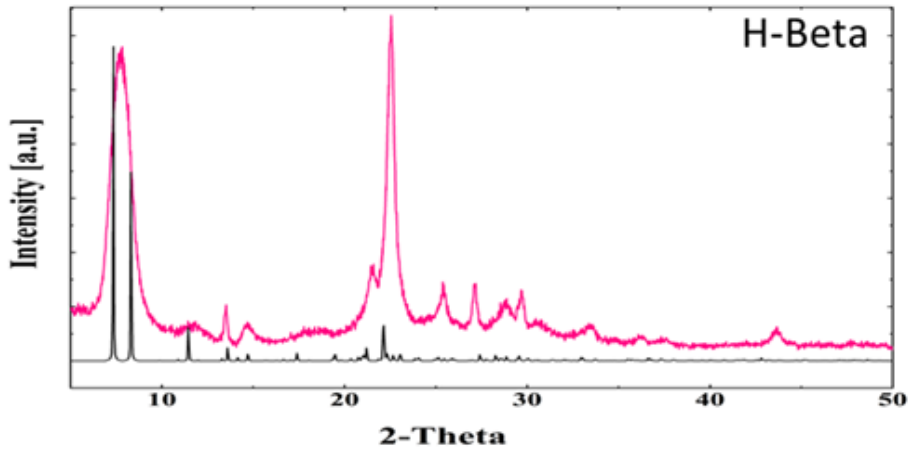

Figure 3.13: The collected (in pink) and reference from IZA [45] (in black) XRD pattern of H-Beta over a range of 2θ between 5 to 50 °.

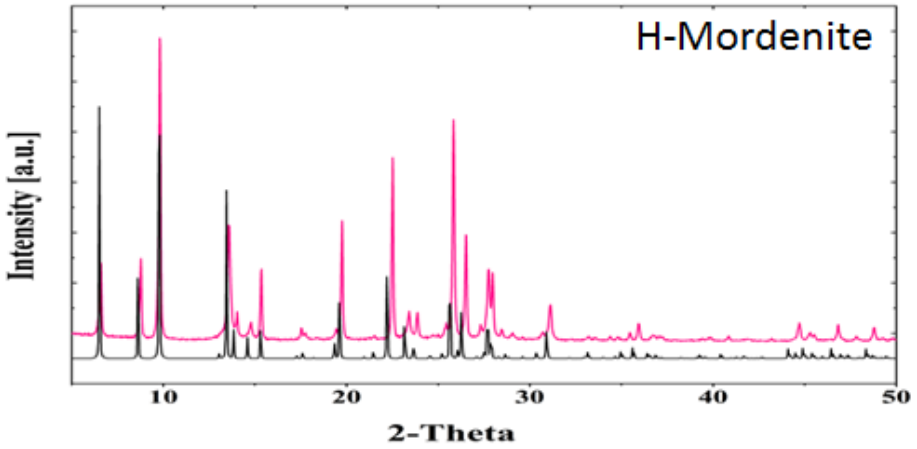

Figure 3.14: The collected (in pink) and reference from IZA [45] (in black) XRD pattern of H-Mordenite over a range of 2θ between 5 to 50 °.

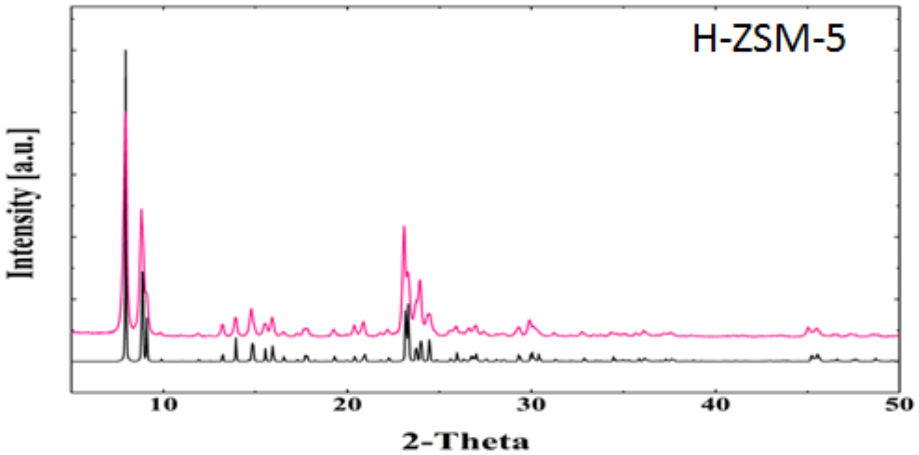

Figure 3.15: The collected (in pink) and reference from IZA [45] (in black) XRD pattern of H-ZSM-5 over a range of 2θ between 5 to 50 °.

The XRD diffractogram and reference pattern of H-Mordenite are shown in Fig. 3.14. All the characteristic peaks in the reference pattern were present in diffraction pattern which confirmed that the desired pure Mordenite structure was present. Also the sharp peaks of the collected pattern revealed high crystallinity of Mordenite. The peaks positions were shifted slightly to the right in x-axis (2θ angel) especially at higher angles. The reference XRD pattern belongs to Mordenite structure with idealized chemical composition of $Na_8(H_2O)_{24}|\,[Si_{40}Al_8O_{96}]$ and Si/Al ratio of 5 while in Mordenite used in this study, the Si/Al ratio was 22. The bond length of Al-O (1.74 Å) is larger than in Si-O (1.61 Å). Therefor the unit cells with Al-O connections would be larger compared to units with only Si-O connections. This difference in unit size reflects in XRD pattern especially at high reflection angles [47]. With higher Al contents peaks are more shifted to the left in x-axis in line with the observation here while comparing two XRD patterns with Si/Al = 5 of the reference and Mordenite studied with Si/Al = 22.

The collected XRD pattern together with the standard diffractogram of H-ZSM-5 sample is depicted in Fig. 3.15. Comparing the position and intensity of peaks confirmed that the ZSM-5 sample had the desired crystallinity. Al-Dughaither et al. [70] claim that two XRD peaks with highest intensities at 7.94° and 8.9° are characteristic peaks which confirm the MFI structure, as seen also here.

Experimental XRD patterns of four zeolites used in this study, H-ITQ-13, H-IM-5, H-ZSM-22 and H-ZSM-23 were not measured in this study, but was reported in a parallel study by S. Kwak [46] and presented in Appendix 1. Since those samples were subjected to catalytic testing in this study, the diffractograms are included here for comparison. The patterns indicated the desired structure in each case. In case of H-ZSM-22, the differences between the collected diffractogram and the reference were attributed to the difference in sample preparation. It was noted by Kwak [46], in contrast to other sample preparation with the powder itself, in case of H-ZSM-22 a small portion of sample powder was mixed with distilled water and used to collect the diffractogram. The sharp peaks proved that the crystalline phase presence in zeolite samples.

In conclusion, XRD experiments for all 7 zeolites in this work revealed that the desired phase were present in each zeolite with a well-crystalline structure and no evidence of amorphous phase. The particle size might be obtained from chromatograms considering the width of peaks according to Scherrer equation and is presented in section 3.4 to compare with the

values obtained by other methods. As the crystallites getting smaller, the peaks become wider. The comparison of the peak width showed that H-Beta sample had the smallest particles followed by H-ZSM-5 and H-ZSM-23. H-ZSM-23 had smaller particles than H-ZSM-22 sample which might be effect on catalytic properties of these similar 1D 10-ring channels as will be referred further. H-Mordenite, H-IM-5, H-ITQ-13 and H-ZSM-22 had a similar particles size.

3.3.2. Scanning electron microscopy (SEM)

The SEM micrographs of H-Beta, H-Mordenite and H-ZSM-5 samples are shown in Figs. 3.16-18, respectively. Fig. 3.16 shows two micrographs of H-Beta with different magnifications, the left panel with lower magnification of (×25000) and the right panel with higher magnification (×45000). It can say the shape of Beta crystals were nearly rounded balls in line with previous studies [72-74]. The average crystal size might be considered less than 0.1 μm. Turning to the H-Mordenite in Fig. 3.17, a bigger crystallite size between 0.2-1 μm was found. Plate-shaped crystals for H-Mordenite were detected from the micrographs. Previously, lamellar or plated morphology was reported for H-Mordenite with SiO_2/Al_2O_3=200 by Martucci et al. [75] in agreement with our observation here.

The micrograph of H-ZSM-5 in Fig. 3.18, displayed an agglomerate crystals with an average size between 0.05-0.1μm in good agreement with the reported values by Bleken et al. [76]. From the picture, the exact size and shape of crystal could not be determined.

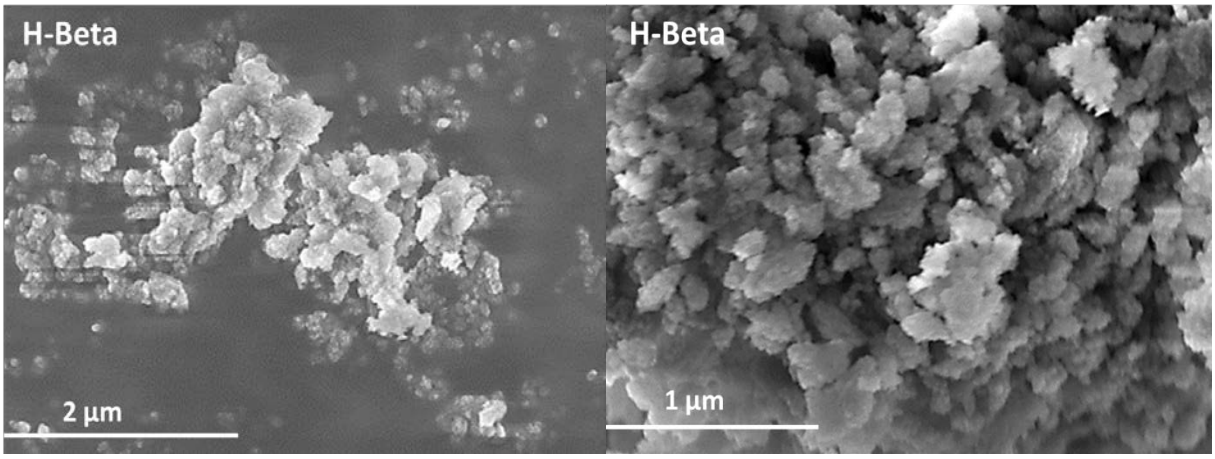

Figure 3.16: SEM micrographs of H-Beta sample taken with: (left panel) low magnification (×25000) and (right panel) with higher magnification (×45000). The images were taken in low voltage, 3keV, and 4.1 mm working distance.

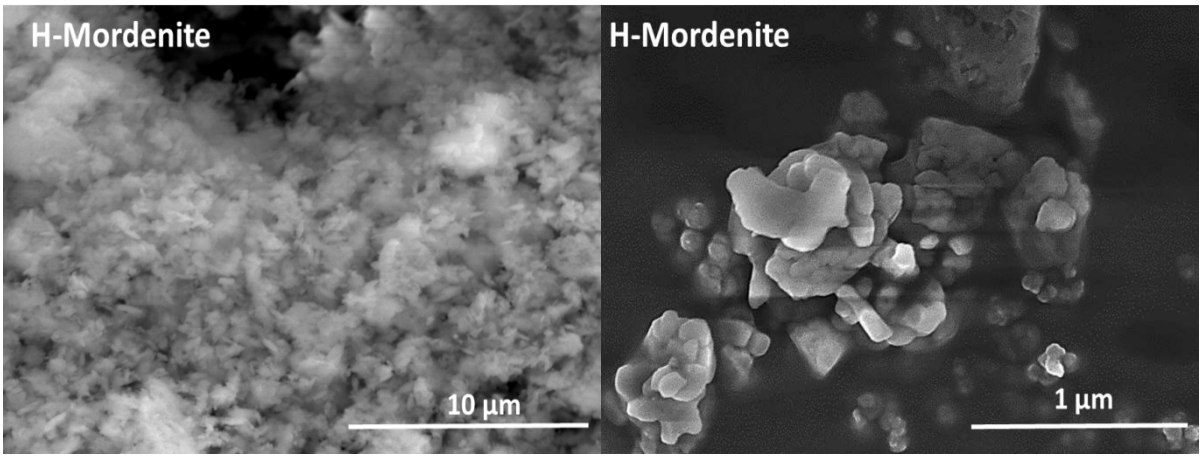

Figure 3.17: SEM micrographs of H-Mordenite sample taken with: (left panel) low magnification (×5000), 10.7 mm working distance, and HV of 20kV, (right panel) higher magnification (×45000), 4.2 mm working distance, and LV of 3kV.

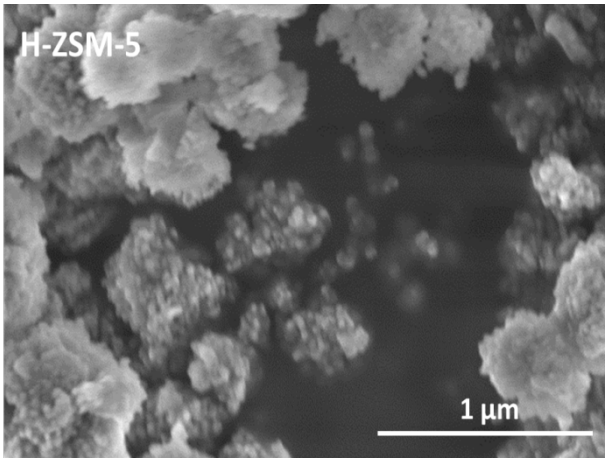

Figure 3.18: SEM micrograph of H-ZSM-5 sample taken with magnification of (×45000), 4.2 mm working distance, and LV of 3kV.

The micrographs of H-ZSM-22, H-ZSM-23, H-ITQ-13 and H-IM-5 which were captured by S. Kwak [46] are presented in Fig. 3.19 as marked with a, b, c, and d, respectively. Fig. 3.19.a shows the rod-shaped crystals of H-ZSM-22 with an average size of 2 µm in length. The same shape for H-ZSM-22 crystals have been reported by S. Teketel [77]. In Fig. 3.19.b, much smaller crystals between 0.1-0.2 µm in average with rod-like shape can be found for H-ZSM-23. Micrograph of H-ITQ-13 in Fig. 3.19.c, revealed an agglomerate needle-shaped particles with approximately 0.1-0.2 µm in length. The needle-shaped crystals of H-ITQ-13 was previously reported by Skistad et al. [78] in line with the observation here. The micrographs of H-IM-5 in Fig 3.19.d, were not good enough to recognize the exact shape of crystal but it might be noted that the particle were in the range of 0.1-0.2 µm.

In conclusion, micrographs revealed relatively large rice-like particles with approximately 2 μm in length for H-ZSM-22, while the needle shaped particle less than 0.1-0.2 μm were found for H-ZSM-23 and H-ITQ-13. Plate-shaped particles with 0.2-1 μm in length and rounded particles of 0.1 μm can be found for H-Mordenite and H-Beta crystals, respectively. The particles within the range of 0.05-0.1 μm were observed in H-ZSM-5. The crystals of H-IM-5 with average length of 0.1-0.2 μm were seen, while the shape of particles was not recognizable.

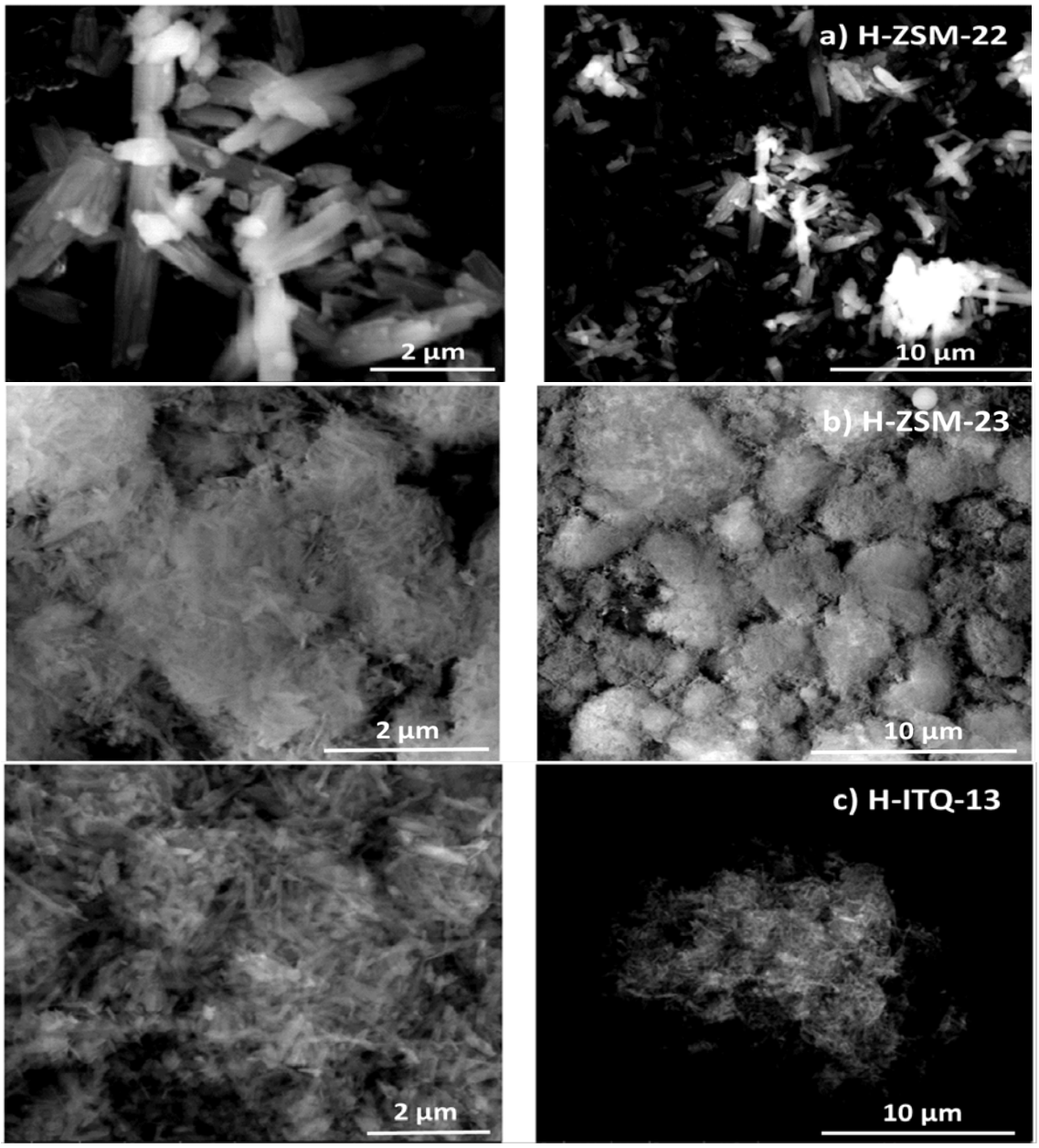

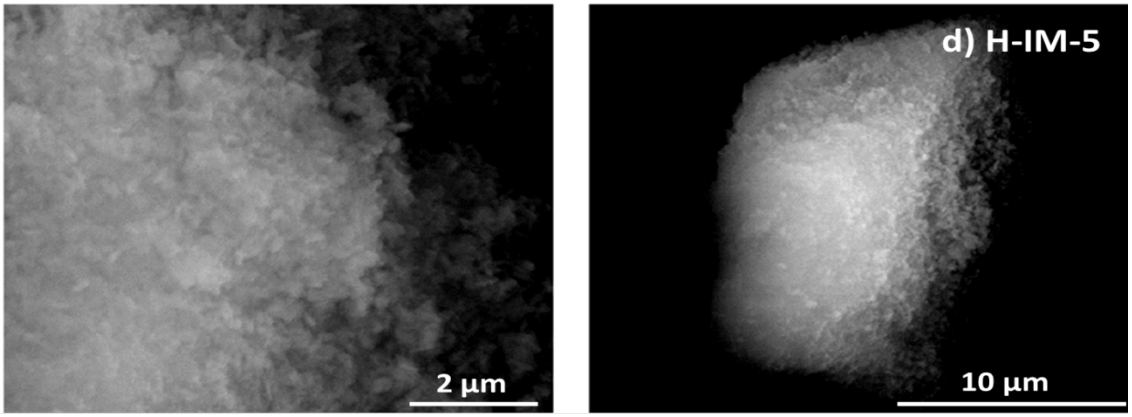

Figure 3.19: SEM images of a) H-ZSM-22 b) H-ZSM-23 c) H-ITQ-13 d) H-IM-5 were captured with high voltage of 30 kV, and working distance of 10 mm: (right panels) at low magnification x5000 and (left panels) at higher magnification of x15000/x20000. Micrographs were taken by S. Kwak [46].

In addition to the micrographs, Si/Al ratios of zeolites were determined using Energy-dispersive X-ray spectroscopy (EDS) analysis.

The typical EDS graph for H-ZSM-5 sample is shown in Fig. 3.20. The Y-axis counts the number of x-rays which received to the detector while X-axis shows the energy level of those x-rays. The Al, Si and O peaks were detectible in the graph. At left-most side of graph, a small detected Carbon peak came from the background; a carbon tape used as a support for powder sample. Thus, the relative proportion of elements can be calculated by EDS analysis as shown in Table 3.2. In each case, at least two different areas were selected and an average value was reported.

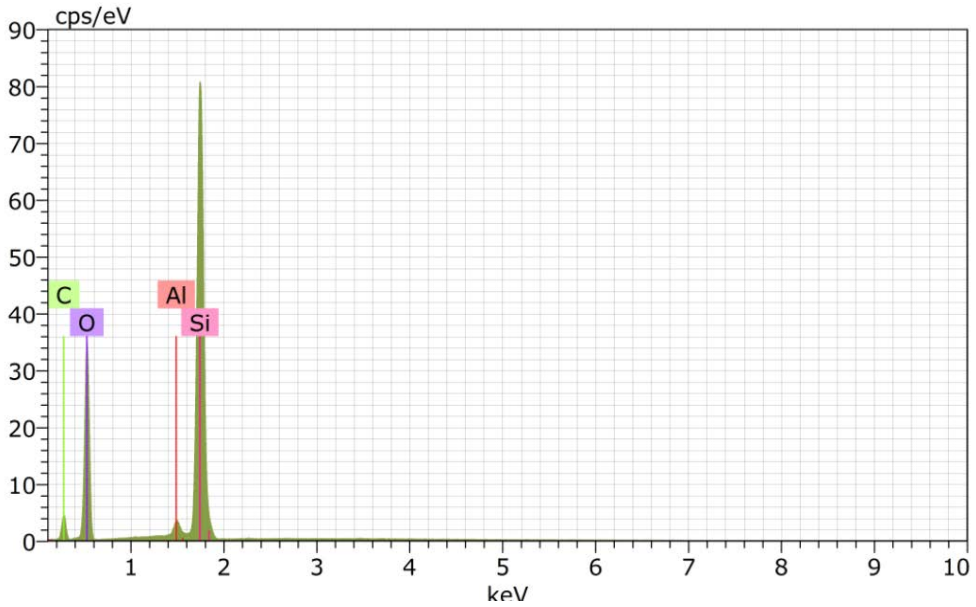

Figure 3.20: EDS analysis of H-ZSM-5 zeolite. The Y-axis shows the number of detected x-rays by detector, while X-axis indicates the energy for those counts.

Table 3.2: Si/Al ratios of studied zeolites obtained from producer and EDS analysis.

sample	Si/Al (given by producer)	Si/Al (EDS)
ZSM-22	45	33
ZSM-23	23	22
Mordenite	22	15
IM-5	15	15
ITQ-13	50	30
Beta	13.5	15
ZSM-5	45	32

In general, the Si/Al ratios determined by EDS were similar to those obtained by supplier, see Table 3.2. Only in the case of the homemade ITQ-13, the difference between the synthesis Si/Al ratio (left column) value and measured with EDS was quite high, suggesting that the desired Si/Al ratio was not achieved when synthesized the ITQ-13 zeolite or the reported value might corresponds to gel rather than the final synthesized ITQ-13 structure [46].

3.3.3. Surface area measurement by N_2 adsorption

N_2 adsorption-desorption isotherms of 7 zeolites are shown in Fig. 3.21 to Fig. 3.27. Furthermore, a summary of all textural properties (surface area and pore volume) is listed in Table 3.3.

The shape of the isotherms are the combinations of type II and IV according to IUPAC classification [54]. As mentioned, isotherm type II is attributed to a solid material having only micropores, while in type IV both micro and meso pores are present in the material [54]. In all isotherms of Figs. 3.21-27, the volume of adsorbed gas increased up to the limited value (point B in the graphs) at very low relative pressure of nitrogen gas (P/P_0) to fill all micropores and make mono-layer coverage of the adsorbed gas as indicates in the graphs by point B. The limited uptake of gas in high pressure range can be found from the isotherms as well.

N_2 adsorption-desorption isotherm of H-ZSM-22 is shown in Fig. 3.21. The calculated specific surface area, according to BET method was 217 m^2/g. From Table 3.3, less than 9% of the total surface was the external surface while above 90% of the surface was assigned to the internal surface. Previously, for different synthesized batches of H-ZSM-22, BET surface area (S_{BET}) between 153 to 241 m^2/g was reported by S. Teketel [77].

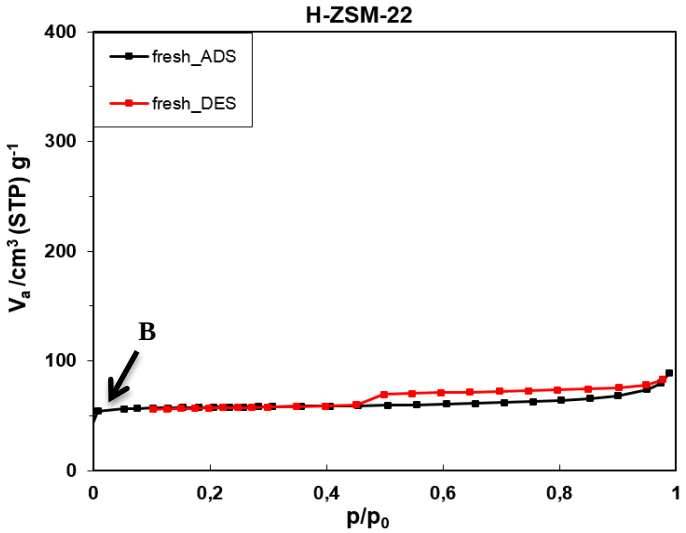

Figure 3.21: N_2 adsorption-desorption isotherm at 77K for H-ZSM-22. Black curve displays adsorption of N_2 gas, while the red curve is related to desorption process of the zeolite material.

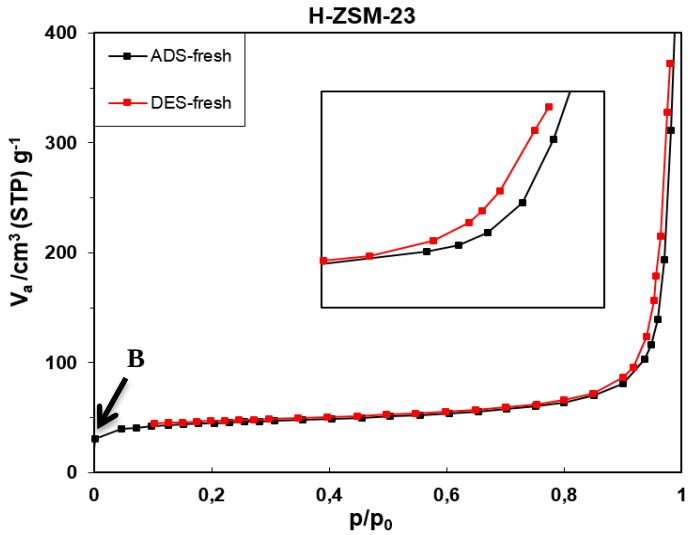

Figure 3.22: N_2 adsorption-desorption isotherm at 77K for H-ZSM-23. Black curve displays adsorption of N_2 gas, while the red curve is related to desorption process of the zeolite material.

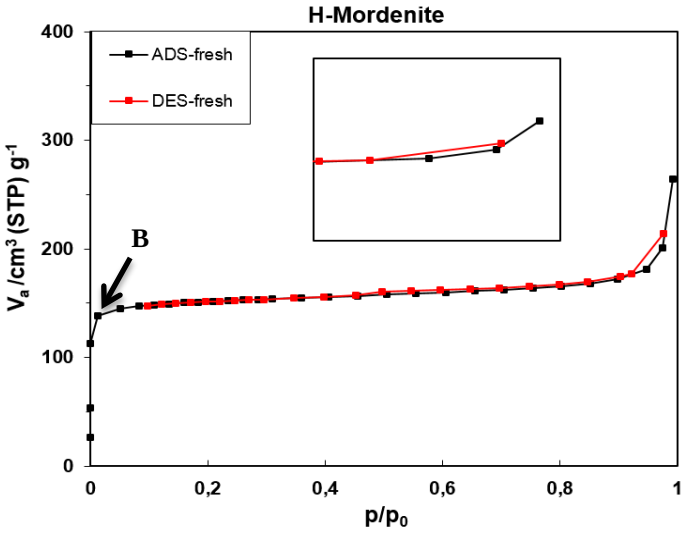

Figure 3.23: N_2 adsorption-desorption isotherm at 77K for H-Mordenite. Black curve displays adsorption of N_2 gas, while the red curve is related to desorption process of the zeolite material.

He also calculated the theoretical BET surface area of ZSM-22 using Material Studio 4.2 software which was 230 m^2/g. In another work, a specific surface area of 196 m^2/g was reported for commercial H-ZSM-22 by W. Skistad [79]. Therefore, the obtained BET surface area of H-ZSM-22 in this work as 217 m^2/g is comparable with those reported values [77].

Table 3.3: Textural properties of samples studied in this work.

Samples	Surface area (m^2/g)			Pore volume (cm^3/g)			V_{micro} / V_{total} (%)
	S_{BET} [a]	S_{micro}	$S_{external}$ [b]	V_{total}	V_{micro} [b]	V_{meso}	
H-ZSM-22	217	197	20	0.137	0.08	0.06	58
H-ZSM-23	159	103	56	0.66	0.05	0.61	7.5
H-Mordenite	576	532	44	0.40	0.22	0.18	55
H-IM-5	482	364	118	0.81	0.15	0.66	18
H-ITQ-13	461	421	40	0.39	0.17	0.21	43
H-Beta	713	495	218	1.12	0.20	0.92	18
H-ZSM-5	422	309	113	0.61	0.14	0.47	23

Surface area determined by a) BET method, b) t-plot method.

The isotherm of H-ZSM-22 further showed a hysteresis effect at relatively low pressure of the gas around P/P_0 = 0.4. The hysteresis in H-ZSM-22 isotherm at low pressure was rather attributed to the property of adsorptive which caused by changes in gas volume at the boiling point of N_2 (P/P_0 = 0.42) than the nature of adsorbent surface [54]. From Table 3.3, while the t-plot method employed for H-ZSM-22, the micropore and total pore volume obtained as 0.08 and 0.137 cm^3/g, respectively. As noted before, for $(V_{micro}/V_{total})\times100 > 20\%$, the combined error with t-plot method is increased even to 40%, [57]. Thus, for this sample with 58% contribution of the micropores in the total pore, t-plot gave rise to a huge error. Thus, the value should be considered with care.

Fig. 3.22 indicates the N_2 adsorption-desorption isotherm of H-ZSM-23. The measured specific surface area for this sample was 159 m^2/g. The BET surface areas of 115 m^2/g for the commercial H-ZSM-23 was previously reported by W. Skistad [79] in line with the obtained value here, indication of a well-open zeolite structure. The isotherm also displays a hysteresis loop at high pressure (> 0.8) which might be related to capillary condensation in the mesopores. The calculated (V_{micro}/V_{total}) as 7.5% gave the ratio of internal/external surface area with high accuracy using the t-plot method [57]. Thus, for the H-ZSM-23 zeolite almost 65% of the surface area was dedicated to internal surface and the rest (35%) was the external surfaces.

The adsorption-desorption isotherm of H-Mordenite is shown in Fig. 3.23 and the specific surface area as 576 m^2/g was calculated. In the research done by Aguado and co-workers [80], the total surface area for the synthesized Mordenite were in a range of 385-485 which is not far from the obtained value here. However, the shape of the Mordenite isotherm is typical for micro/meso porous and a high value for (V_{micro}/V_{total}) as 55% resulted in a big error while calculating internal/external surface area using t-plot method, see Table 3.3 [57].

Fig. 3.24 presents the sorption isotherm of H-IM-5. From Table 3.3, the calculated specific surface area for IM-5 was 482 m^2/g. The isotherm and the values of surface area obtained is in good agreement with those reported for H-IM-5 having Si/Al= 15 (425 m^2/g) by W. Skistad [79], which approved the open and accessible pore structure in H-IM-5 sample. The hysteresis effect detected at higher equilibrium pressure of gas might be an indication of mesoporosity [54]. Also with a high accuracy the internal and external surface areas can be determined as 364 and 118 m^2/g, respectively.

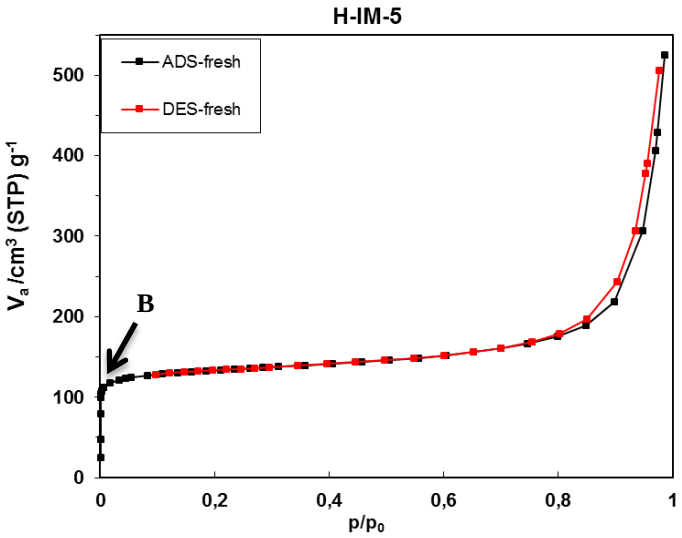

Figure 3.24:N2 adsorption-desorption isotherm at 77K for H-IM-5. Black curve displays adsorption of N_2 gas, while the red curve is related to desorption process of the zeolite material.

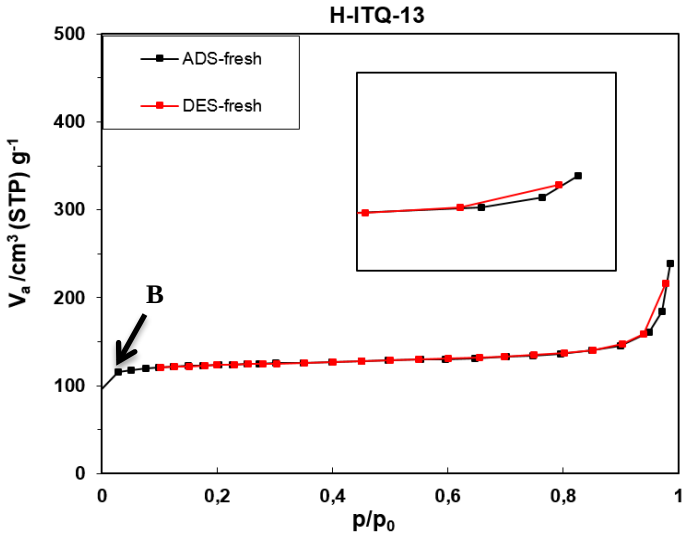

Figure 3.25: N2 adsorption-desorption isotherm at 77K for H-ITQ-13. Black curve displays adsorption of N_2 gas, while the red curve is related to desorption process of the zeolite material.

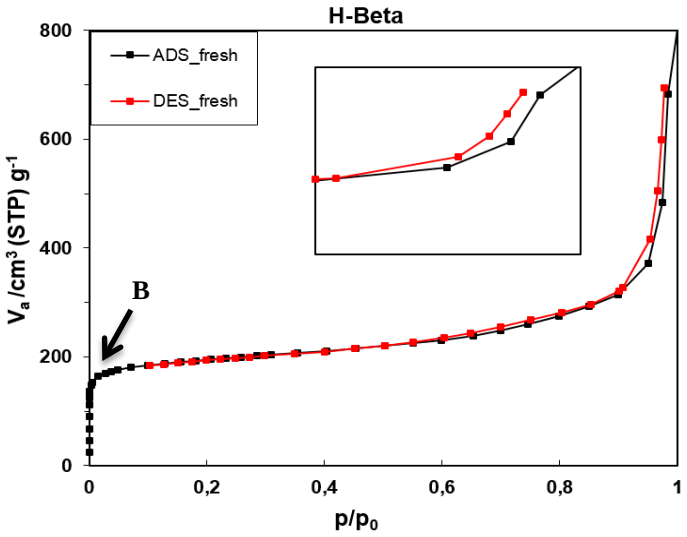

Figure 3.26: N2 adsorption-desorption isotherm at 77K for H-Beta. Black curve displays adsorption of N_2 gas, while the red curve is related to desorption process of the zeolite material.

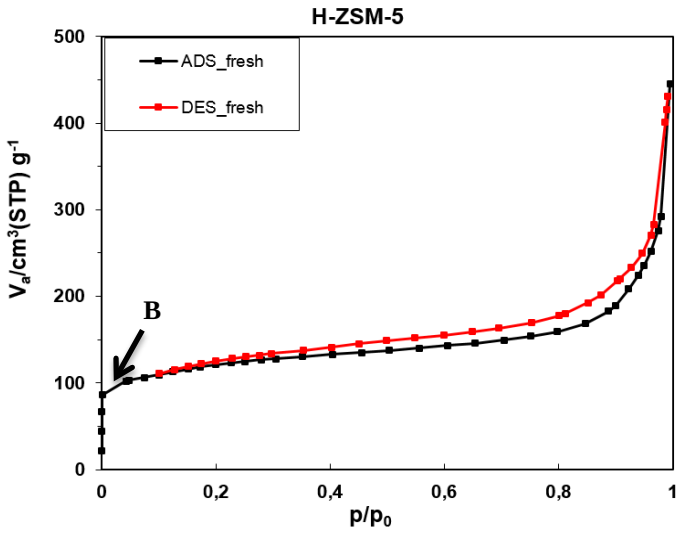

Figure 3.27: N2 adsorption-desorption isotherm at 77K for H-ZSM-5. Black curve displays adsorption of N_2 gas, while the red curve is related to desorption process of the zeolite material.

Fig 3.25 presents the N_2 isotherm of H-ITQ-13 and corresponding value of the specific surface area was 461 m^2/g. Skistad [79] synthesized two batches of ITQ-13 having $(Si+Ge)/Al_{EDS}=42$ with needle-like particles and plate-like crystals containing $(Si+Ge)/Al_{EDS}>100$. The N_2 sorption showed a value of S_{BET} = 413 m^2/g for the needle shaped crystals and S_{BET} = 455 m^2/g for the plate-like particles. Hence, the surface area of the homemade ITQ-13 zeolite in this work is in line with those reported data and showed an open and accessible structure [79]. However, the high ratio as 43% for the V_{micro}/V_{total} revealed high uncertainty while calculating the internal/external surface area [57].

From Fig. 3.26 and Table 3.3, the total surface area, micro and mesopores areas of H-Beta were as follows; S_{BET} =713, S_{micro}=495 and S_{meso}=218 m^2/g. Bjørgen and Kolboe [81] previously reported S_{BET} = 608 m^2/g for this zeolite topology having Si/Al=12. Thus, an open and accessible structure of Beta sample was present.

The adsorbed volume of gas as a function of relative pressure for H-ZSM-5 sample is shown in Fig. 3.27. The specific surface area for this sample was 422 m^2/g (see Table 3.3). Sang and co-workers [82] synthesized various ZSM-5 zeolites using different templates which were characterized by routine characterization techniques such as nitrogen adsorption measurement. They noted a range of BET surface areas of 264-312 m^2/g for those ZSM-5 samples comparable with the obtained value here.

In summary, the N_2 adsorption-desorption isotherms of the samples studied were a combination of type II and type IV in IUPAC classification; therefore zeolites are micro/meso materials. The relatively big hysteresis loop at low pressure in H-ZSM-22 was attributed to the properties of adsorptive gas than the adsorbent nature. The capillary condensation in mesopores which might be seen by a hysteresis loop must be occur at relative high relative pressure of gas (> 0.8) while having adsorbed gas multilayers. The hysteresis region in H-ZSM-23 and H-IM-5 samples was probably originated from the aggregated plate-like particles (see also SEM micrographs in part 3.3.2). The textural properties of the zeolites can be extracted from N_2 isotherms listed in Table 3.3. The specific surface area of a material depends on whether or not the structure is open, i.e. whether all atoms, or only a small fraction of atoms, in the structure is exposed to the gas molecules. When H-Beta had a higher surface area than H-ZSM-22, it is mainly because a higher fraction of lattice atoms are exposed to the gas in that particular topology. The main reason for measuring BET surface areas is to compare the obtained values to literature values (or theoretical values) obtained for

each topology, to elucidate whether the structure is close to perfect, or whether a significant fraction of the internal surface is blocked for gas molecules. Therefore, in all these 7 zeolite samples, a porous and open structure which is accessible by gas molecules was present.

3.3.4. Fourier Transformed Infrared spectroscopy (FT-IR)

The FT-IR spectrum of H-Mordenite, H-Beta and H-ZSM-5 are depicted in Figs 3.28, 3.29 and 3.30, respectively. In each graph, the IR spectrum of the bare zeolite structure is shown in red meaning there was no dosage of CO, hence this spectrum revealed various species on the surface. The left panel showed the O-H stretching region in the range of 3050-3800 cm^{-1}, while the right panel revealed the C-O stretching region from 2075 to 2275 cm^{-1} wavenumber for the zeolite. To see clearly what happened during CO adsorption, the graph was split into two regions; top and bottom part. The upper part in black more focused on silanol groups' shift, while the lower part in grey focused more on the bridged hydroxyl groups' shift. It is possible also to see either the peak growth or peak decay by following the arrows on the graphs.

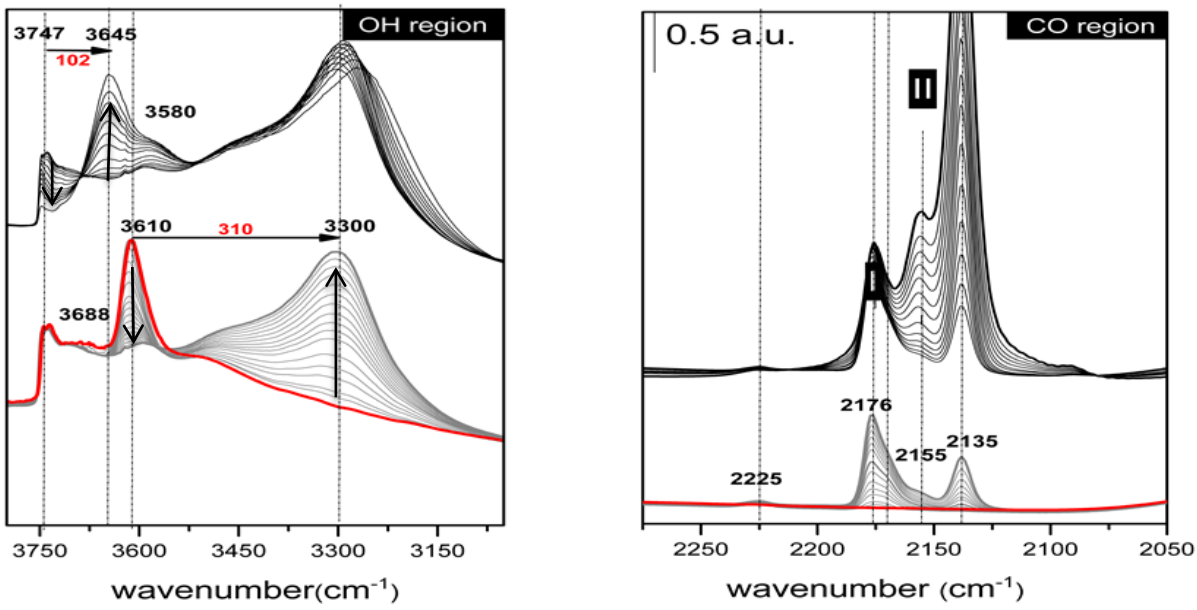

Figure 3.28: O-H (left panel) and C-O (right panel) stretching region of H-Mordenite and studying the effect of increasing dosage of CO at 77K. Red spectrum indicates to the activated sample with no dosage of CO while gray and black shows the higher dosage of CO.

The FT-IR spectra of H-Mordenite are shown in Fig. 3.28. By just focusing on the red spectrum of the Mordenite, in the O-H stretching region (left panel) the asymmetric peak at ~3747 cm^{-1} with a tail towards lower wavenumber at ~3700 cm^{-1} might be assigned to isolated/external and terminal/internal silanol groups, respectively [83]. Small peaks at ~3688 cm^{-1} were attributed to the hydroxyl groups attached to the extra framework aluminium species [46]. From this spectrum, a sharp peak centred at ~3610 cm^{-1} was assigned to bridged hydroxyl groups, Si(OH)Al, named as Brønsted acid sites. The general shape and placed peaks of IR adsorption bands for the clean activated H-Mordenite is in good agreement with previous literatures [83-86].

The asymmetric peak at ~3610 has been reported previously for various zeolite topologies [58, 59, 62, 83, 86-89]. Various interpretations could be thought for this band broadening. It might be related to extra framework species or interaction of bridged hydrogen and oxygen atom, or could be originated from the inhomogeneous distribution of Al cation in the framework [84, 88]. It was previously shown by researchers from different groups that the band at ~3610 cm^{-1} consists of two separate bands; first centred at 3612 cm^{-1} and the second with lower frequency at 3585 cm^{-1}. The first band assigned to the acidic hydroxyl vibration in the main 12-ring channels, while the low-frequency component was related to hydroxyls placed in smaller channels/side pocket where also difficult to access. This would be the case here as well, as asymmetric peak at ~3610 cm^{-1} has a tail towards lower frequencies which can be divided into two components mentioned above. As the peak at 2225 cm^{-1} in CO region also confirmed the presence of these species (see Fig. 3.12. right panel).

In Fig. 3.28 left panel bottom part, with increasing the dosage of CO first Brønsted acid sites started to interact with CO via hydrogen bonding and the frequency of their OH band shifted to lower wavenumber. Thus, Brønsted acid sites at ~3610 cm^{-1} eroded and new peak as a result of OH…CO interactions appeared at ~3300 cm^{-1}. Although the peak at ~3610 cm^{-1} disappeared completely upon the high dosage of CO, but the small band at ~3584 cm^{-1} did not totally deplete even in high dosage of CO. As discussed before, this band attributed to Brønsted sites placed in the side pocket/small pores and might not accessible by CO molecules. The similar observations were reported before for other zeolite structures as well [83, 86, 88, 90]. Also there is a possibility that the extra-framework species such as cations blocked some channels and made a fraction of Brønsted sites become isolated [77]. Via CO adsorption on H-Mordenite, Brønsted acid sites experienced a shift of $\Delta\bar{\nu}$ = -310 cm^{-1} in frequency. At higher dosage of CO showed at top-left part of Fig. 3.28, silanol groups started

to interact with CO. Via this interactions of Si(OH)…CO molecules, O-H frequency assigned to silanol groups at ~3747 cm^{-1} shifted to lower frequency at ~3645 cm^{-1} ($\Delta\bar{\nu}$ = -102 cm^{-1}).It is also worth to note that a small fraction of silanol groups became unperturbed even at very high dosage of CO, which might suggest that this fraction existed at locations where not accessible by CO probe molecules [46, 77].

The right panel of Fig. 3.28 shows the C-O bond frequency range. Again, the red spectrum showed the sample before CO introduction, black and thick black lines correspond to lower and higher dosage of CO. A asymmetric band at ~2176 cm^{-1} is related to CO interacted with Brønsted sites, while the adsorbed CO on silanol groups showed a peak at ~2155 cm^{-1}. Small peak at ~2225 cm^{-1} is due to CO adsorbed on Al^{3+}. The physisorbed, liquid-like CO molecules in Mordenite channels are assigned with a peak at ~2135 cm^{-1} similar to the complex IR peak at 2138 cm^{-1} previously reported by Bordiga et al. [83].

Fig. 3.29 shows FT-IR spectra of the H-Beta zeolite. A red spectrum was attributed to the activated sample with no dosage of CO which revealed three main surface species as follows; silanol groups at ~3740 cm^{-1}, a range of small peaks around ~3680 cm^{-1} assigned to extera-framework Al and the bridged hydroxyl group (Brønsted acid sites) at ~3611 cm^{-1}. The asymmetric peak of silanol showed an intensive peak at ~3749 cm^{-1} and a tail towards lower frequency at ~3740 cm^{-1}, which were possibly attributed to external and internal silanol groups, respectively [46].

From left-bottom part of Fig. 3.29, first Brønsted sites at ~3611 cm^{-1} perturbed which led to a shift of $\Delta\bar{\nu}$ = -315 cm^{-1} with a new band appeared at ~3296 cm^{-1} at lower dosage of CO. The shifted peak also showed a tail towards higher wavenumber ~3450 cm^{-1} which may be either due to inhomogeneity of the Brønsted sites or perturbation of the extra framework Al sites [77]. However, the second choose might be the case as the peak at ~2228 cm^{-1} in CO region (see right panel) also was another indication for existence of these surface species. Silanol groups were perturbed after Brønsted sites and shifted from ~3749 cm^{-1} to ~3655 cm^{-1} via CO…(OH)Si interactions.

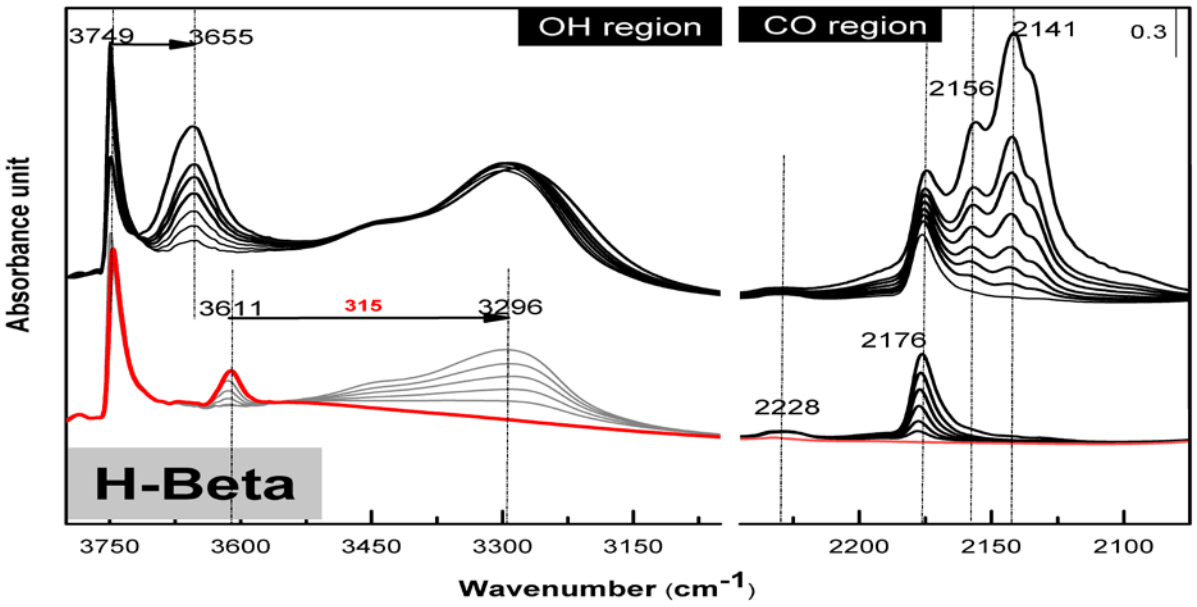

Figure 3.29: O-H (left panel) and C-O (right panel) stretching region of H-Beta and studying the effect of increasing dosage of CO at 77K. Red spectrum indicates to the activated sample with no dosage of CO while gray and black shows the higher dosage of CO.

In the CO stretching region (right panel of Fig. 3.29), the red spectrum corresponds to bare H-Beta zeolites with no IR peaks. A small peak at ~2228 cm^{-1} is assigned to CO molecules adsorbed on the extra-framework species. Upon CO dosing (black spectra), a band at ~2176 cm^{-1} assigned to vibrational mode of CO…Brønsted side interaction appeared. A peak at ~2156 cm^{-1} at higher dosage of CO showed CO…(OH)Si interactions. Again the peak at ~2141 cm^{-1} was attributed to liquid-like CO in the channels.

Fig. 3.30 displays IR spectra for H-ZSM-5 zeolite. The red spectrum revealed three main surface species of silanols, extra framework Al and Brønsted sites at ~3749, ~3680 and ~3618 cm^{-1}, respectively. With increasing dosage of CO, first Brønsted sites became perturbed (see bottom-left part in black) via CO…Brønsted sites interactions and shifted to a peak at ~3305 cm^{-1}. This asymmetric peak with a shoulder at around ~3450 cm^{-1} is attributed to extra framework Al [46, 77]. Afterwards, silanol groups interacted with CO while shifted to a peak at ~3450 cm^{-1}.

In the ν(CO) region at right panel of Fig. 3.30, peaks at ~2175 and ~2156 cm^{-1} are assigned to vibrational mode of CO interacted with Brønsted sites and silanol groups, respectively. Peak at ~2137 cm^{-1} is attributed to the condensed phase of CO similar to ones previously described for H-Mordenite.

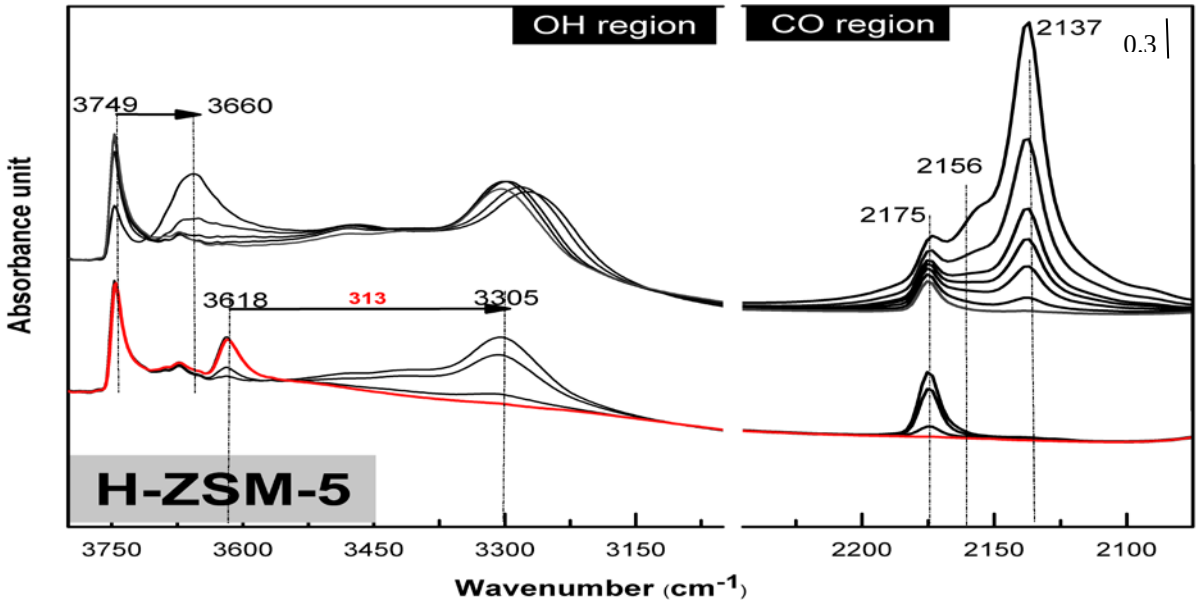

Figure 3.30: O-H (left panel) and C-O (right panel) stretching region of H-ZSM-5 and studying the effect of increasing dosage of CO at 77K. Red spectrum indicates to the activated sample with no dosage of CO while gray and black shows the higher dosage of CO.

For four other zeolites; H-ZSM-22, H-ZSM-23, H-IM-5 and H-ITQ-13 the IR spectra can be found in appendix 1. The IR experiments for these four zeolites were performed in parallel studies done by S. Kwak [46] with the same IR apparatus and in the same condition.

Table 3.4 summarised of data obtained by IR experiments for all 7 zeolites; H-ZSM-22, H-ZSM-23, H-Mordenite, H-IM-5, H-ITQ-13, H-Beta and H-ZSM-5. For all 7 studied zeolites, the silanol, extra framework Al were observed with peak in the range of 3747-3749 cm^{-1} and 3665-3688 cm^{-1}, respectively. Brønsted acid sites were detected in the zeolites with a peak appeared in the range of 3605-3618 cm^{-1}wavenumber. Upon CO dosing, different acid sites were perturbed and showed different shifts in wavenumber via the interaction with CO molecules. As CO interacted with OH of different groups, the vibrational frequency of O-H bond became smaller meaning more restriction for O-H vibrational mode. The stronger the interaction, the larger the shift would be. The first spices which interacted at lower dosage of CO, were Brønsted acid sites and probably extra framework Al species. Afterwards, the silanol groups started to interact and shifted to lower frequencies. The calculated O-H shifts for the studied zeolites were summarized in Table 3.4. Upon these data, the strength of Brønsted acid sites can be sorted as follows:

H-ZSM-23 > H-ZSM-22 = H-Beta > IM-5 = H-ZSM-5 > ITQ-13 > H-Mordenite

However acid strength values only showed 7% variation between the strongest Brønsted sites of H-ZSM-23 compared to the weakest sites of H-Mordenite, which is negligible. The approximate relative intensities of silanol over Brønsted acid sites might be helpful to have a quantitative comparison of particle size of these zeolites. From these ratios, the particle size of the samples can be sorted as follows:

H-ITQ-13 > H-Beta > H-ZSM-5 > H-ZSM-23 ~ IM-5 > H-ZSM-22 > H-Mordenite

Table 3.4: A Summary of obtained values via FT-IR experiments of 7 zeolites.

sample	ν **(silanol)**	ν**(EFAl/Al^{3+})**	ν **(Brønsted sites)**	ν **(Lewis sites)**	**OH shift**	$\frac{I(silanol)}{I(Brønsted)}$
ZSM-22*	3747	3673	3605	-	-315	~ 1.4
ZSM-23*	3749	3665	3610	-	-320	~ 2.1
Mordenite	3747	3688	3610	2225	-298	~ 0.6
IM-5*	3749	3672	3615	2229	-313	~ 2.1
ITQ-13*	3739	3670	3619	-	-305	~ 10
Beta	3749	3670	3611	2228	-315	~ 4.2
ZSM-5	3749	3666	3618	-	-313	~ 2.6

*samples were characterized by S. Kwak[46]

3.4. Summary of the characterization part

As the main goal of this project is to make a quantitative comparison of the life-time stability of different zeolites during Methanol-To-Hydrocarbons (MTH) reaction, in this section a summary of data obtained by different characterisation analyses are listed. The aim of the comparison of characterization data is to elucidate which parameters vary between these studied zeolites that might lead to different catalytic performance during the MTH reaction. The parameters such as acidity: density and strength of acid sites, presence of defects or other acid sites, crystal/particle size, and specific surface area of the zeolites were thought of as the main parameters influence on catalytic performance [8, 13, 45, 48, 76, 78, 79, 91-96]. Therefore, the quantitative comparisons of these parameters that varied between zeolite samples are shown here.

3.4.1. Si/Al ratio

The obtained Si/Al ratios from; provider, EDS, and pyridine-IR for the studied zeolites; H-ZSM-22, H-ZSM-23, H-Mordenite, H-ITQ-13, H-IM-5, H-Beta and H-ZSM-5, are shown in Table 3.5. From data, H-ZSM-22 and H-Beta contained the highest and lowest Si/Al ratio, respectively. The Si/Al ratio might be related to number of acid sites present in the structure meaning that the higher the Si/Al ratio, the less acid sites present in the zeolite structure. Although this ratio give an estimation of number of acid sites, but it would not distinguish between the different acid sites: Brønsted and Lewis acid sites, framework and extra-framework and accessible and non-accessible species as will be considered in the next paragraph.

Table 3.5: Si/Al ratio for 7 studied zeolites obtained from supplier, EDS analyses and pyridine adsorption.

sample	Si/Al (given by producer)	Si/Al (EDS)	Si/Al (pyridine adsorption)*
ZSM-22*	45	33	49
ZSM-23*	23	22	-
Mordenite	22	15	20
IM-5*	15	15	19
ITQ-13*	50	30	31
Beta	13.5	15	14
ZSM-5	45	32	43

****data obtained by S. Kwak[46]***

3.4.2. Acidity

Table 3.6 gives a summary on acid properties of H-ZSM-22, H-ZSM-23, H-Mordenite, H-ITQ-13, H-IM-5, H-Beta and H-ZSM-5. The acidity consists of two different concepts; acid strength and acid density/concentration [97]. The acid strength of the zeolites was obtained by IR-CO analyses considering the frequency shift of the bridged OHs via CO interaction. The bigger the shift, the stronger Brønsted acid sites present in the zeolite structure [10, 11, 97, 98]. In Table 3.6, data showed maximum 7% variation of $\Delta\nu_{(OH)}$ between the zeolites, which is not considerable. Thus, with a good approximation it can say that the acid strength of all 7 zeolites were similar.

Turning to concentration of acid sites, which were calculated by IR-pyridine adsorption by S. Kwak [46] showed different values for various zeolites as indicated in Table 3.6. Lewis acid sites as Al^{3+} framework, extra-framework Al-oxides as well as other defects/cations were presented in all samples [99]. Relative high concentration of Lewis acid sites were calculated for H-Beta and H-IM-5 samples as 0.4 and 0.2 (mmol/g), respectively while other samples contained 0.1(mmol/g) or even lower concentration of Lewis acid sites. The concentration of Brønsted acid sites varied slightly as follows:

H-Mordenite > H-Beta > H-IM-5 >> H-ITQ-13 >> H-ZSM-22 = H-ZSM-5 > H-ZSM-23

Table 3.6: Acid proprty of 7 studied zeolites

sample	Acid strength of Brønsted sites ($\Delta\nu_{OH}$) (cm^{-1})	Concentration of Brønsted acid sites* (mmlo/g)	Concentration of Lewis acid sites* (mmol/g)
ZSM-22*	- 315	0.287	0.047
ZSM-23*	-320	0.236	0.039
Mordenite	-298	0.714	0.068
IM-5*	-313	0.614	0.216
ITQ-13*	-305	0.422	0.105
Beta	-315	0.695	0.414
ZSM-5	-313	0.277	0.103

****data obtained by S. Kwak[46]***

The characterisation of acid sites was performed by probe molecules, CO and pyridine, so the obtained values can be considered as the accessible acid sites in these zeolites. As the kinetic diameter of both; CO (~ 3.76Å) and pyridine (~ 6Å), are larger than methanol (~3.6 Å) as the MTH reactant, these acid sites could be accessible for methanol during the MTH reaction as well. Comparison between the acid site density obtained by Pyridine measurement and EDS

revealed that some of the Al atoms were extra-framework, belonged to the other phases or even not accessible by molecules which cannot participate into MTH reaction.

3.4.3. Crystal size and surface area

Table 3.7 shows data obtained from various characterisation analyses relating to crystal/particle size and surface area measurements. Relative intensity of silanol (external/isolated) over Brønsted acid sites obtained from IR-CO measurement might be useful to estimate the particle sizes. As the external silanol groups terminate the zeolite lattice, the higher ratio might be obtained with smaller particles [100]. Thus, Mordenite sample has the largest particles due to the lowest IR relative intensity of external silanol over Brønsted acid sites.

SEM and XRD measurements also confirmed the values obtained by IR-CO. All the methods showed the largest particles for H-Mordenite and H-ZSM-22 and the smallest particles for H-Beta samples, while H-ZSM-23, H-IM-5, H-ITQ-13 and H-ZSM-5 appeared with almost the similar particles sizes. SEM gave almost 10 times higher value for particle size than those obtained by XRD measurements, see Table 3.7. Thus, the micrographs of SEM showed agglomerates or particles size while by XRD and using the Scherrer Eq. (see section 3.1) the size of individual crystals can be calculated.

The surface area measurement using BET method showed the highest surface area for H-Beta zeolite, while the lowest surface area measured for H-ZSM-23. The order of specific surface area varied over different zeolite samples as follows:

Beta > Mordenite > IM-5> ITQ-13 > ZSM-5 > ZSM-22 > ZSM-23

Table 3.7: particles and surface area property of the studied zeolites obtained by different characterisation techniques.

sample	$I_{(silanol)}/I_{(Brønsted)}$ (FT-IR)	Particle size (SEM, µm)	Crystal size (XRD, nm)	Surface area (m^2/g)			
				S_{BET}	S_{int}	$S_{int}/S_{BET(\%)}$	S_{ext}
ZSM-22	~ 1.4	0.2	17	217	197	91	20
ZSM-23	~ 2.1	0.1	10	159	103	65	56
Mordenite	~ 0.6	0.3	22	576	532	93	44
IM-5	~ 2.1	0.1	10	482	364	76	118
ITQ-13	~ 10	0.1-0.2	13	461	421	91	40
Beta	~ 4.2	0.05	6	713	495	70	218
ZSM-5	~ 2.6	0.1	9	422	309	73	113

In addition t-plot method was used to calculate the $S_{internal}$ /S_{BET} surface area as it is important factor in catalytic reactions. The uncertainty using this method was really high in case of H-ZSM-22, H-Mordenite and H-ITQ-13 [57], but for other zeolites the ratio of $S_{internal}$ /S_{BET} were obtained with rather good accuracy. Thus, rather high ratio of the total surface was attributed to internal surfaces (~70%) in H-ZSM-23, H-IM-5, H-Beta and H-ZSM-5. The hysteresis loop at relative high pressure revealed the presence of mesopores, especially in H-ZSM-23, H-IM-5 and H-ZSM-5.

XRD diffractograms revealed no background in the range of 2θ =15-25° which is an indication of non-crystalline impurities [101]. Powder XRD patterns of theses zeolites also approved presence of the desired phase in each zeolite samples. The size and shape of crystals/particles might cause some diffusion limitations. Products and intermediates in a zeolite with small crystals can diffuse out of the channels easier than in case of bigger crystals. Also in a sample with rather larger crystals size, it takes a while for those components to find their way to diffuse out and this increases the residence time and probability of secondary reactions which lead to deactivation of catalyst [102]. The mesoporosity in ZSM-5 zeolite can increase the catalyst lifetime in MTH reaction even by factor of three compared to the similar zeolite with only micropores, reported by Ryoo and co-workers [101]. They declared that by presenting mesopores the coke species deposits on the mesosopores walls, while having only micropores lead to heavy coke formation inside the micropores. The short path length in meso structure speeds up the molecular diffusion which then have effect on the lifetime catalyst [101].The number of acid sites as well as their concentrations might have negative effects on catalysts stability [31]. The Bulkier components may block the pores and made a catalyst deactivated are formed via a series of reactions, most of them need more than one acid site. As the number of active acid sites increases, Si/Al ratio decreases, the probability of those secondary reactions are also increases. Thus, higher number of acid sites might lead to faster deactivation.

In conclusion, all characterized samples had an open and accessible pore structure with pure and crystalline phase. The zeolites had a similar acid strength but differed in acid sites density. Brønsted acid sites were present in all zeolite samples. Most of zeolites had similar particle size except for H-Mordenite and H-ZSM-22 where bigger particle size than other samples were present.

Catalytic part

Chapter4: Catalytic testing

4.1. Theory

Several catalytic tests were conducted to study the lifetime stability of various zeolite topologies; H-ZSM-22, H-ZSM-23, H-Mordenite, H-IM-5, H-ITQ-13, H-Beta and H-ZSM-5. In this section, first the theoretical backgrounds relate to catalytic testing are presented followed by experimental procedures and relevant product parameters together with mathematical calculations, which will be use in discussion while comparing different zeolite structures.

4.1.1. Reactor

Selection of reactor requires more attention to be paid. To achieve a reliable and reproducible data many factors should be taken into account in order to choose the best suited reactor for a particular catalytic study. Beside these, the purpose of experiment, the physical nature of the reaction system and the ease of construction and operation as well as cost efficiency should be taken care. In laboratory studies, it is mostly interested to operate the catalytic tests on the steady-state condition without any concentration or temperature gradients, result in to choose Continuously Stirred Tank Reactors (CSTR) and Plug Flow Reactors (PFRs) over batch, fluidized-bed, bubble column and trickle-bed reactors [103].

In this study, all the reactions were performed in a homemade quartz U-shaped PFR reactor (also see Fig. 4.7). A close attention should be paid to have an ideal flow pattern through the reactor as depicted in Fig. 4.1. Thus the diameter of the PFR reactor must be at least 10 times larger than the catalyst particle sizes to eliminate the influence of the reactor wall effects on the flow pattern.

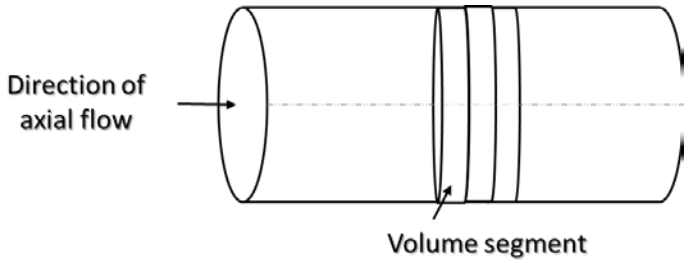

Figure 4.1: A schematic of Plug-flow reactor.

4.1.2. Oven

To assess the catalyst lifetime, it is important to find out the isothermal zone of the oven. It can be seen from Fig. 4.2 that relatively small changes in temperature can affect reaction rates significantly [103]. For instance, for a hypothetic reaction at 400 °C only 3°C deviation from the operating temperature might cause 10%, 20% or even higher error while the activation energy increasing to 30, 40 (kcal/mol) and bigger numbers, respectively.

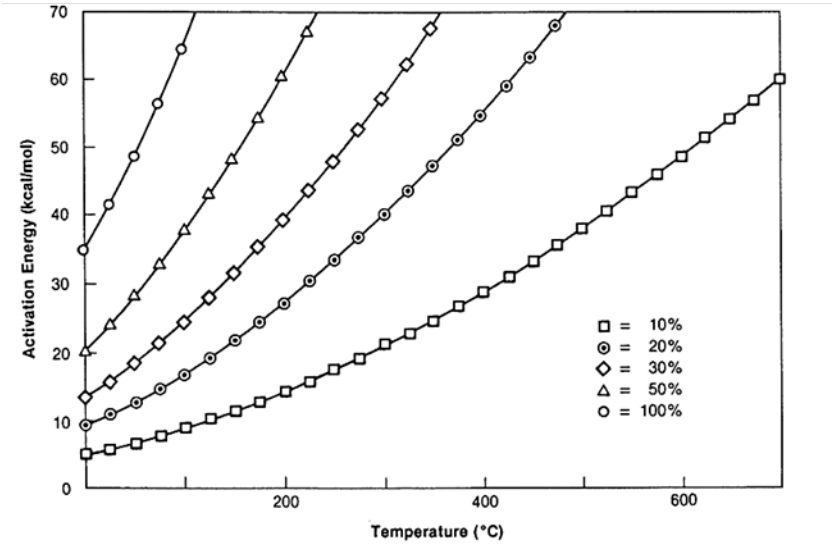

Figure 4.2: Graph shows how big is the error for 3°C deviation in temperature for reactions at different temperature and activation energy [47].

On the other hand, to avoid further reactions between the products in the U-shaped reactor, it is necessary to determine the isothermal zone of the oven and always place the reactor in the same position for all of catalytic reactions. Therefore, the isothermal zone of the oven was

obtained while the reactor was placed in the oven, with/without Helium flow and reported in Appendix 2.

4.1.3. Saturation evaporator

Saturation evaporator was designed to obtain a proper amount of methanol as feed for catalytic reaction, and pictured in Fig. 4.3. A distinct flow of inert gas (Helium) was bubbled through a liquid methanol to get a desired weight space velocity (WHSV) of methanol. The liquid methanol was kept close to its boiling point in order to have a stable vapour pressure using a silicon-oil bath [24]. Helium saturates with methanol at atmospheric pressure while passing through it. The temperature in the reflex column (20.1 °C), which is controlled by circulating cold water determines the final vapour composition. In this work using this set-up, the partial pressure of methanol was fix at 13 kPa and used as the feed for MTH reactions.

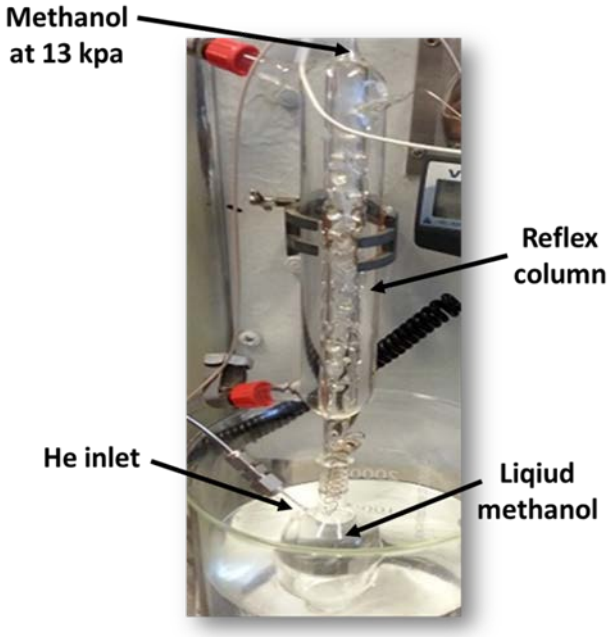

Figure 4.3: Saturation evaporator set-up used in this work

4.1.4. Gas Chromatography (GC)

Gas chromatography is a method used for quantitative and qualitative analyses of a vaporised mixture. This method is widely used to separate components of volatized mixture as a simple,

sensitive and effective technique. An inert gas either Helium or Nitrogen serves as a mobile phase carrying the analyte to the column as shown in Fig. 4.4.

The principle of gas chromatography is based on how the components are partitioned between the stationary and mobile phase in the column. There are two general types of columns: packed and capillary column with a stationary phase bounded to the tube in both types. While the mobile phase (carrier gas with analyte) passes through the column, each component of analyte interacts with the stationary phase of the column. The strength of the interactions leads to a separation based on various retention time. The stronger the interaction, the longer time takes for component to migrate through the column. In addition, temperature gradients might be used to have the best separation based on different polarities and boiling points of the components [104].

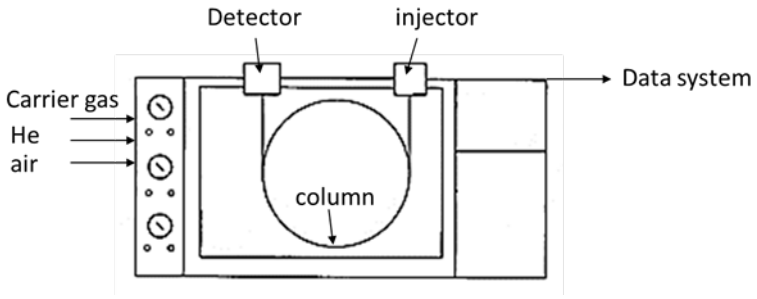

Figure 4.4: A gas chromatography instrument and its components [49]

As the sample leaves the column, it meets the detector which can detect the different components as shown in Fig. 4.5. The flame ionization detectors (FIDs) are the most common, robust and more sensitive among the other detectors. Sample passes through the column where it burns with a hydrogen-air flame and produces ions. A polarizing voltage attracts these ions to the collector where the produced current is proportional to the amount of sample being burned. The captured signal is called chromatogram as a function of retention times and intensity of each separated components [104].

In FID detector, the response factor of hydrocarbons is equal to unity; sometimes it is called equal-per-carbon response. On the other hand, for substituted hydrocarbons, oxygenate and other compounds like methanol and dimethyl ether, the response is always less than 1 [105]. From previous calibration, the response factors of methanol and dimethyl ether were

considered as 0.72 and 0.598, respectively [48]. Therefore, the obtained peak areas of methanol and dimethyl ether in chromatograms were corrected regarding to their response factors to get the actual concentrations of these compounds in the effluent as follows:

$$\text{Corrected area of methanol} = \frac{Area\ of\ methanol\ from\ chromatogram}{0.72}$$

$$\text{Corrected area of dimethyl ether} = \frac{Area\ of\ dimethyl\ ether\ from\ chromatogram}{0.598}$$

These corrected areas would be proportional to the number of carbon atoms presence in the compound. For instance, if the same area calculated for butane and ethane, the concentration of ethane would be twice much as the butane.

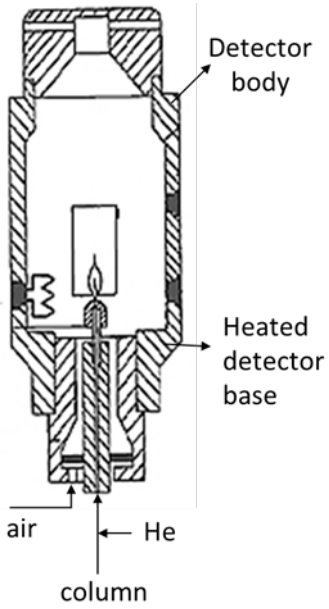

Figure 4.5: Picture of flame ionization detector [49]

4.2. Experimental Part

Fig. 4.6 shows the test rig which was designed to study the lifetime stability of zeolites during Methanol-to-Hydrocarbons (MTH) reaction. Many parameters might have influence on the catalyst lifetime. Among them: reaction temperature, partial pressure of methanol, pre-treatment condition and catalyst preparation method are the most important parameters to be considered. In order to investigate the effects of methanol flow, the above listed parameters were kept constant except the flow of methanol. A range of methanol flow might be obtained while changing the flow of inert gas (helium). Thus, the reaction temperature of 400 °C and methanol partial pressure of 13 kPa were chosen for all catalytic reactions and weight space hour velocity was changed by varying the helium flow through the saturator.

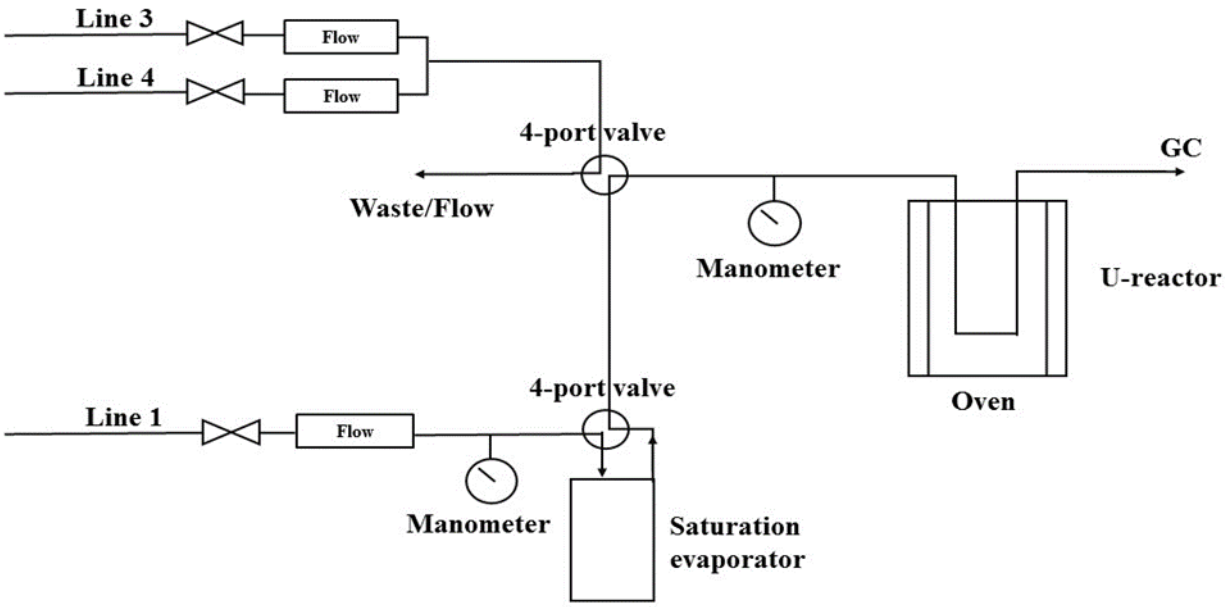

Figure 4.6: The test rig setup which was designed and used for catalytic testing.

4.2.1. Catalytic reaction procedure

The catalytic experiments were performed in a U-shaped fixed-bed quartz reactor of 8mm inner diameter as shown in Fig. 4.7.

The temperature of catalyst bed was monitored with a thermocouple covered by quartz tube which was placed exactly inside the catalyst bed as shown in Fig. 4.7. The enough amount of

sample powder was pressed and sieved several times to get particles in the range of 0.25-0.42 mm for catalytic testing. The catalyst prepared such, to avoid pressure drop during reaction. Approximately 50 mg of the prepared catalyst was poured into the clean reactor and the thermocouple was placed exactly into the catalyst bed. Then, the reactor was placed in the isothermal zone of oven when the temperature was chosen to increase up to 550 °C. In order to reduce the heat loss, the outlet of the oven was isolated each time with isolating glass-wool blankets.

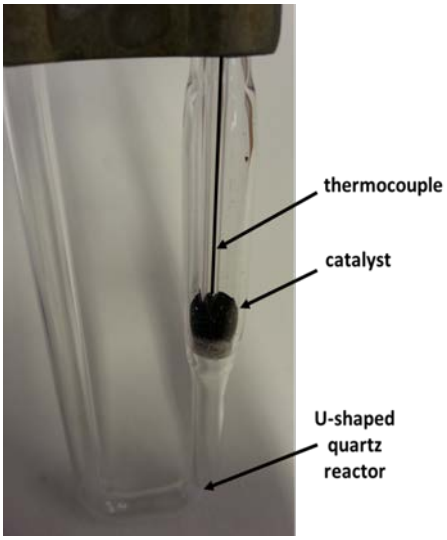

Figure 4.7: U-shaped quartz reactor used for MTH reactions.

Separate lines were designed for pre-treatment and feeding the catalyst during MTH reaction, seen in Fig. 4.6 as Line 3&4 and Line 1, respectively. Prior to the MTH reaction, it is necessary to remove the adsorbed contaminants which ingress during the handling/storage of the catalyst in order to have reproducible data. For this purpose, a flow of pure oxygen was passed over the catalyst for 1 h while the temperature was fixed at 550 °C. After the pre-treatment process was finished, a flow of helium was passed over the catalyst to remove all the oxygen out of the line while collecting the chromatogram indicates whether there is any impurity in the gas effluent or not.

During this work by checking the reproducibility of data, it was found that it is necessary to bubble the helium through the saturator for at least three hours to get a stable and desired flow of methanol (see Appendix 3). Thus, at least three hours before the MTH reaction started, a flow of He gas was passed through the saturator evaporator to get the desired methanol flow or weight hourly space velocity (WHSV). The helium flow was adjusted each time by a ball

flowmeter (porter P-150) and the corresponding flow of He/feed was monitored by an on-line digital ADM2000 Universal gas flowmeter connected to the PC. During the reaction, the temperature of feed was monitored with the thermocouple placed in the outlet of the reflex column. The temperature of reflex column was fixed at 20.1 °C by circulating cold water, so methanol obtained at partial pressure of 13 kPa. All the lines from the outlet of saturator to the inlet of reactor were rapped with heating cable and isolating wool in order to avoid condensation of methanol in the lines.

After the blank chromatogram was collected, the reaction was begun by allowing methanol feed pass over the catalyst bed. As it takes sometimes for effluent to pass through lines and reach to the detector, the GC chromatograms were begun to collect after almost 3 mins since the valve was switched to the feed.

4.3. Products analyses

MTH gas effluent were analysed by on-line gas chromatograph, Aligent 6890 A, with Flame Ionized Detector (FID), see Fig. 4-8. The FID detector was equipped by Supelco SPB-5 capillary column of 60 m length with inner diameter of 0.530 mm and 3µm thickness of stationary phase. The applied temperature was programmed between 45 °C to 260 °C increased with a ramp of 25 (°C/min) and held at 45 °C for 5 mins and 10 mins at the final temperature. This temperature program was employed to detect a wide range of compounds from light hydrocarbons like methane to heavier aromatic and aliphatic compounds such as polyaromatic and aliphatic compounds together with methanol and dimethyl ether.

Figure 4.8: Gas chromatograph instrument, Aligent 6890 A with FID detector used to analyze the gas effelunt.

The GC chromatogram of H-Beta which was collected after 36 mins of the MTh reaction might be seen in Fig. 4.9. From the chromatogram, several peaks which were assigned to a range of hydrocarbon can be found at different retention times. As mentioned in section 4.1.4, after the peaks area were corrected regarded to response factors, these areas might be used to calculate the methanol conversion as well as products concentration and selectivity. In the calculations, both methanol and dimethyl ether (DME) were considered as the reactants which can be converted to a range of hydrocarbon products over the catalyst. In the pre-equilibrium between methanol and dimethyl ether, 1 mol of water produces by converting 2 mole of methanol as below reaction:

$$2\,CH_3OH \leftrightarrow CH_3OCH_3 + H_2O$$

The reaction quotient ($Q = \frac{[DME] \times [H_2O]}{[MeOH]^2}$) of methanol and its condensation product of methanol (DME) were calculated for each test to ensure about equilibrium and absence of by-pass (see Appendix 4).

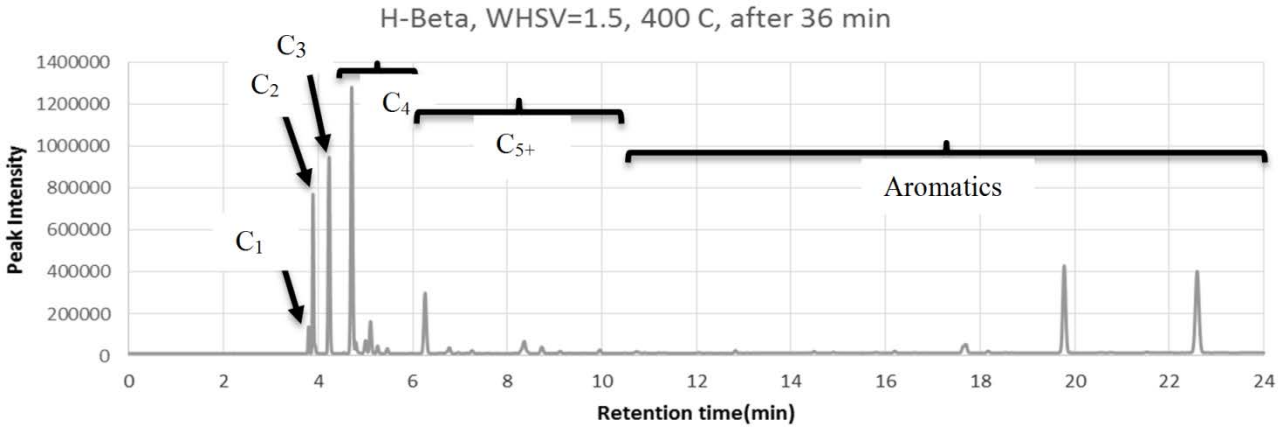

Figure 4.9: The GC chromatogram of H-Beta zeolite collected after 36 min of MTH reaction with WHSV=1.5 at 400 C.

Methanol conversion, product yield and selectivity can be calculated based on the GC-FID peak areas. The GC-FID peaks were corrected by the methanol and DME response factors and used to derive below values for conversion, yield and selectivity.

$$\text{Conversion}(\%) = \frac{\Sigma \text{ area of all compounds} - \text{area of (MeOH+DME)}}{\Sigma \text{ area of all compounds}} \times 100$$

The percentage of each product (x) can be determined by:

$$\text{Selectivity (x)} = \frac{\text{area of compound (x)}}{\Sigma \text{ area of all products}} \times 100$$

Howerever yield describes the amount of each product formed and calculated accordingly as:

$$\text{Yield (x)} = \frac{\text{Conversion} \,.\, \text{Selectivity(x)}}{100}$$

Catalytic Results And Discussions

Chapter5: Catalytic results and discussions

This chapter presents the results and discussions of the MTH catalytic tests over different zeolite topologies. The main goal of this project is to make a quantitative comparison of the life time stability of the materials studied as MTH catalysts. The second goal of this work is to elucidate whether the autocatalytic deactivation model is globally valid by extending the experimental basis for such studies to other topologies than those previously studied or not and investigating the possible limitations for this deactivation models. Thus, the results and followed discussions are presented in separate parts as catalyst lifetime and conversion capacity, selectivity and the yield of hydrocarbon products. In each section, the materials are further separated into: 1D (H-ZSM-22, H-ZSM-23 and H-Mordenite) and 3D zeolites (H-IM-5, H-ITQ-13, H-Beta and H-ZSM-5). In the last part, the characterisation results of the spent catalysts are presented followed by a discussion part relates to the Autocatalytic deactivation model.

5.1. Catalyst lifetime

The stability of a catalyst during the MTH reaction and its resistance against deactivation are sometimes presented by plotting methanol conversion versus time-on-stream. The catalyst lifetime is defined as the time taken to reach a given conversion level [40]. Therefore, the total catalyst lifetime is the time to reach almost zero methanol conversion in the fix-bed reactor working at fixed temperature and WHSV.

5.1.1. 1D zeolites: H-ZSM-22, H-ZSM-23 and H-Mordenite

Figure 5.1.a-c shows the methanol conversion as a function of time-on-stream for H-ZSM-22, H-ZSM-23 and H-Mordenite at different weight hourly space velocity (WHSV) and 400 °C. During the MTH reaction, the methanol partial pressure was set to constant at 13 kPa. For each zeolite topology three different WHSVs were selected such that the MTH reaction

started with almost 100% methanol conversion. This was achieved by alternating the flow rate of He gas rather than varying the catalyst mass [41].

As seen from the below graphs, the lifetime of catalyst varied by either feed rate or zeolite topology used [36]. H-ZSM-22 was tested with space velocities of 0.97, 1.47 and 1.97 $gg_{cat}^{-1}h^{-1}$ and the corresponding lifetimes are depicted in Fig. 5.1.a. The MTH reaction started with 100% initial conversion and it declined sharply after 1 h with WHSV=0.97 $gg_{cat}^{-1}h^{-1}$ and became deactivate within 18 hours since the reaction began. The plotted curves for H-ZSM-22 at various space velocities suggest that with higher space velocity, the catalyst became deactivated faster. Total lifetime of H-ZSM-22 was calculated as ~18, ~10 and ~9 hours with space velocities of 0.97, 1.47 and 1.97 $gg_{cat}^{-1}h^{-1}$, respectively. Teketel et al [77] calculated the lifetime of ~ 5 hours over H-ZSM-22 to 15% methanol conversion with space velocity of 2.05 $gg_{cat}^{-1}h^{-1}$ and 400 °C in good agreement with the lifetime obtained here.

In case of H-ZSM-23 (Fig. 5.1.b), the initial conversion at 100% declined with milder slope than H-ZSM-22. This zeolite was tested at feed rates of 1, 1.45 and 1.96 $gg_{cat}^{-1}h^{-1}$. Similar to the previous material, H-ZSM-23 deactivated faster with higher feed rates. The longest total lifetime was ~24 hours and obtained with space velocity of 1 $gg_{cat}^{-1}h^{-1}$, while with space velocities of 1.45 and 1.96 $gg_{cat}^{-1}h^{-1}$ the catalyst became deactivate after ~16 and ~12 hours, respectively. Fig 5.1.c depicts the methanol conversion as a function of time-on-stream for H-Mordenite. The catalyst was studied with three space velocities of 1.95, 2.9 and 3.87 $gg_{cat}^{-1}h^{-1}$ and very similar lifetimes (~ 4 h) were observed with all of the feed rates. High activity and short lifetime of H-Mordenite during the MTH reaction was reported by other researchers as well [71, 106]. Among these one dimensional zeolites, the shortest lifetime was assigned to H-Mordenite, while H-ZSM-23 showed the longest catalyst lifetime during the MTH reaction compared with other studied 1D materials with the same space velocity of ~ 2 $gg_{cat}^{-1}h^{-1}$.

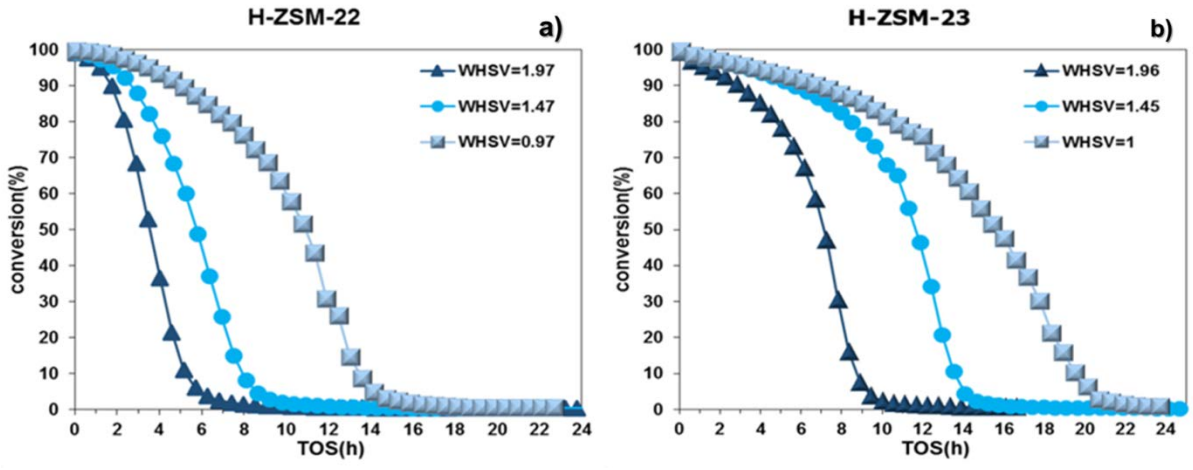

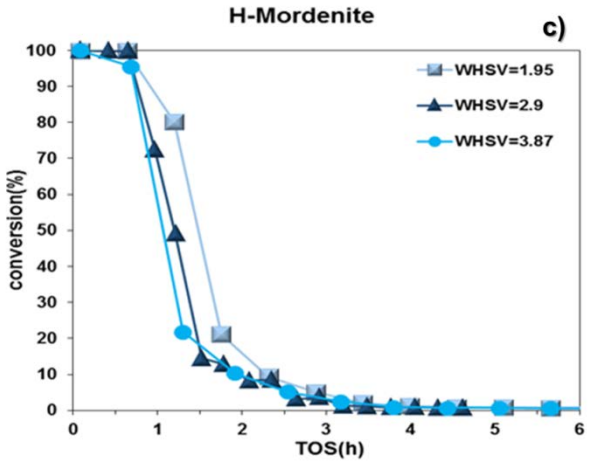

Figure 5.1: Methanol conversion as a function of time on stream (TOS) of a) H-ZSM-22, b) H-ZSM-23 and c) H-Mordenite for different WHSVs, Pp_{MeOH} =13 kPa at 400 ℃.

5.1.2. 3D zeolites: H-IM-5, H-ITQ-13, H-Beta and H-ZSM-5

The lifetime stability tests over H-IM-5, H-ITQ-13, H-Beta and H-ZSM-5 were performed and the relevant graphs are illustrated in Figs. 5.2.a-5.2.d, respectively.

Fig 5.2.a depicts methanol conversion versus time-on-stream for H-IM-5 with space velocity of 1.89, 3.93 and 7.88 $gg_{cat}^{-1}h^{-1}$. The longest lifetime obtained with the lowest feed rate (1.89 $gg_{cat}^{-1}h^{-1}$) equals to ~36 hours, while with higher feed rates of 3.93 and 7.88 $gg_{cat}^{-1}h^{-1}$ a faster deactivation and shorter lifetime of 21 and 15 hours was achieved, respectively. A steep decline in methanol conversion in a short time after the MTH reaction began was seen with WHSV=3.93 and 7.88 $gg_{cat}^{-1}h^{-1}$, while the conversion declined gradually with milder slope with space velocity of 1.89 $gg_{cat}^{-1}h^{-1}$. The lifetime graph of H-ITQ-13 is shown in Fig. 5.2.b at WHSV=1.1, 1.5 and 1.96 $gg_{cat}^{-1}h^{-1}$ and 400 °C. In case of ITQ-13, a lower initial conversion (the left-most point) was obtained with all tested space velocities which was close to 90%. Erichsen [48] related the observed differences in initial activity of the different synthesized batches of H-SAPO-5 to their differences in acid site densities; the material with relative lower acid density revealed lower initial methanol conversion. This explanation might be useful here since the H-ITQ-13 sample had relatively high Si/Al=30 or low acid site density compared to the other tested samples (see section 3.4). The conversion curve showed a gradual decline with increasing time and catalyst became totally deactivated within ~93, ~75 and ~64 hours with space velocity of 1.1, 1.5 and 1.96 $gg_{cat}^{-1}h^{-1}$, respectively.

In case of H-Beta which is depicted in Fig. 5.2.c, the conversion declined sharply from ~ 100% to 0 with tested feed rates. This material was tested with space velocity of 1, 1.45 and 1.92 $gg_{cat}^{-1}h^{-1}$ while a similar total lifetime of ~10 hours was obtained under reaction conditions. In Fig. 5.2.d, with feed rates of 9.78, 11.92 and 13.83 $gg_{cat}^{-1}h^{-1}$ over H-ZSM-5 a noticeable range with full methanol conversion in the left-most part of graph was observed. After this plateau which lasted about 15 hours' time-on-stream, the conversion declined gradually. It should be noted that the material has shown a high stability during the MTH reaction, therefore it took a long time to have full deactivation and due to time limitation of this study the reaction was stopped around 30% conversion. Accordingly, the H-ZSM-5 lifetime to 30% conversion with feed rates of 9.78, 11.92 and 13.83 $gg_{cat}^{-1}h^{-1}$ were calculated to ~ 100, 95 and 83 hours.

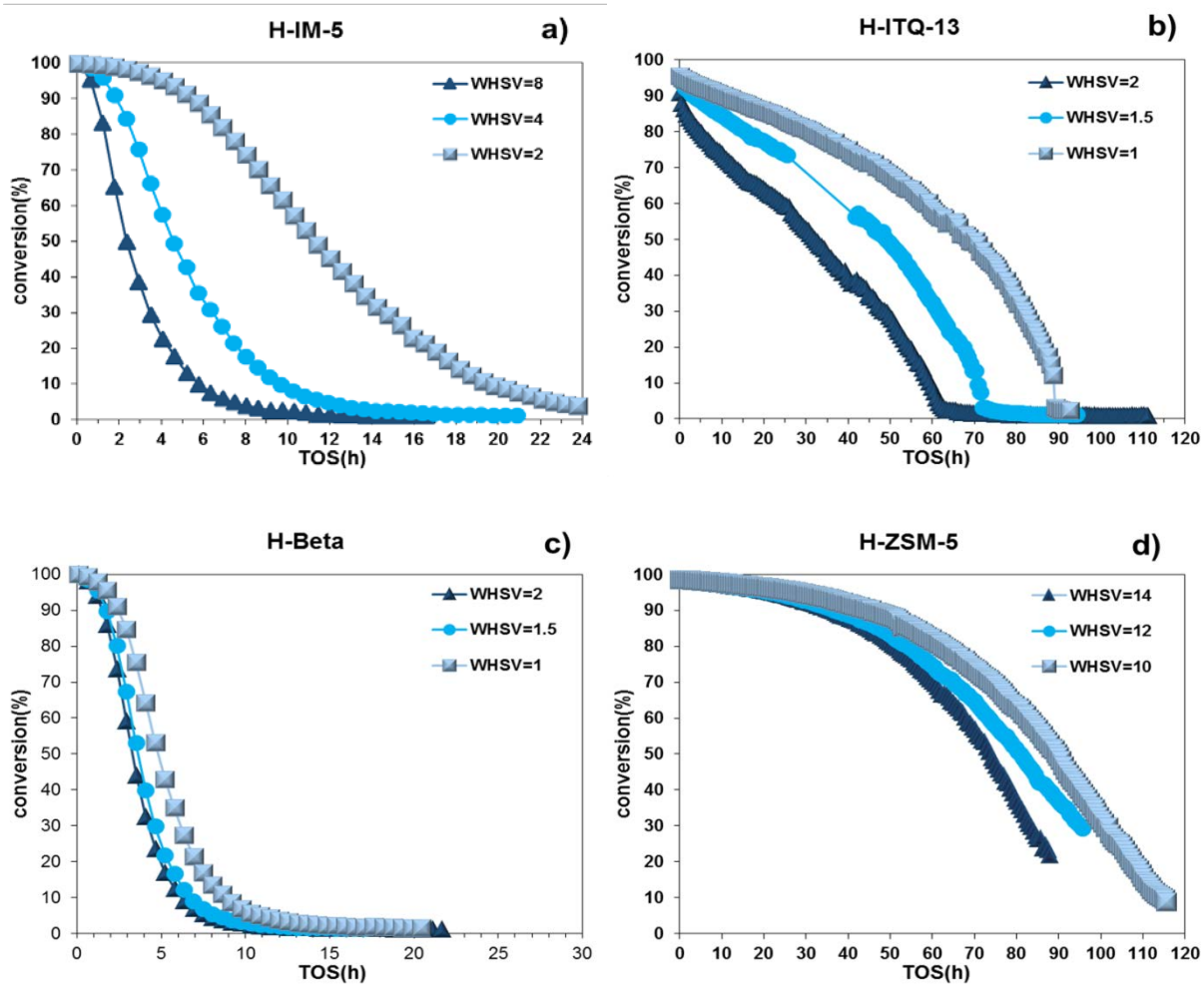

Figure 5.2: Methanol conversion as a function of time on stream (TOS) over a) H-IM-5, b) H-ITQ-13 and c) H-Beta and d) H-ZSM-5 for different WHSVs, Pp_{MeOH} =13 kPa at 400 ℃.

5.1.3. Zeolite topology and lifetime at WHSV= 2 $gg_{cat}^{-1}h^{-1}$

A comparison between the lifetime of zeolites; H-ZSM-22, H-ZSM-23, H-Mordenite, H-IM-5, H-ITQ-13, H-Beta with WHSV ~ 2 $gg_{cat}^{-1}h^{-1}$ and H-ZSM-5 with WHSV ~ 10 $gg_{cat}^{-1}h^{-1}$ at 400 °C is shown in Fig. 5-3. Thus, this test over H-ZSM-5 can only be compared to the rest of the samples only if the usage of 5 times more methanol compare to other catalysts is takinen into account.

From the graph, H-Mordenite and H-ZSM-22 with a sharp decline from ~ 100% to 0% methanol conversion exhibited respectively 4 and 9 hours of total lifetime. H-ZSM-23 with a gradual decline and H-Beta with a sharp decline in conversion with increasing time-on-stream both became totally deactivated after ~ 10 hours. Milder deactivation over H-IM-5 and H-ITQ-13 resulted in respectively 36 and 64 hours lifetime for these catalysts. The most stable catalyst during the MTH reaction was H-ZSM-5, while its conversion declined to 30% after 100 hours even with 5 times more methanol feed (WHSV= 9.78 $gg_{cat}^{-1}h^{-1}$) compared to the previous samples. Thus, the lifetime of the tested zeolites under reaction conditions decreased in the order of:

H-ZSM-5 > H-ITQ-13 > H-IM-5 > H-Beta ~ H-ZSM-23 > H-ZSM-22 > H-Mordenite

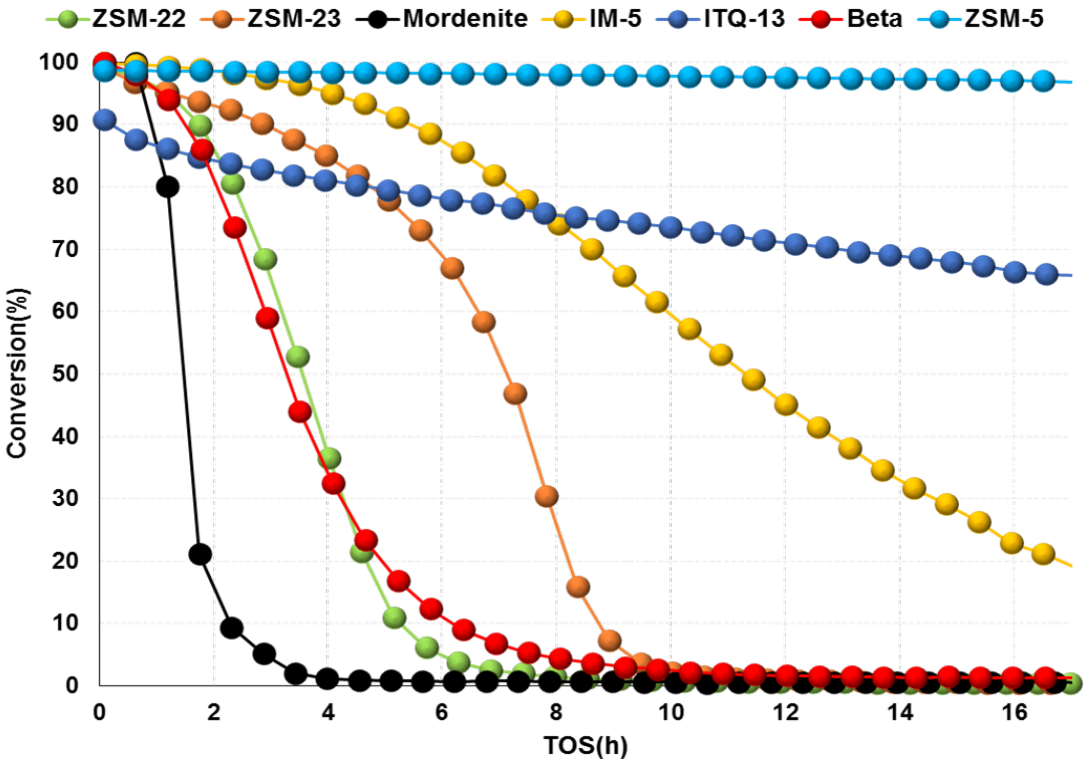

Figure 5.3: Methanol Conversion as a function of time on stream for H-ZSM-22, H-ZSM-23, H-Mordenite, H-IM-5, H-ITQ-13, H-Beta with WHSV=2 $gg_{cat}^{-1}h^{-1}$ and for H-ZSM-5with WHSV=10 $gg_{cat}^{-1}h^{-1}$, 400 °C and Pp_{MeOH} =13 kPa.

It was tempting to find the possible relations between the structural parameters and the observed lifetimes of the studied catalysts. Thus, different parameters such as acid site densities, specific surface areas and cross-section area of channel for catalysts which varied between the samples as a function of the MTH catalyst lifetime are plotted as follows:

5.1.4. Acid density, surface area, channel size and catalyst lifetime

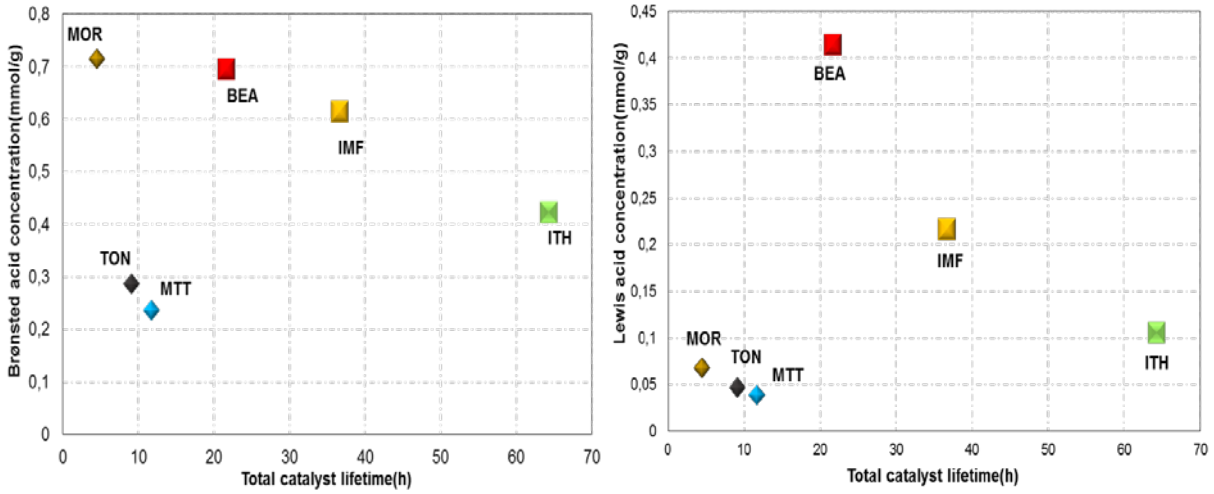

Figure 5.4: Concentration of Brønsted acid sites (left panel) and Lewis acid sites (right panel) as a function of the total catalyst lifetime for different zeolite topologies measured at WHSV=2 $gg_{cat}^{-1}h^{-1}$, 400 °C and Pp_{MeOH}=13 kPa.

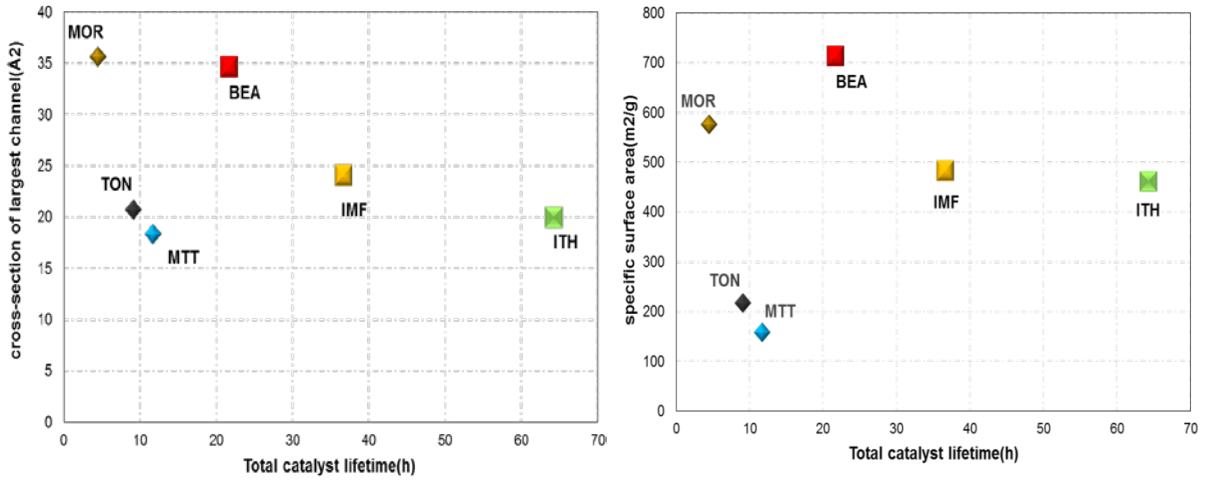

Figure 5.5: Cross-section area (left panel) and specific surface area (right panel) as a function of the total catalyst lifetime for different zeolite topologies measured at WHSV=2 $gg_{cat}^{-1}h^{-1}$, 400 °C and Pp_{MeOH}=13 kPa.

From Figs 5-4 to 5-5 it is obvious that, a straight forward relation between the acid sites density, specific surface area, the size of channels and the total lifetime of studied zeolites cannot be established. However, H-Mordenite with 12-ring channels having the highest Brønsted acid density as well as high specific surface area showed the shortest lifetime during the MTH reaction. The characterization data for this zeolite also revealed relatively bigger particle size which might also have influence on the short lifetime of Mordenite.

A good advantage for having smaller crystals is reducing the diffusion path length of methanol as the reactant in MTH reaction, which was found by Wan and coworkers [107] while studying the effect of crystal size on catalytic behaviour of H-ZSM-5 during methanol to gasoline conversion. The MFI (ZSM-5) structure with smaller crystalline size showed higher methanol conversion and less amount of coke due to the shorter path for formed intermediates to escape out of the channels [107].

On the other hand, H-ZSM-22 and H-ZSM-23 with 10-ring channels with the least acid site density and the least specific surface area showed almost equal lifetime which was slightly higher than the Mordenite lifetime. A slightly longer lifetime of H-ZSM-23 compared to H-ZSM-22, might be attributed to its relatively less acid site density, specific surface area or smaller particle size of H-ZSM-23 respect to those for H-ZSM-22. H-IM-5 (3D 10-ring channels) with rather high acid site density and medium specific surface area compared to the other studied samples, showed higher lifetime (~ 40 hours) during the MTH reaction compared to the previous samples. H-IM-5 and H-ITQ-13 possess almost the same specific surface area while H-ITQ-13 had relatively lower acid site density and smaller channel size than IM-5. These differences together with slightly smaller channel size of H-ITQ-13 (cross-section area of the largest channel is 20 $Å^2$) might be the reasons of the longer lifetime of H-ITQ-13 which was almost twice as much as H-IM-5.

In total, it is seen that H-ITQ-13 zeolite with moderate acid site densities, surface area and cross-section area displayed a long lifetime after H-ZSM-5. H-ZSM-5 excluded from the graphs because the value of total lifetime was not achievable as the reaction stopped at 30% conversion of methanol.

5.2. Conversion capacity

Methanol conversion might be studied as a function of the amount of methanol converted to hydrocarbons products over catalyst bed during the MTH reaction under the reaction conditions. Focusing on the lifetime of catalyst during MTH reactions without paying attention to methanol conversion capacity of the catalyst can be misleading [81].

Total methanol conversion capacity of catalyst can be obtained by calculating the total amount of methanol converted to hydrocarbon products just before the catalyst became totally deactivated. The cumulative methanol conversion which was defined by Mikkelsen and Kolboe [108] as: "The cumulative amount of methanol converted when x grams of methanol has been fed is given by the area under the conversion curve up to a given value of x, i.e. the integral of the conversion curve versus x.". The cumulative methanol conversion in the whole conversion range of methanol were calculated accordingly and plotted in Fig. 5.6.a-g for all 7 studied zeolites. Thus, Fig. 5.6.a-g shows the methanol conversion as a function of gram of methanol converted per gram of catalyst to hydrocarbons over 7 studied zeolites at different feed rates, 400 °C and Pp_{MeOH} = 13 kPa.

As can be seen from the graphs of H-ZSM-22 (Fig. 5.2.a) and H-ZSM-23 (Fig. 5.2.b), the cumulative conversion capacity for these zeolites were higher when a lower rate of methanol was fed over the catalyst. Consequently, for H-ZSM-22 total conversion capacity of 9.8 g_{MeOH}/g_{cat} achieved with WHSV=0.97 $gg_{cat}^{-1}h^{-1}$, while with feed rates of 1.47 and 2.12 $gg_{cat}^{-1}h^{-1}$ only 8.2 and 7.8 gram of methanol converted to the products per gram of zeolite, respectively. The obtained data is in good agreement with the reported value of 7.5 g_{MeOH}/g_{cat} for methanol conversion capacity over H-ZSM-22 tested at WHSV=2.05 $gg_{cat}^{-1}h^{-1}$ and 400 °C by Teketel [77, 91].

For H-ZSM-23 the conversion capacities varied between ~16, 15 and 13 g_{MeOH}/g_{cat} with feed rate of 1, 1.45 and 1.96 $gg_{cat}^{-1}h^{-1}$, respectively. A conversion capacity of 11.6 g_{MeOH}/g_{cat} was previously calculated by Teketel et al [91] during MTH reaction over H-ZSM-23 zeolite at WHSV=2 $gg_{cat}^{-1}h^{-1}$ and 400 °C in line with the obtained value here.

Fig. 5.2.c depicts the cumulative methanol conversion at different feed rates of methanol over H-Mordenite. The highest total conversion capacity of ~5 g_{MeOH}/g_{cat} was obtained with a feed rate of 3.84 $gg_{cat}^{-1}h^{-1}$, while reducing the space velocity to 2.92 and further to 1.95 $gg_{cat}^{-1}h^{-1}$ decreased the methanol capacity to 4 and 3.2 g_{MeOH}/g_{cat}, respectively. The conversion

capacity decreased with decreasing the space velocity in H-Mordenite, the opposite trend was observed for H-ZSM-22 and H-ZSM-23.

H-IM-5 with WHSV of 1.89, 3.93 and 7.88 $gg_{cat}^{-1}h^{-1}$ resulted in ~23, 21 and 24 gram of methanol converted to hydrocarbons per gram of catalyst, respectively. For H-ITQ-13 as is depicted in Fig. 5.2.d, the highest methanol conversion of ~65.5 g_{MeOH}/g_{cat} was attributed to WHSV= 1.5 $gg_{cat}^{-1}h^{-1}$, while changing the feed rate to 1.1 and 1.98 $gg_{cat}^{-1}h^{-1}$ decreased the conversion capacity of methanol to 62 and 61 g_{MeOH}/g_{cat}, respectively. H-Beta showed the total conversion capacity of ~ 7.5, 6.5 and 5.5 g_{MeOH}/g_{cat} with feed rates of 1.92, 1.45 and 1 gg_{cat}^{-1} h^{-1}, respectively. The total converted methanol over the fresh H-ZSM-5 to 30% methanol conversion might be derived from the Fig. 5.2.g. As the feed rate was changed to 9.78, 11.92 and 13.83 $gg_{cat}^{-1}h^{-1}$, the corresponding conversion capacities were calculated as ~788, 875 and 916 g_{MeOH}/g_{cat} which is close to 900 g_{MeOH}/g_{cat} as reported by Beleken et al [45] for conversion capacity over H-ZSM-5.

As can be seen from the graphs, in case of H-Mordenite and H-Beta zeolites, the higher conversion capacities were observed with the higher feed rate. Bjørgen and Kolboe arrived with the same conclusion while studying H-Beta during MTH reaction [81].

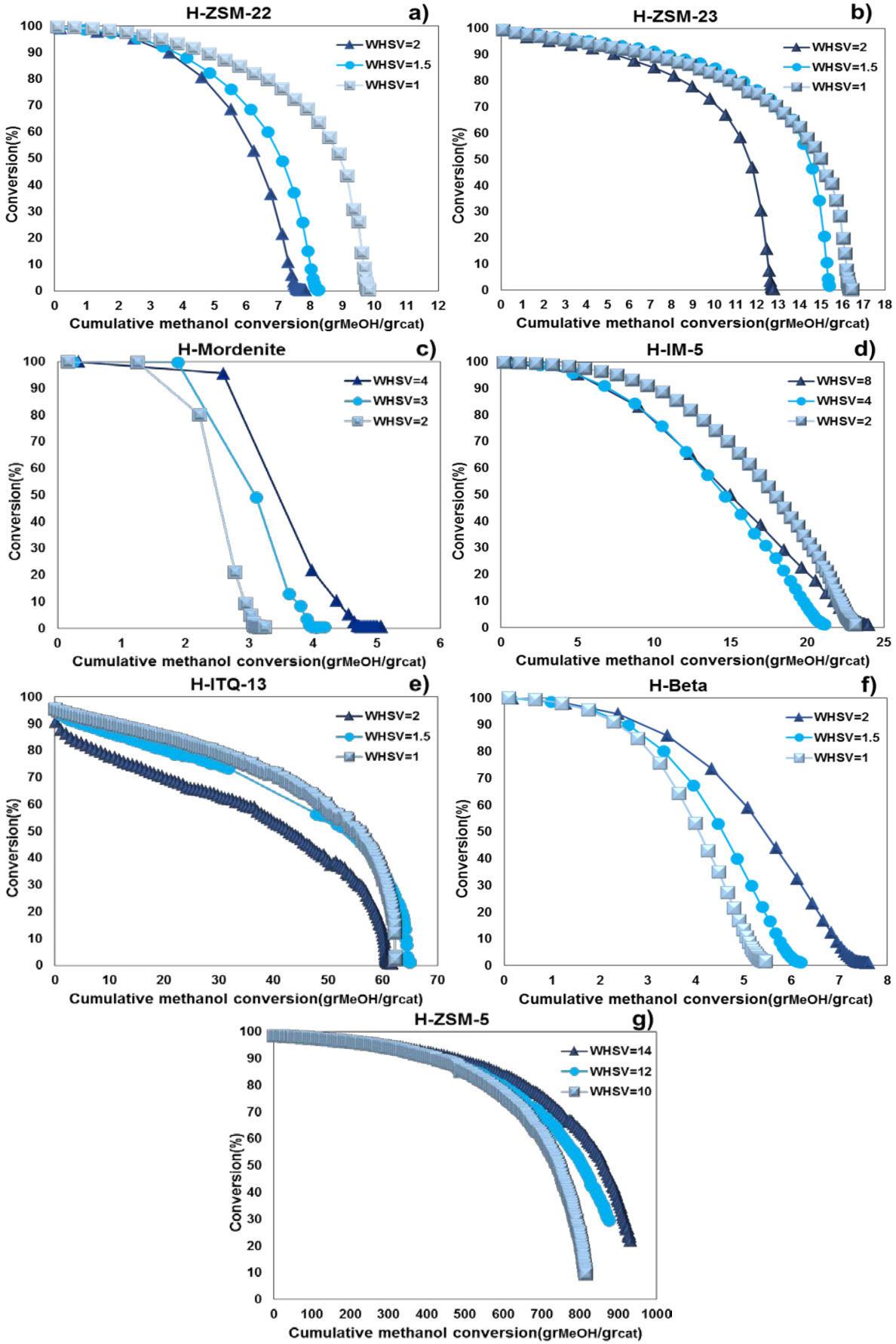

Figure 5.6: Cumulative conversion capacity of methanol for different zeolites at 400 °C and Pp_{MeOH} *= 13kPa.*

5.3. Total catalyst lifetime at WHSV=2 $gg_{cat}^{-1}h^{-1}$

5.3.1. Conversion capacity and catalyst lifetime

Fig. 5.7 depicts the relationship between total conversion capacity and total lifetime of various zeolite topologies studied with WHSV=2 $gg_{cat}^{-1}h^{-1}$, 400 °C and Pp_{MeOH}=13 kPa. It should be noted that H-ZSM-5 sample was excluded as it was tested with higher feed rates.

It is noteworthy that two lines with equal slope emerged when conversion capacity versus lifetime for 1D and 3D zeolites topologies were plotted. 1D zeolites; H-ZSM-22, H-ZSM-23 and H-Mordenite appeared with both lower total conversion capacity and shorter catalyst lifetime as compared to 3D zeolites. Another interesting feature of this graph is that Beta and ZSM-22 with different catalyst lifetime had almost the same value for methanol conversion capacity. The ITQ-13 depicted the maximum total lifetime and methanol conversion capacity among all tested zeolite topologies, while H-Mordenite appeared with the minimum lifetime and conversion capacity between these tested zeolites.

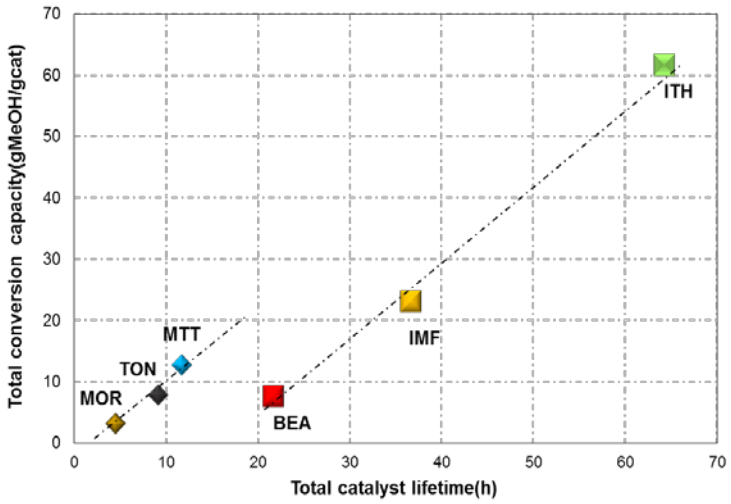

Figure 5.7: Total conversion capacity as a function of total catalyst lifetime for TON (H-ZSM-22), MTT (H-ZSM-23), MOR (H-Mordenite), IMF (H-IM-5), ITH (H-ITQ-13) and BEA (H-Beta) zeolites tested with WHSV=2 $gg_{cat}^{-1}h^{-1}$, 400 °C and Pp_{MeOH} = 13kPa. MFI (H-ZSM-5) sample excluded as it was not completely deactivate during MTH reaction and data obtained with higher feed rates than other materials.

5.4. Product Selectivities and Yields

Several consecutive and parallel reactions involve in the methanol-to hydrocarbons (MTH) processes which is initiated with methanol as a reactant [93]. The dual cycle mechanism as shown in Fig. 5.8, suggests the formation of products occur during the MTH reactions based on two cycles; alkene and aromatic cycle. In the first cycle alkenes are considered as the hydrocarbon pool species, while in the second cycle the aromatic compounds (i.e. polymetheylated benzene) are considered as the pool species. Furthermore, the methanol as the reactant continuously add to these hydrocarbon pools to produce either higher alkenes in the alkene-based cycle or higher methylatedbenzene molecules in the aromatic-based cycle. These two cycles are connected via secondary reactions e.g. cyclisation and hydride transfer reactions where higher alkenes convert into aromatic compounds and alkanes as shown in the Fig. 5.8. The alkene-cycle is mainly producing higher olefins, while the aromatic-cycle is mainly responsible for formation of light olefin (C_2 and C_3) and aromatic fractions.

In this section, it is tempting to interpret the product distributions during the MTH reaction based on this hydrocarbon pool model.

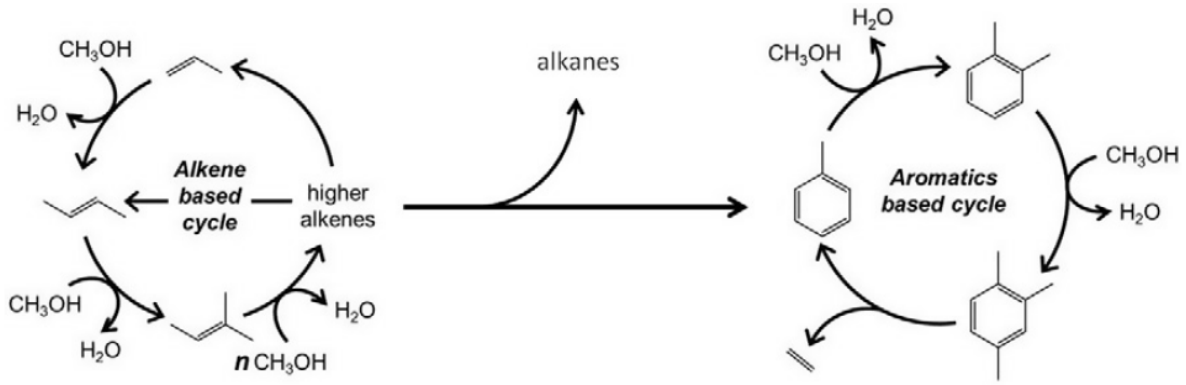

Figure 5.8: Dual cycle model proposed for the MTH reaction.

The yield versus conversion graphs can be used to distinguish between the primary versus secondary and stable versus unstable products as might be found in other literatures as well [45, 76, 109, 110]. The primary products are those compounds formed directly from methanol without any intermediates, while the secondary products are those formed via reactions where intermediates are also involved in. The stability and instability of product towards further

reactions can be investigated by considering the slope of the yield versus conversion. A stable product shows an upwards curvature with increasing conversion, while unstable product exhibits a maximum with conversion [109]. The secondary reactions become more important at higher conversion levels where high concentration of products can be found [111].

5.4.1. Product Selectivities and Yields over 1D zeolites

5.4.1.1. Product selectivities with WHSV= 2 $gg_{cat}^{-1}h^{-1}$

Fig. 5.9 shows product distributions at 80% conversion over H-ZSM-22, H-ZSM-23 and H-Mordenite with WHSV=2 $gg_{cat}^{-1}h^{-1}$ at 400 °C. Also, the products selectivities over all 7 studied zeolites in the whole methanol conversion range 0-100% can be found in Appendix 5 as well.

From the column chart (Fig. 5-9), the selectivity of different hydrocarbon products; C_1(methane), C_2 (ethane and ethane), C_3 (propene and propane), C_{4-} (Butanes), $C_{4=}$ (butenes), C_5 and C_{6+} which is split further into Aromatics and C_{6+} Aliphatics compounds, can be found at 80% methanol conversion. The product distributions over H-ZSM-22 (1D with 10-ring 5.7×4.6 Å elliptical channel) and H-ZSM-23 (1D with 10-ring 5.2×4.5 Å teardrop channel) were very similar and followed the order of: C_{6+}aliphatics > C_5 > C_3 = $C_{4=}$ > C_2 = C_{4-} . Almost zero and 1% aromatic compounds were detected over H-ZSM-22 and H-ZSM-23 zeolites, respectively. The C_3 and C_{6+} aliphatics fractions were slightly higher in H-ZSM-22, while slightly higher ~1% of C_5 and C_4 alkane were found in H-ZSM-23 compared to H-ZSM-22. In line with previous reports [77, 91] for H-ZSM-22 tested with WHSV=2 $gg_{cat}^{-1}h^{-1}$ and 400 °C, the C_{6+} fraction which only consisted of C_{6+} aliphatic compounds revealed the highest selectivity among all other products. The observations are in line with dual cycle model while consider relatively high activity for alkene cycle than arene cycle for both of the 1D structures which also resulted in high selectivity of the C_{6+}, C_5, $C_{4=}$ and C_3 fractions. On the other hand, the low (1%) and almost zero aromatics over H-ZSM-23 and H-ZSM-22 revealed a very low activity of arene-cycle over these structures. Low selectivity of C_2 also proved the low activity of arene cycle; C_2 is mainly produced by arene-cycle. The previous literatures also reported a low activity of arene-cycle over H-ZSM-22 and H-ZSM-23 [8, 13, 44, 77, 91, 92, 112].

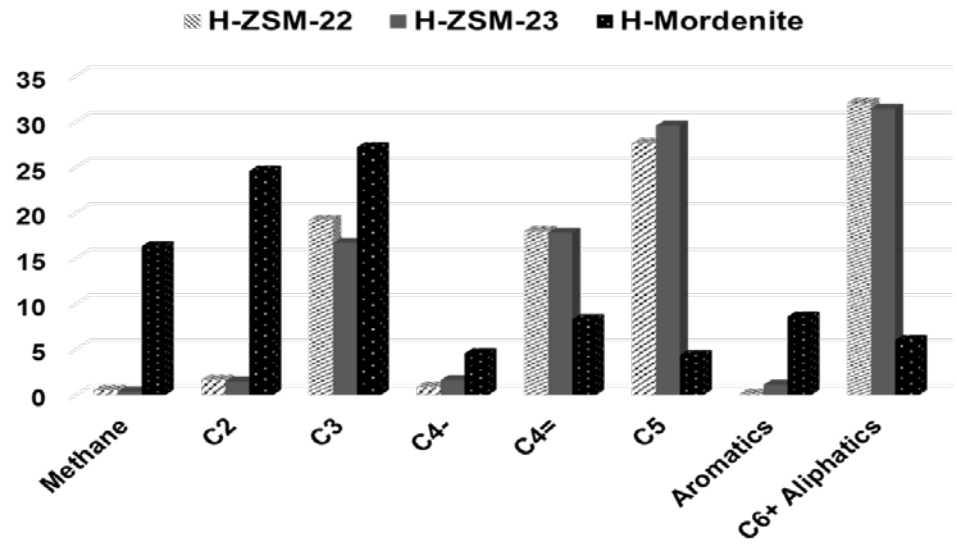

Figure 5.9: Product selectivities over H-ZSM-22, H-ZSM-23 and H-Mordenite at 80% methanol conversion with WHSV=2 $gg_{cat}^{-1}h^{-1}$, 400 °C and Pp_{MeOH} = 13 kPa.

Turning to H-Mordenite (1D 12-ring 7.0×6.5 Å channel with side pocket of 2.6×5.7 Å), a totally different product distributions than the previous structures were found at 80% conversion. The product selectivity can be divided into two groups: light aliphatics with high selectivity of ~65% in total with an order of: $C_3 > C_2 > C_1$ and the rest of products with considerably lower selectivities compared to the first group followed the order of C_{6+} aromatic = buthene > C_{6+} aliphatics > C_5 = buthane. High selectivity to C_2 might be explained by dual-cycle model where C_2 mainly produced via arene-cycle. The C_1 fraction might be formed via reaction of methanol with the surface methoxy group will be explained in section 5.8.1, together with coke species. Thus, the high selectivity of C_1 at 80% conversion where we have relatively fresh catalyst might be an indication of early coke formation. The C_3 fraction can be produced directly from the alkene-cycle or via secondary reactions e.g. cracking the higher aliphatics compounds. These higher aliphatics C_{6+} can be further convert to aromatics via cyclisation and hydrogen transfer reactions where alkane molecules such as buthane might be formed together with aromatics compounds, which is well in line with dual cycle model.

5.4.1.2. Product Yields with WHSV=2 $gg_{cat}^{-1}h^{-1}$ at 400 °C

The product yields of H-ZSM-22, H-ZSM-23 and H-Mordenite as a function of methanol conversion with WHSV=2 $gg_{cat}^{-1}h^{-1}$ at 400 °C, are illustrated in Fig. 5.10.

The similar product yields can be found over H-ZSM-22 and H-ZSM-23. The highest yield of C_{6+} aliphatics (~25%) might be achieved over both H-ZSM-22 and H-ZSM-23 at around 80% conversion, while C_{6+} aliphatics yield declined with increasing conversion to 15% at full methanol conversion. In H-ZSM-23, a small proportion of C_{6+} (~1%) were devoted to aromatic compounds, while in case of H-ZSM-22 this value reduced to ~0.1%. The yields of C_2, C_3, C_5 and C_{6+} increased linearly with increasing conversion from 0 to 70% in the order of C_{6+} aliphatics > C_5 > $C_{4=}$ > C_3 >> C_2 > C_{4-}.

Most of the products crossed the origin which is an indication of primary products. The C_{6+} aliphatics with a downwards curvature at higher methanol conversion is a primary unstable product which might participate in the cracking reactions to produce lower olefins. The same went for the C_5 fraction at the minor level. The C_3 molecules with a clearly upwards curvature especially at high conversions showed a primary and secondary stable products which may be produced in either cracking of higher olefins formed in the alkene-based cycle or dealkylation of polyaromatics formed in the arene-based cycle according to the dual cycle model. The C_2 fraction with clearly less yield compared to C_3 exhibited an upwards curvature at conversion levels exceeded 90%, an indication of the stable product. However, as the yield of C_2 is really low (< 5%) especially at lower conversion where it is almost zero, this fraction can be considered as secondary stable rather than primary product.

Analysing the product distributions over H-Mordenite is rather difficult due to its short lifetime and fewer data points obtained. However, the higher yield of aromatics and C_2 than the former structures can be an indication of higher arene-cycle activity in line with dual cycle model. As there is more space inside the 12-ring channels with a side-pocket of H-Mordenite, the aromatic cycle becomes more active. C_1 and C_{6+} aliphatics were the primary unstable products as both crossed the origin, while aromatics and C_3 were secondary stable products. The C_{6+} aliphatics may undergo cyclisation and aromatisation reactions which also increased the yield of both alkane and aromatics.

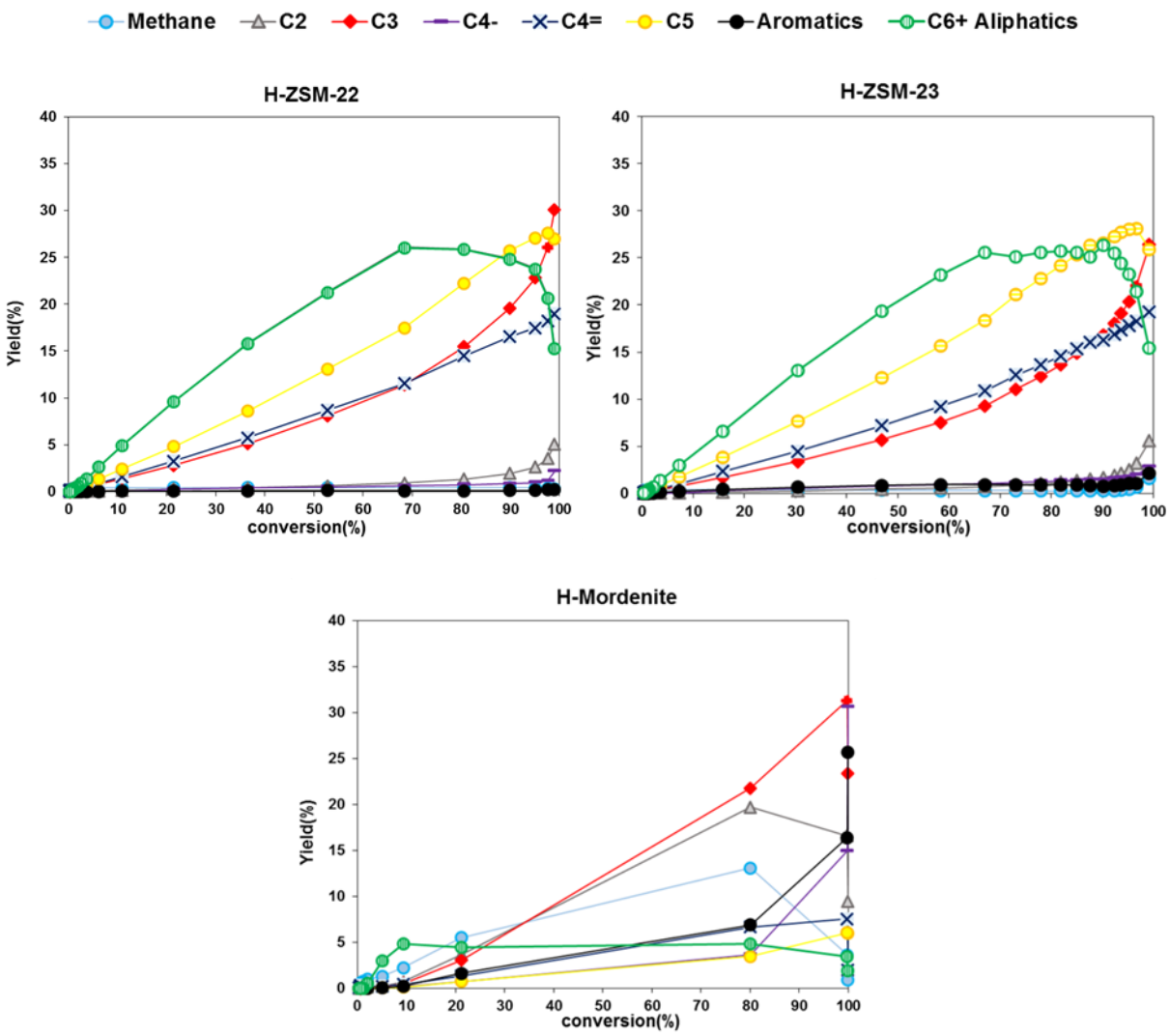

Figure 5.10: Product yields over H-ZSM-22 (top left), H-ZSM-23 (top right) and H-Mordenite (bottom) with WHSV=2 $gg_{cat}^{-1}h^{-1}$, 400 °C and Pp_{MeOH} = 13 kPa.

5.4.1.3. Coke and shape selectivity

Fig. 5.11 depicts product yields of C_2, C_3, C_4 and C_{5+}, with various space velocities (contact times) over H-ZSM-22, H-ZSM-23 and H-Mordenite at 400 °C and Pp_{MeOH} =13 kPa. In Fig. 5.11, each colour corresponds to product yield obtained with different space velocities as WHSV=1 (black), WHSV=1.5 (red) and WHSV=2 (blue). Different methanol rates over the same zeolite structure while other parameters kept constant led to different level of deactivation (see section 5.2). Thus, the purpose of this part is to elucidate whether the different feed rates which leads to different level of formed coke would affect the product selectivities or not.

For instance, for H-ZSM-23 at 20% methanol conversion the product yields were very similar with different feed rates, indicates by different colours. The similar observations obtained while changing the conversion meaning that the product yield coincided to a good extent with various space velocities.

The similar observation was found for H-ZSM-22; varying the feed rate had no effect on products yield at a given conversion. This observation is in line with the previous research by Teketel over H-ZSM-22 [77]. However, in case of H-Mordenite and due to its short lifetime during the MTH reaction less data points obtained and the picture was not so clear to conclude.

The data suggested that for H-ZSM-22 and H-ZSM-23 the deactivation due to coke formation is a non-selective process in which the yield at a given conversion was not dependant on the amount of coke deposited in the zeolite structure [13, 64, 91]. Thus, the changes in product selectivity over time on stream can be simply described as changing in contact time with gradual deactivation of catalyst with time, as previously suggested by Janssens [40].

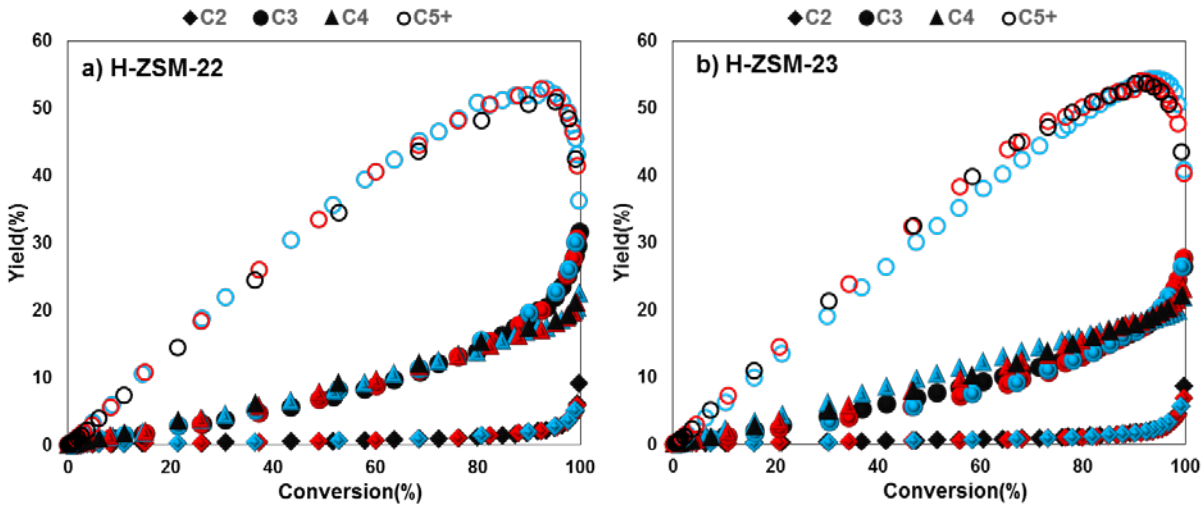

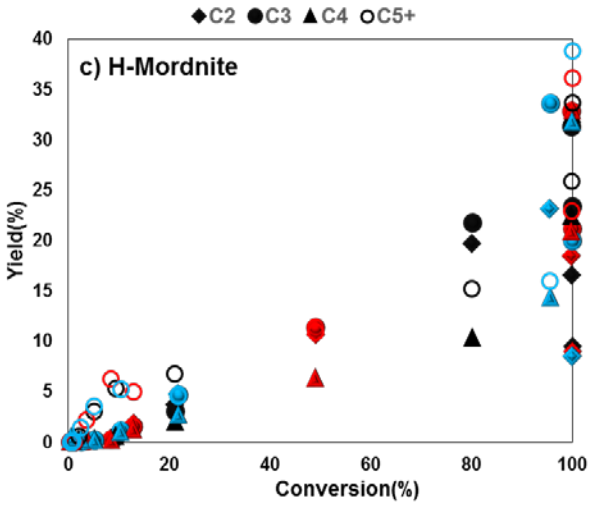

Figure 5.11: Product yield (C %) versus methanol conversion (%) during the MTH reaction over a) H-ZSM-22, b) H-ZSM-23 and c) H-Mordenite. Note that the corresponding WHSV for H-ZSM-22 and H-ZSM-23 were WHSV=1 (black), 1.5 (red) and 2 (blue) $gg_{cat}^{-1}h^{-1}$, while for H-Mordenite WHSV=2 (black), 3 (red) and 4 (blue) $gg_{cat}^{-1}h^{-1}$ were applied. The MTH reactions were performed at 400 °C and Pp_{MeOH} =13 kPa over all the catalysts.

5.4.2. Product Selectivities and Yields over 3D zeolites

5.4.2.1. Product selectivity

Product selectivities over 3D zeolites; H-IM-5, H-ITQ-13, H-Beta and H-ZSM-5 at 80% methanol conversion, 400 °C and Pp_{MeOH} = 13 kPa, are depicted in Fig. 5.12.

From Fig. 5.12, For H-IM-5 (3D 10-ring channel with cross-section area of 24.1 $Å^2$) the product distributions at 80% methanol conversion were as follows:

C_3(23%)>C_{6+} aliphatics(21%)> aromatics(14%)>C_5(12%)>C_{4-}(11%)>$C_{4=}$(9%)>C_2(5%)>C_1

The product selectivities over H-ITQ-13 (3D 9 and 10-ring channel with cross-section area of 20 $Å^2$) exhibited the highest selectivity for C_{6+} aliphatics (~ 30%), while the aromatic fraction showed a selectivity of 5%. The C_3 fraction showed a slightly lower selectivity (~ 27%) than C_{6+} aliphatics followed by a considerably lower selectivity for C_5 and buthene as 15%. Buthane and aromatics exhibited almost equal selectivity of 5% followed by C_2 (2%) and C_1 (1%). The selectivity of buthene, buthane and aromatics over H-IM-5 compared to those selectivities over H-ITQ-13 showed ratio of 0.5, 2 and 3, respectively. The higher Aromatic and buthane selectivity in IM-5 might be explained by higher conversion of C_{6+} aliphatics to aromatics and alkane via cyclisation/ aromatisation reactions and higher activity of arene

versus alkene cycle in more spacious channel structure of IM-5 (24.1 $Å^2$) respect to ITQ-13 (20 $Å^2$). During cyclisation/aromatisation reactions, alkene such as buthene are the source of hydride, thus the selectivity of this fractions became lower, as seen in IM-5 compared to ITQ-13. Therefore, the relatively selectivity of products in these 3D structures can be successfully explained by dual cycle model.

For Beta zeolite (3D 12-ring channel with cross-section of 34.7 $Å^2$), the order of product selectivities at 80% conversion were as follows:

aro(28%)>C_{4-}(16%)>C_3(15%)>C_{6+} ali(11%)>C_5(8%)>C_2(7%)>$C_{4=}$(5%)>C_1(3%)

Clearly, higher aromatic selectivity obtained over H-Beta with larger pore channels. High selectivity for aromatic and buthane can be an indication of higher arene-cycle activity and higher rate of aromatisation and hydride transfer reactions which reduced the alkene ($C_{4=}$) versus alkane (C_{4-}) selectivity. In the previous study done by Bleken et al. [45] over H-ZSM-5 with different acid site densities, the buthane/buthene and aromatics/aliphatics ratio correlated to the acid site density. The material with higher acid site density showed higher ratio of buthane/buthene and aromatics/aliphatics in line with the data obtained over the 7 studied structures (also see section 5.4). For H-Beta with the highest acid site densities among the other samples, the highest Buthane/buthene and aromatics/aliphatics ratio were obtained. By increasing the number of acid sites, the probability of secondary reactions also increases.

Finally, for H-ZSM-5 (3D 10-ring channel with cross-section of 23.3 $Å^2$) the product distributions were similar to H-IM-5. The trend of product selectivity was as follows: C_3 (27%) followed by C_{6+} aliphatics (20%), C_5 (13%), buthene (12%), aromatics (11%), buthane (8%), C_2 (4%) and C_1 (1%). Over this medium channel size structure, both alkene and arene-cycles worked parallel to a similar extent to produce both aromatic and higher aliphatic compounds.

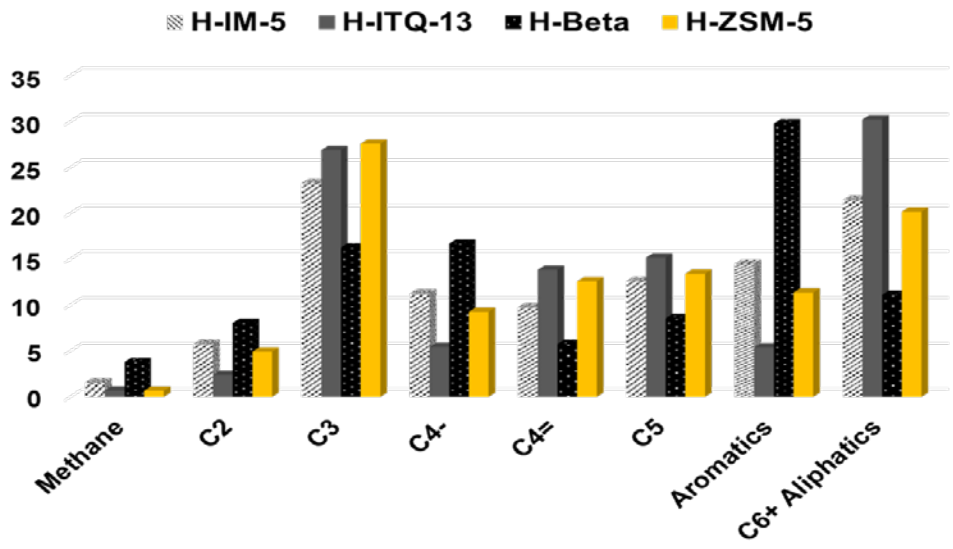

Figure 5.12: selectivity of different products at 80% methanol conversion, 400 °C with WHSV=2 $gg_{cat}^{-1}h^{-1}$ for H-IM-5, H-ITQ-13, H-Beta and with WHSV=10 $gg_{cat}^{-1}h^{-1}$ for H-ZSM-5.

5.4.2.2. Product Yield

Fig. 5.13 illustrates product yields over 3D zeolites; H-IM-5, H-ITQ-13, H-Beta with WHSV=2 $gg_{cat}^{-1}h^{-1}$ and H-ZSM-5 with WHSV=10 $gg_{cat}^{-1}h^{-1}$ at 400 °C and Pp_{MeOH} = 13 kPa.

For H-IM-5, the C_{6+} aliphatics and C_3 fractions were the most abundant products in the range of 0-75% methanol conversion with a slightly higher yield for C_{6+} aliphatics. At 80% methanol conversion the C_{6+} aliphatics showed a maximum yield (~ 20%), while with increasing conversion to 100% the yield declined to less than 5%. In the range of 80% to slightly less than 100% conversion, C_3 with a clear linear approach towards the origin showed the highest amount among all other products. At full methanol conversion, the highest yield for C_{6+} aromatics was detected. Although C_5 and aromatics coincided over the rage of 0-80% conversion, but C_5 showed a downward curvature while reaching to full methanol conversion. The C_{6+} aromatic fraction exhibited a sharp increase at higher conversion levels (>80%). For the C_4 alkane and alkene fractions, from 80% to 100% conversion C_4 alkane increased sharply (from 10% to 20%) while C_4 alkene yield decreased from 10% to less than 1% with increasing methanol conversion. The C_2 fraction with lower yield in the whole conversion range as compared to above products, showed a linear trend from 0 up to 80% conversion with an upwards curvature close to full methanol conversion.

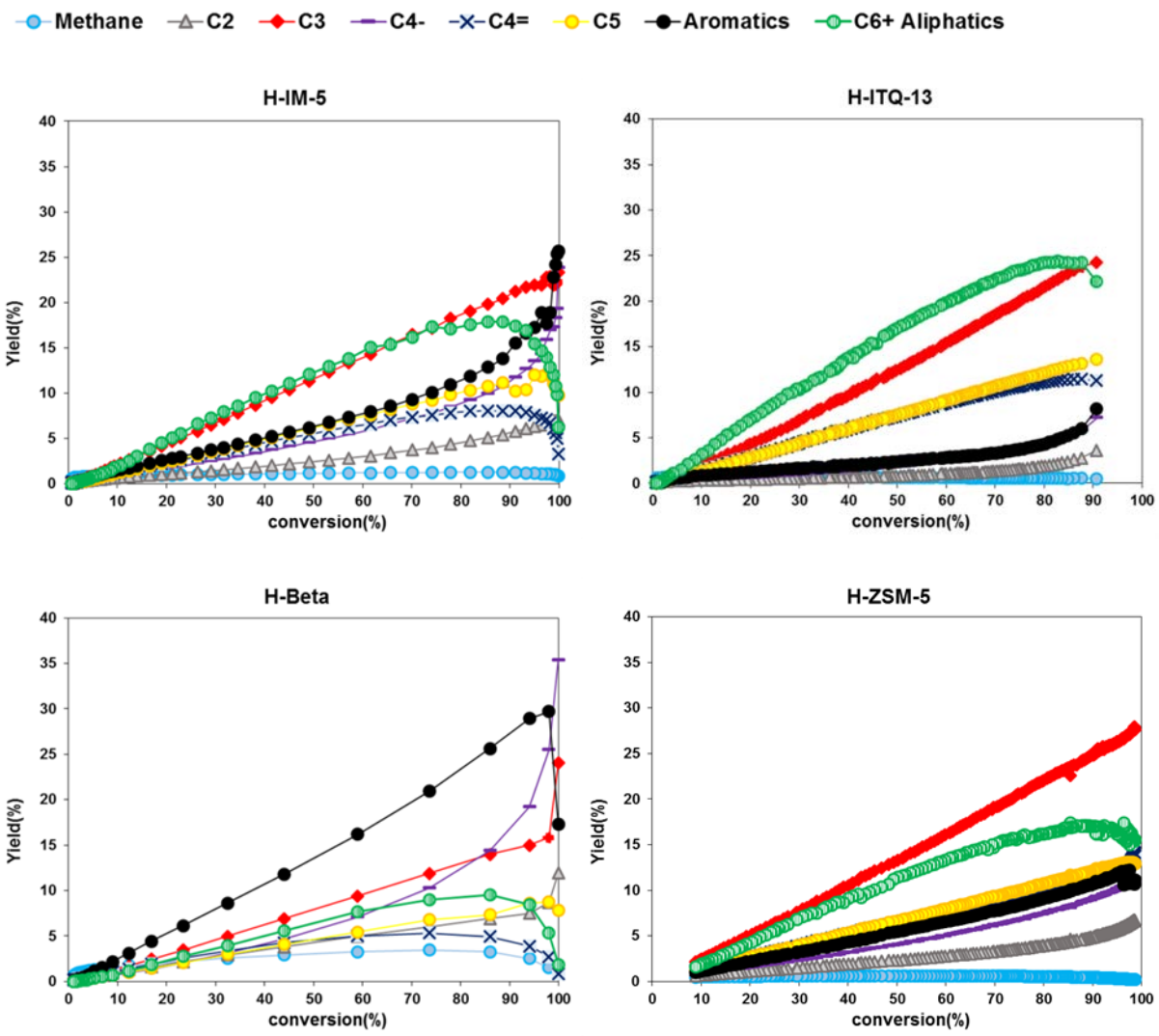

Figure 5.13: Products yield vs. methanol conversion over H-ITQ-13 (top left), H-IM-5 (top right), H-Beta (bottom left) and H-ZSM-5 (bottom right). The MTH reactions were performed at 400 °C and WHSV=2g $g_{cat}^{-1}h^{-1}$ for H-Beta, H-ITQ-13 and H-IM-5 and WHSV=10 g $g_{cat}^{-1}h^{-1}$ for H-ZSM-5.

As all of the products crossed the origin, all products can be considered as primary products rather than pure secondary products. However, the C_{6+} aromatics and C_4 alkane with upward curvature at higher methanol conversion (>80%) were both secondary and primary stable products. The downwards curvature of C_{6+} aliphatics, C_4 alkene and C_5 can be an indication of unstable products. The product distributions and their trend are in line with the reported values by Bleken et al. over H-IM-5 at 350 °C [76].

According to the dual-cycle model, the higher alkenes formed in alkene-based cycle can be further converted to aromatics compounds via cyclization and hydride transfer reactions. Along with these reactions, alkenes as a source of hydride converted to alkanes as well. Referring to these reactions the downwards curvature of C_{6+} aliphatics and buthene and

upwards curvature of C_{6+} aromatics and buthane can be explained well. At higher methanol conversion, larger fraction of higher alkenes converts to aromatic compounds which increases the yield of both aromatics and alkane e.g. buthane.

Fig. 5.13 (top right panel) shows the yield as a function of conversion for H-ITQ-13 at WHSV=2 $gg_{cat}^{-1}h^{-1}$. For this zeolite, the conversion initiated at ~ 90%, the right-most data points. As seen from the graph, the C_{6+} aliphatic fractions showed the highest yield with a maximum of 25% yield corresponding to 80% conversion which decreased to 20% yield at ~90% conversion. A clear linear trend with a slope slightly lower than C_{6+} aliphatices which crossed the origin can be found for the C_3 fraction. The C_4 alkene and C_5 coincided over a conversion range of 0-80% with a clearly lower slope than C_3 compounds. The C_4 alkene showed a downwards curvature at higher methanol conversion (80-90%). C_{6+} aromatics and C_4 alkane also coincided over the 0-80% methanol conversion with an upwards curvature at higher conversion levels (80-90%). Finally, the C_2 fraction exhibited a straight line with the lowest slope over the whole methanol conversion range. The yield of C_1 was too low over the whole conversion range.

The lack of data points at the higher methanol conversion range between 90% to full conversion make the comparisons rather difficult as mosts of secondary reactions take place in this conversion range. However, the downwards curvature of C_{6+} aliphatics and C_4 alkene and upwards curvature of aromatics and buthane can be explained well by using the dual cycle model and involved cyclisation and hydride transfer reactions, similar to IM-5 material.

Fig. 5.15 (bottom left) depicts the products yield versus conversion for H-Beta at WHSV=2 $gg_{cat}^{-1}h^{-1}$ and 400 °C. The C_{6+} aromatics showed the highest yield with a linear trend approached to origin and a maximum at 30% yield corresponds to 98% methanol conversion which then declined sharply to 17% yield at full methanol conversion. From the shape of the graph, it can be said that C_{6+} aromatics were a primary and secondary unstable product. In contrast, the C_3 fraction with a linear trend over 0 to 98% conversion range showed a sharp increase from 17% to 25% yield as the conversion approached to 100% methanol conversion indications of primary stable product. The C_4 alkane exhibited the similar but with gradual increase with increasing conversion which ended up to the highest yield of 35% at full methanol conversion; this fraction might be considered as primary and secondary stable product. C_{6+} aliphatics revealed a curve with a maximum of 10% yield at 85% conversion which declined to almost zero at full methanol conversion; the indication of secondary

unstable product. A similar trend with lower slope was found for C_4 alkene and methane with a maximum of 5% and 3% yield at 70% conversion respectively and zero yield at full methanol conversion; indication of primary and secondary unstable products for both. C_2 and C_5 which coincided over 0 up to 90% conversion showed a deviation at higher conversion levels. The C_2 showed a small upwards curvature while the slope of C_5 declined slightly as the conversion approached to 100%; showed secondary stable and unstable products respectively.

The increases and decreases in the C_3 and C_{6+} aliphatic yields close to 100% conversion might be connected to each other when more cracking of these higher alkenes to lighter hydrocarbons such as C_3 (C_{6+} alkenes $\rightarrow$ C_3) take place. The cyclisation/aromatisation reactions might result in the observed decline in slope of C_4 alkene and C_{6+} and the concave shape of C_4 alkane. Similar to H-Mordenite sample, the higher yield of C_1 might be an indication of the reactions which lead to coke formation.

The yield as a function of conversion for H-ZSM-5 is shown in Fig. 5.13 (bottom right panel) at WHSV=10 $gg_{cat}^{-1}h^{-1}$ and 400 °C. The most abundant product over the whole conversion range was C_3 with a clear linearly trend approaching the origin, indicates the primary stable product in agreement with previous studies performed over H-ZSM-5 by Bleken et al. [45, 76]. C_{6+} aliphatic with lower yield compared to C_3 showed a downwards curvature over the range of 90 to 100% conversion with a maximum of ~ 18% yield which corresponds to 90% conversion. The C_{6+} downwards curvature at high methanol conversion indicates the primary unstable product. The C_5, C_{6+} aromatics and alkene coincided over the whole conversion range; except for C_4 alkene a small increase in yield close to full methanol conversion was detected indicating a stable product. The C_4 alkane and the C_2 fractions exhibited almost straight lines, for C_2 a small increase over 90-100% conversions was observed, which shows a secondary stable product.

Cracking reactions of C_{6+} aliphatic to lighter alkene such as C_4 can be an explanation of the decrease and increase in C_{6+} aliphatic and C_4 alkene respectively in agreement with dual cycle model.

5.4.2.3. Coke and shape selectivity

Fig. 5.14 illustrates C_2, C_3, C_4 and C_{5+} yields as a function of methanol conversion at different space velocities over H-IM-5, H-ITQ-13, H-Beta and H-ZSM-5 at 400 °C and Pp_{MeOH}=13 kPa.

From Fig. 5.14 similar to the discussions made for 1D zeolites in section 5.1.3, at a given methanol conversion the product yield were independent of the amount of coke formed in the studied 3D topologies; H-IM-5, H-ITQ-13, H-Beta and H-Beta at 400 °C. Therefore, the deactivation during the MTH reaction over these studied catalysts is also non-selective process in which product selectivities are independent of deactivation in line with previous literatures [45, 76, 78]. The changes in product selectivity over time on stream can be interpreted as the changing in contact time as proposed by Janssens [40, 41] and the deactivation can be simply considered as loss of active sites in the reactor with time on stream.

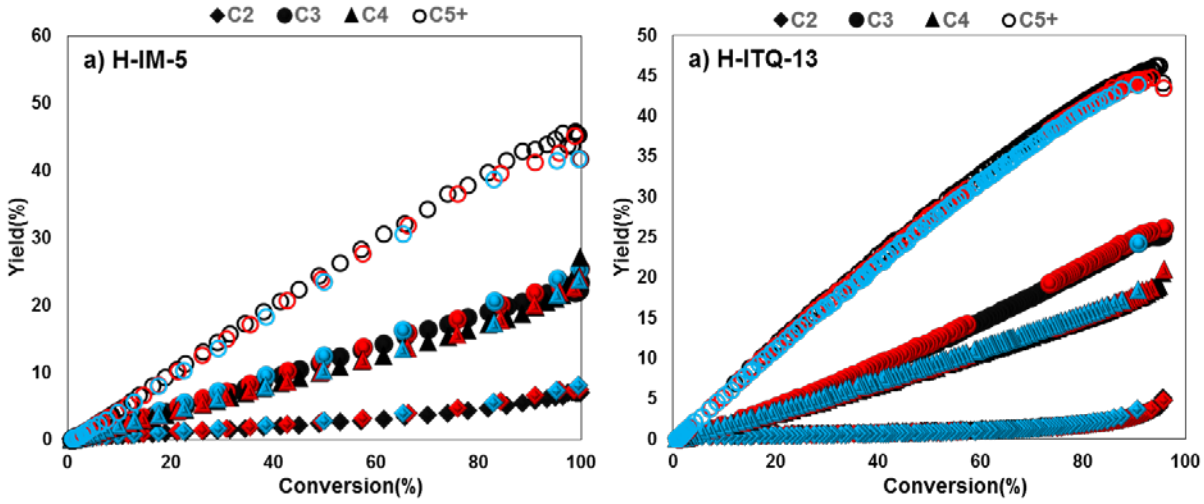

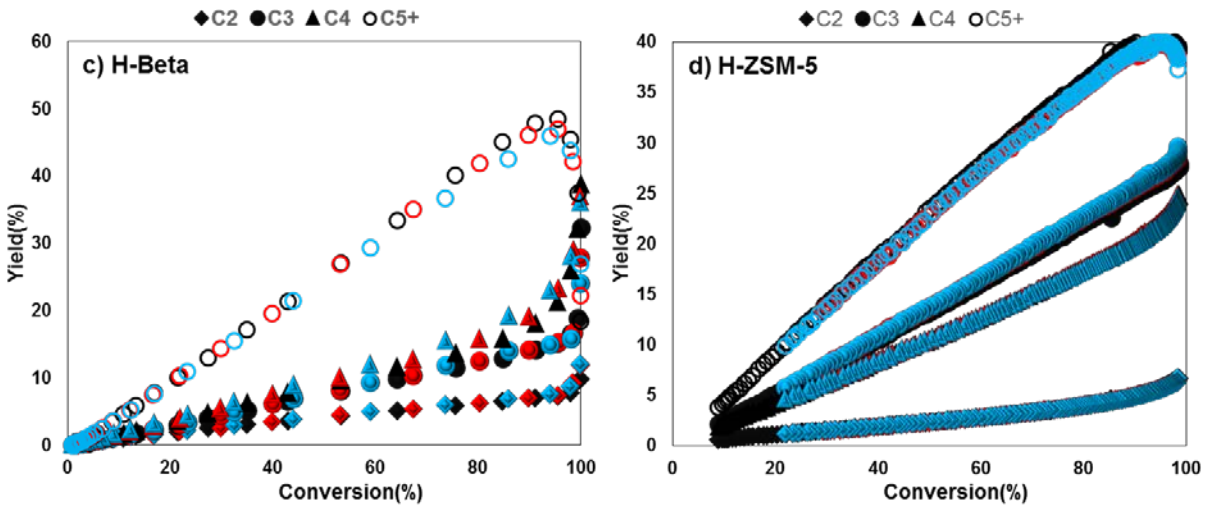

Figure 5.14: Yield (C %) versus methanol conversion (%) during the MTH reaction over a) H-IM-5, b) H-ITQ-13, c)H-Beta and d)H-ZSM-5. . Note that the corresponding WHSV for H-ITQ-13 and H-beta were WHSV=1 (black), 1.5 (red) and 2 (blue) g $g_{cat}^{-1}h^{-1}$, while for H-IM-5: WHSV=2 (black), 4 (red) and 8 (blue) $gg_{cat}^{-1}h^{-1}$ and in case of H-ZSM-5: WHSV=10 (black), 12 (red) and 14 (blue) $gg_{cat}^{-1}h^{-1}$. The MTH reactions were performed at 400 °C and Pp_{MeOH} =13 kPa.

5.5. Shape selectivity of the studied catalysts

In order to compare data obtained during the MTH reaction over the various studied structures, yield of C_2, C_3, C_{5+} aliphatic and aromatic compounds over H-ZSM-22, H-ZSM-23, H-Mordenite, H-IM-5, H-ITQ-13, H-Beta and H-ZSM-5 are plotted as a function of methanol conversion in Figs. 5.15 and 5.16. It is worth noting that in the below graphs the space velocity was 2 $gg_{cat}^{-1}h^{-1}$ for all materials except for H-ZSM-5 a space velocity of 10 $gg_{cat}^{-1}h^{-1}$ was applied.

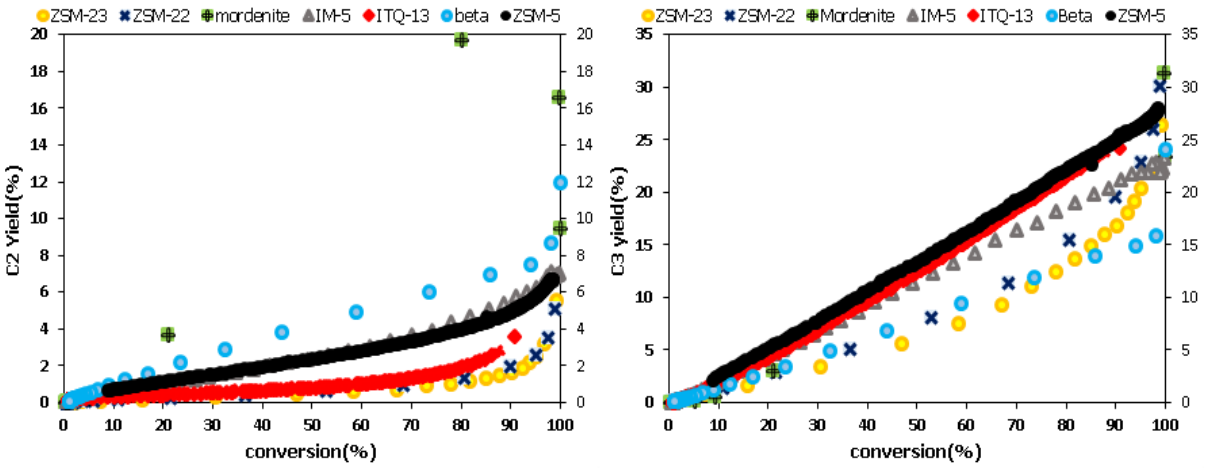

Figure 5.15: C2 (left panel) and the C3 (right panel) yield as a function of conversion for different zeolites tested at 400 ℃ and Pp_{MeOH} =13kPa

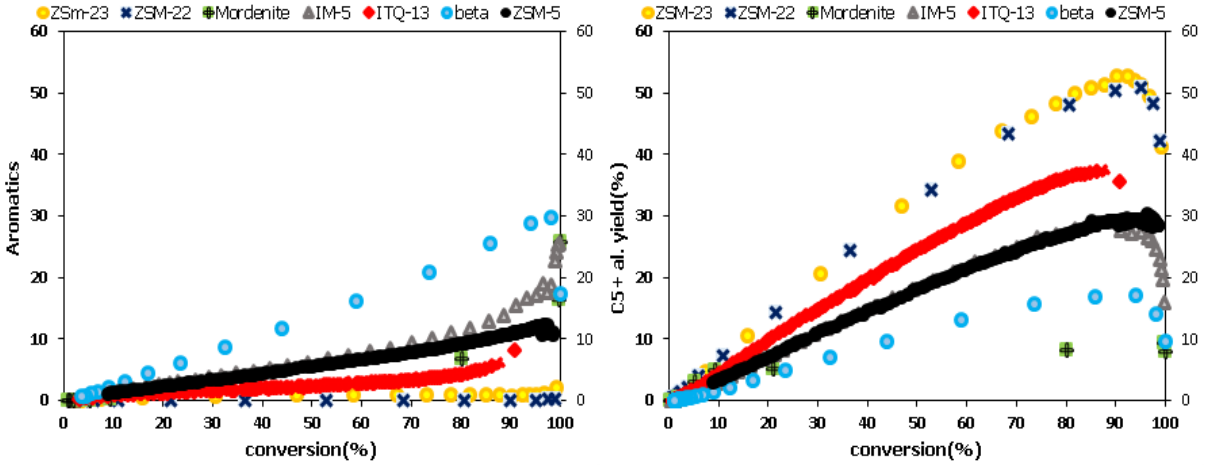

Figure 5.16: aromatic (left panel) C5+ aliphatic (right panel) and yield as a function of conversion for different zeolites tested at 400 ℃ and Pp_{MeOH} =13kPa.

As seen from C_2 yield in Fig. 5.15 (left panel), the highest C_2 value was obtained over Mordenite (1D 12-ring) followed by Beta zeolite (3D 12-ring). The C_2 yield decreased further over H-IM-5, H-ZSM-5 and H-ITQ-13 (3D 10-ring), and then to even lower values over H-ZSM-23 and H-ZSM-22 (1D 10-ring) at the tested conditions. The production of ethene via alkene-cycle is considered to be negligible according to the dual cycle mechanism of the MTH reaction [8, 93]. It is expected over more spacious channels zeolites such as Beta and Mordenite, the arene-cycle become more active than the alkene-cycle which might lead to more C_2 yield and more aromatic yield in line with data obtained (see Fig. 5.16 left panel). Thus, C_2 and aromatics yields decreased as with replacing the catalyst by the material with

smaller channel size intersections following the order of: 3D 12-ring (Beta) > 3D 10-ring (IM-5, ZSM-5, ITQ-13) > 1D 10-ring (ZSM-22 and ZSM-23), Mordenite was an exception.

Looking at the C_3 yield in Fig. 5.15 (right panel), it changed with the zeolite topology over a range of 0-80% methanol conversion as follows:

ZSM-5 = ITQ-13 > IM-5 >> ZSM-22 = Beta > Mordenite > ZSM-23.

Thus, the structure can be grouped into two sets with similar C_3 yields; 3D 10-ring (ZSM-5, ITQ-13 and IM-5) and 1D/3D 10/12-ring (ZSM-22, Beta, Mordenite and ZSM-23) over the mentioned range of methanol conversion and the results are in good agreement with a recent work reported by Teketel et al [8] tested at 350 °C. The upwards curvature of C_3 over H-ZSM-22 and H-ZSM-23 might be originated from alkene methylation and interconversions (e.g. $C_6 \rightarrow 3C_3$) especially when combined with the simultaneous downwards curve of C_{5+} aliphatic compounds, see Fig. 5.16 bottom-right panel.

The C_{5+} aliphatic yields in Fig. 5.16 right panel revealed that the 1D 10-ring materials such as ZSM-22 and ZSM-23 with the smallest pore channels exhibited the highest amount of C_{5+} aliphatic compounds in the gas effluent over the whole range of methanol conversion. The second stage with a noticeable decline was belonged to 3D 10-ring ITQ-13, followed by IM-5 and ZSM-5 which showed a sharp decline in yield compared to ITQ-13. Finally two structures with 12-ring, Beta and Mordenite, showed the lowest C_{5+} values in agreement with the trend previously reported at 350 °C [8]. These observations are in good agreement with the dual cycle model considering higher activity for alkene-cycle versus arene-cycle which results in higher yield of aliphatics compounds and lower aromatic yields in H-ZSM-22 and H-ZSM-23 with 1D 10-ring channels with more restricted space inside the structures respect to other structures and the reverse scenario for H-Beta 3D 12-ring which relatively more channel space for arene-cycle activity leads to more C_2 and aromatic yield. The H-IM-5 and ZSM-5 with relatively larger channel cross-section areas of respectively 24.1 and 23.3 $Å^2$ than ITQ-13 (20 $Å^2$) appeared with higher aromatics, C_2 and lower C_{5+} aliphatics yield as compared to ITQ-13. In other words, in IM-5 and ZSM-5 the channels provided more space results in more activity of arene-cycle compared to ITQ-13.

5.6. Acid site density and selectivity

The ratio of buthane/buthene and C_{6+} aromatic/C_{6+} aliphatic yield as a function of acid sites density are illustrates in Fig. 5.17. Both ratio were increased by changing catalyst with higher acid site density. With higher acid site density, the activity of arene-cycle versus alkene-cycle in the dual cycle model increases which then increase the degree of secondary reactions. These observations are in line with the previous work done by Bleken et al. [45] while testing ZSM-5 with different acid site densities during the MTH reaction.

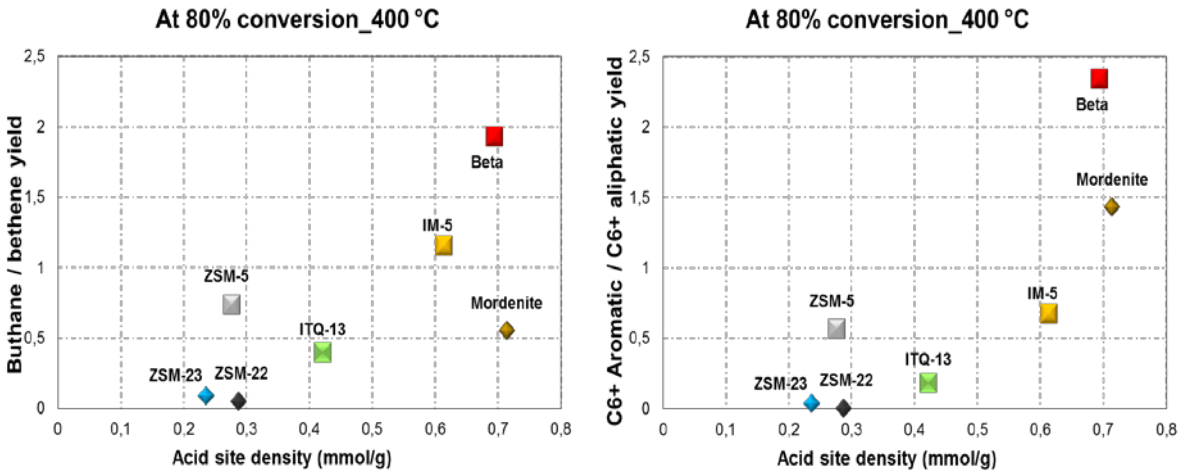

Figure 5.17: The product yield ratio of buthane/buthene (left panel) and C_{6+} aromatics/C_{6+} aliphatic (right panel) as a function of acid site density for 7 different zeolites at 400 °C and Pp_{MeOH} =13kPa.

In total, the pore size and acid site densities are the two most important factors influencing the activity of the alkene and arene cycles according to dual cycle model of the MTH mechanism which then leads to different product distributions influencing the transition-state or product shape selectivity.

5.7. Analyses of the retained materials

In order to investigate more the catalysts deactivations during the MTH reaction, the spent catalysts were characterized with respect to their surface areas and coke contents. In the next two parts, the characterisation results are presented together with their discussion.

5.7.1. Surface area measurement

The BET surface areas of the fresh and spent zeolites are shown in Table 5.1 for H-ZSM-22, H-ZSM-23 and H-Mordenite (1D zeolites) and in Table 5.2 for H-ITQ-13, H-IM-5, H-Beta and H-ZSM-5 (3D zeolites). A direct comparison between the isotherms obtained for the fresh and its spent versions is presented all the last part of this section in Figs. 5.18-24. For simplicity, only one isotherm of the spent zeolite is shown in each case. The isotherms in Figs. 5.18-23 relates to the totally deactivated H-ZSM-22, H-ZSM-23, H-Mordenite, H-IM-5, H-ITQ-13, and H-Beta during the MTH reaction with WHSV = 2 $gg_{cat}^{-1}h^{-1}$, while Fig. 5.24 belongs to the partially deactivated ZSM-5 sample tested with WHSV=10 $gg_{cat}^{-1}h^{-1}$.

The common feature of these isotherms is a significant decrease in amount of the adsorbed gas in micropores over the spent zeolite compared to the fresh catalyst (Figs. 5.18-24). Thus, for better comparison the value of the BET specific surface area (in m^2/g) and total pore volume (in cm^3/g) were calculated for both the fresh and spent samples and reported in Table 5.1 and Table 5.2. In addition, the accessible surface area and pore volume (in %) of the spent zeolites are also noted. As the kinetic diameter of N_2 (3.64 Å) and methanol (3.6 Å) are so close to each other, a good approximation on accessibility of reactant (methanol) to surface area/pore volume of the totally/partially deactivated zeolite can be achieved via N_2 adsorption.

From Table 5.1, the BET surface area for the fresh H-ZSM-22, 217 m^2/g, decreased significantly to 21-27 m^2/g as the catalyst became totally deactivated after MTH reaction. Also the total pore volume for this sample decreased from 0.137 to 0.07-0.09 cm^3/g (depending on WHSV), which is also noticeable. To compare those values of the fresh and spent catalyst clearly, the percentage value of accessible surface area and pore volume were also calculated and shown in the Tables. The accessible surface area reduced to almost 10%, while half of the total pore volume is still accessible by N_2 molecules for the completely deactivated ZSM-22 sample.

Table 5.1: Calculated values from surface area measurement of the fresh and spent 1D zeolites of H-ZSM-22, H-ZSM-23and H-Mordenite. By spent catalyst means the coked and totally deactivated sample after the MTH reaction.

Samples		**H-ZSM-22**			**H-ZSM-23**			**H-Mordenite**		
fresh catalyst	**BET (m^2/g)**	217			159			576		
	Total pore volume (cm^3/g)	0.137			0.658			0.399		
WHSV(g $g_{cat}^{-1}h^{-1}$)		**1**	**1.5**	**2**	**1**	**1.5**	**2**	**2**	**3**	**4**
spent catalyst	**BET (m^2/g)**	21	27	24	52	60	59	29	26	23
	Total pore volume (cm^3/g)	0.07	0.09	0.07	0.31	0.58	0.54	0.07	0.06	0.07
	Accessible surface area (%)	10	13	11	33	38	37	5	5	4
	Accessible pore volume (%)	51	66	51	47	88	82	18	15	18

Table 5.2: Calculated values from surface area measurement of the fresh and spent 3D zeolites of H-ITQ-13, H-IM-5, H-Beta and H-ZSM-5. By spent catalyst means the coked and totally deactivated sample after the MTH reaction (except for ZSM-5 which partially deactivated.

Samples		**H-ITQ-13**			**H-IM-5**			**H-Beta**			**H-ZSM-5**		
fresh catalyst	**BET (m^2/g)**	461			482			713			422		
	Total pore volume (cm^3/g)	0.385			0.812			1.12			0.606		
WHSV(g $g_{cat}^{-1}h^{-1}$)		**1**	**1.5**	**2**	**2**	**4**	**8**	**1**	**1.5**	**2**	**10**	**12**	**14**
spent catalyst	**BET (m^2/g)**	255	242	253	66	80	86	137	147	148	284	292	307
	Total pore volume (cm^3/g)	0.30	0.30	0.29	0.45	0.43	0.45	0.51	0.52	0.51	0.44	0.46	0.50
	Accessible surface area (%)	55	53	55	14	17	18	19	21	21	67	69	73
	Accessible pore volume (%)	78	78	75	55	53	55	45	46	45	72	76	82

In case of H-ZSM-23, the specific surface area also reduced significantly from 159 m^2/g for the fresh catalyst to 59-60 (depending on WHSV) for the totally deactivated zeolite. A decrease in total pore volume from 0.658 to 0.31, 0.58 and 0.54 cm^3/g with space velocities of 1, 1.5 and 2 was seen for H-ZSM-23. Hence, about 35% of the surface area is still available even after full deactivation of H-ZSM-23, while around 50% of pore volume is available in the deactivated sample with WHSV=1. This value increased to ~85% with WHSV=1.5 or 2 $gg_{cat}^{-1}h^{-1}$.

H-Mordenite showed a drastic decline in total surface area; declining from 576 to 23-29 m^2/g. So that only 5% of the surface was accessible after deactivation, while 18% of the pore volumes were available after full catalyst deactivation.

Table 5.2 shows the surface properties for 3D zeolites: H-ITQ-13, H-IM-5, H-Beta and H-ZSM-5. The surface area of fresh H-ITQ-13 (461 m^2/g) reduced to almost the half for the deactivated sample (250 m^2/g), while changing the WHSV did not change the surface blockage. For H-IM-5 and H-Beta zeolites, after the MTH reaction around 20% of the total surface area was still accessible by N_2 gas molecules and the surface areas decreased over H-IM-5 from 482 to ~ 80 m^2/g and from 713 to ~140 m^2/g over H-Beta after the MTH reaction. For H-ZSM-5, as the MTH reaction was stopped during the MTH reaction, it is not so surprising to have surface accessibility of 70% when testing the spent sample.

In all above samples, it seems that varying the feed rate (various WHSVs) over the tested zeolites have no effect on neither amount of the total accessible surface area nor the pore volume of the spent catalysts (Table 5.1-2). In H-Mordenite (1D, 12-ring) and H-ZSM-22 (1D, 10-ring) samples more than 90% of the total surface areas were occupied by coke species, while for H-IM-5 (3D, 10-ring) and H-Beta (3D, 12-ring) zeolites coke blocked almost 80% of the total surface areas. The blockage of surface areas decreased to ~65% for H-ZSM-23 with lowest initial total surface area of 159 m^2/g, and ~50% in case of H-ITQ-13. From only those values, a logical trend could not be easily found. But it might be noted that the surface blockage (in %) is rather higher in 1Ds than 3Ds which is reasonable as 1D channels may block easily with bulky molecules [22]. A rather high accessible surface of completely deactivated H-ITQ-13 of ~50 %, may be understood by recalling its channels connectivity (see section 1.3). In this zeolite, 9-ring and 10-ring channels connected to each other to form a 3D channels structure. The 9-ring channels can be block easier than 10-ring, as a more limited space provided with 9-ring.

The pore/channel blockage with coke precursors might be a reason for the deactivation of samples with rather lower accessible surface area after deactivation, but for instance in H-ITQ-13 and H-ZSM-23 with higher accessible surface areas even after full deactivation, the pore/channels blockage would not be the only reason for deactivation. It would be concluded that both poison/blockage of active sites and pore/channel blockage with coke precursors, were responsible for deactivation of those zeolites.

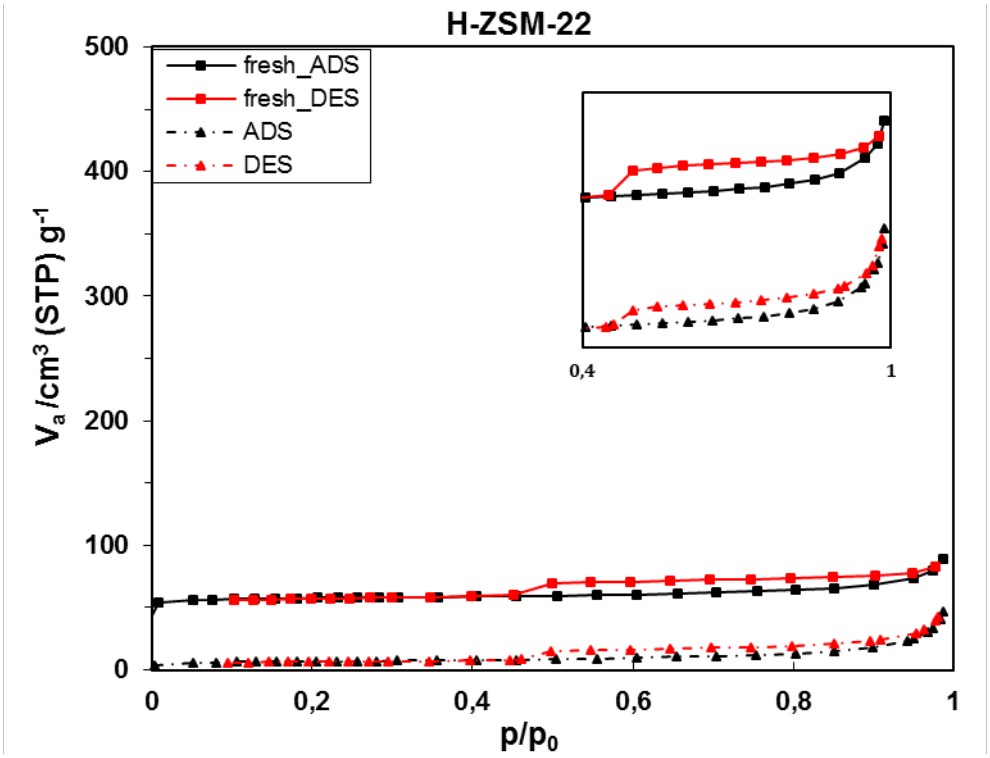

Figure 5.18: N_2 adsorption-desorption isotherm for the fresh (top curve) and totally deactivated H-ZSM-22 zeolite after MTH reaction at 400 °C, Pp_{MeOH}=13kPa and WHSV=2 $gg_{cat}^{-1}h^{-1}$ (bottom curve). The insert picture shows the hysteresis region clearly for both tested H-ZSM-22 samples.

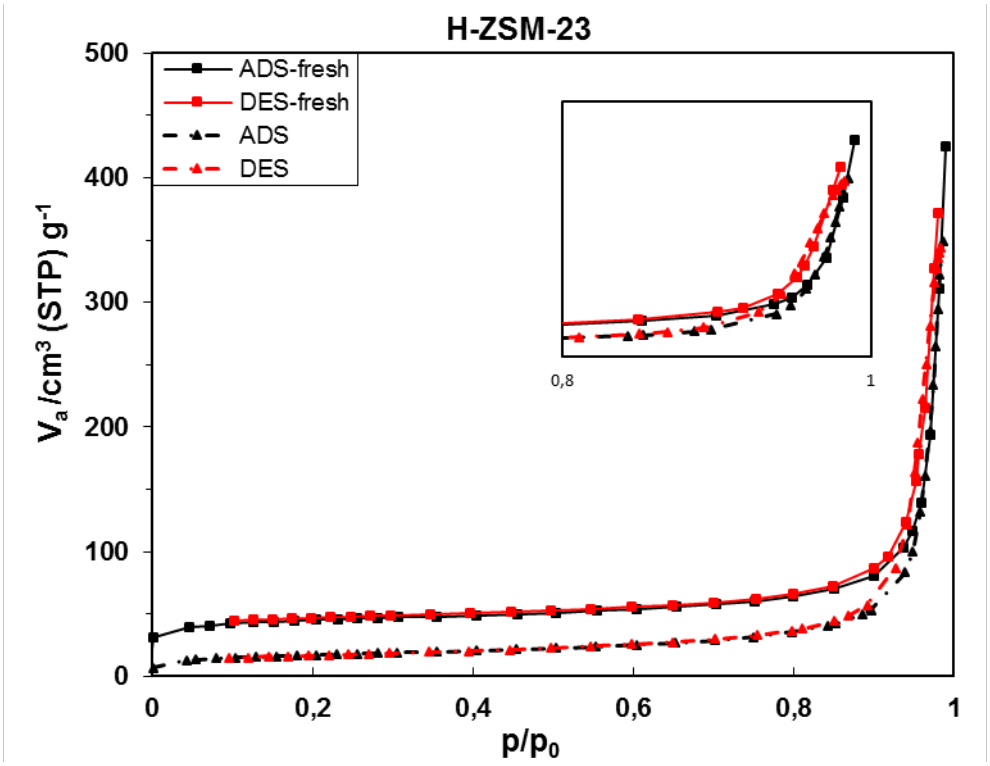

Figure 5.19:N_2 adsorption-desorption isotherm for the fresh (top curve) and totally deactivated H-ZSM-23 zeolite after MTH reaction at T=400 °C, Pp_{MeOH}=13kPa and WHSV=2 $gg_{cat}^{-1}h^{-1}$ (bottom curve). The insert picture shows the hysteresis region clearly for both tested H-ZSM-23 samples.

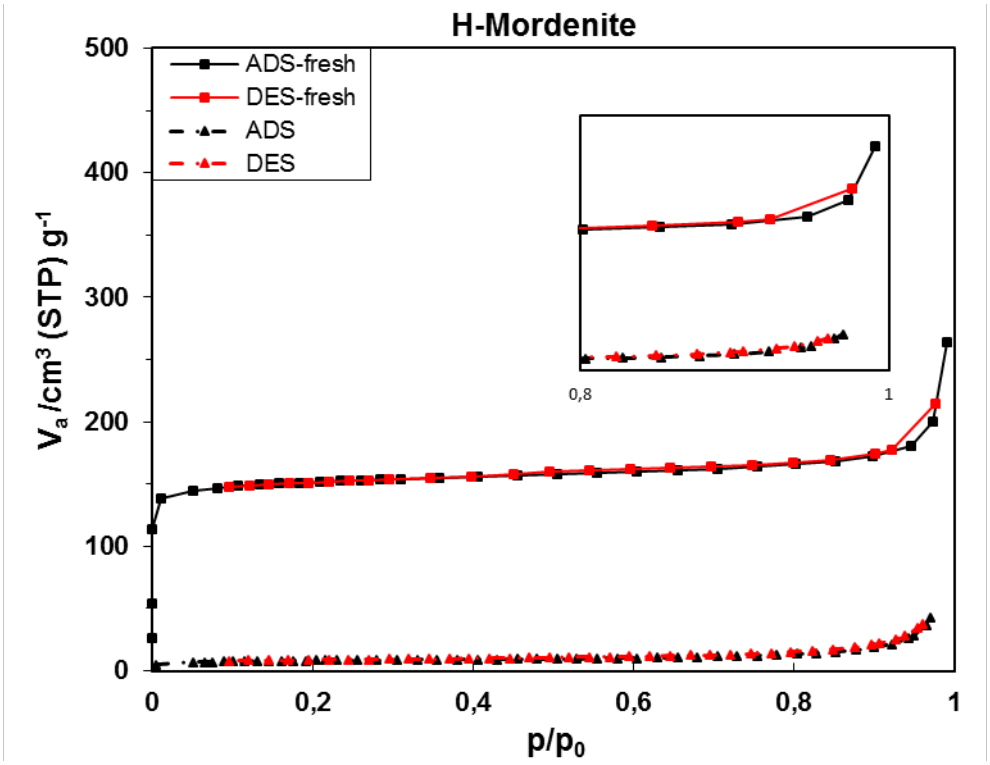

Figure 5.20: N_2 adsorption-desorption isotherm for the fresh (top curve) and totally deactivated H-Mordenite zeolite after MTH reaction at T=400 °C, Pp_{MeOH}=13kPa and WHSV=2 $gg_{cat}^{-1}h^{-1}$ (bottom curve). The insert picture shows the hysteresis region clearly for both tested H-Mordenite samples.

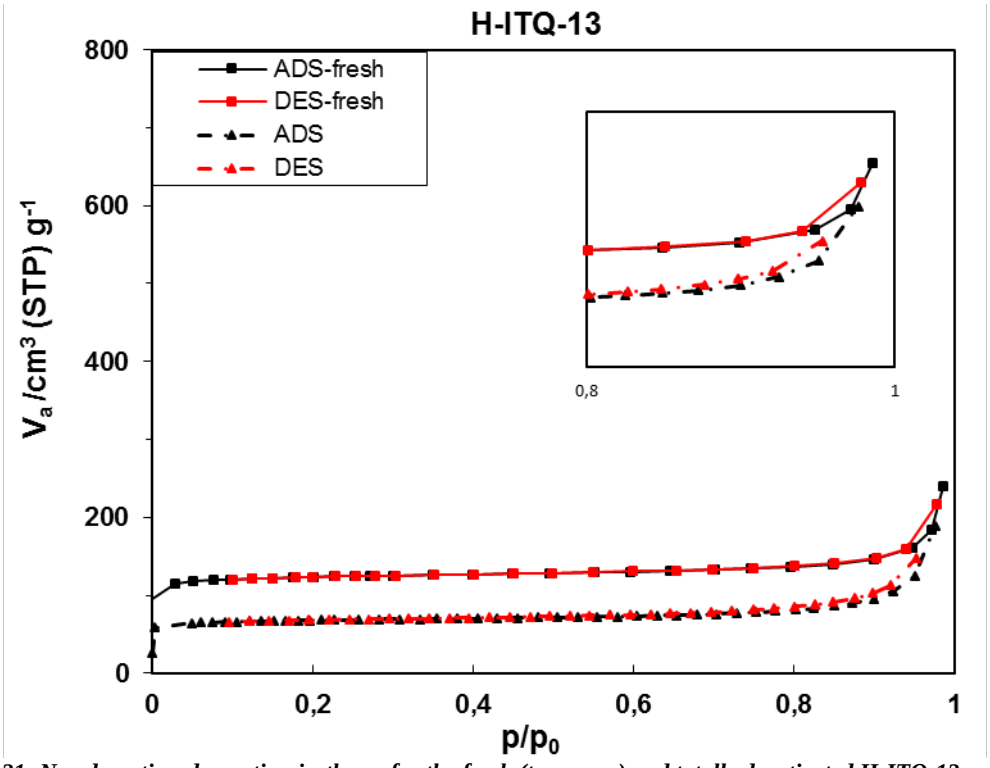

Figure 5.21: N_2 adsorption-desorption isotherm for the fresh (top curve) and totally deactivated H-ITQ-13 zeolite after MTH reaction at T=400 °C, Pp_{MeOH}=13kPa and WHSV=2 $gg_{cat}^{-1}h^{-1}$ (bottom curve). The insert picture shows the hysteresis region clearly for both tested H-ITQ-13 samples.

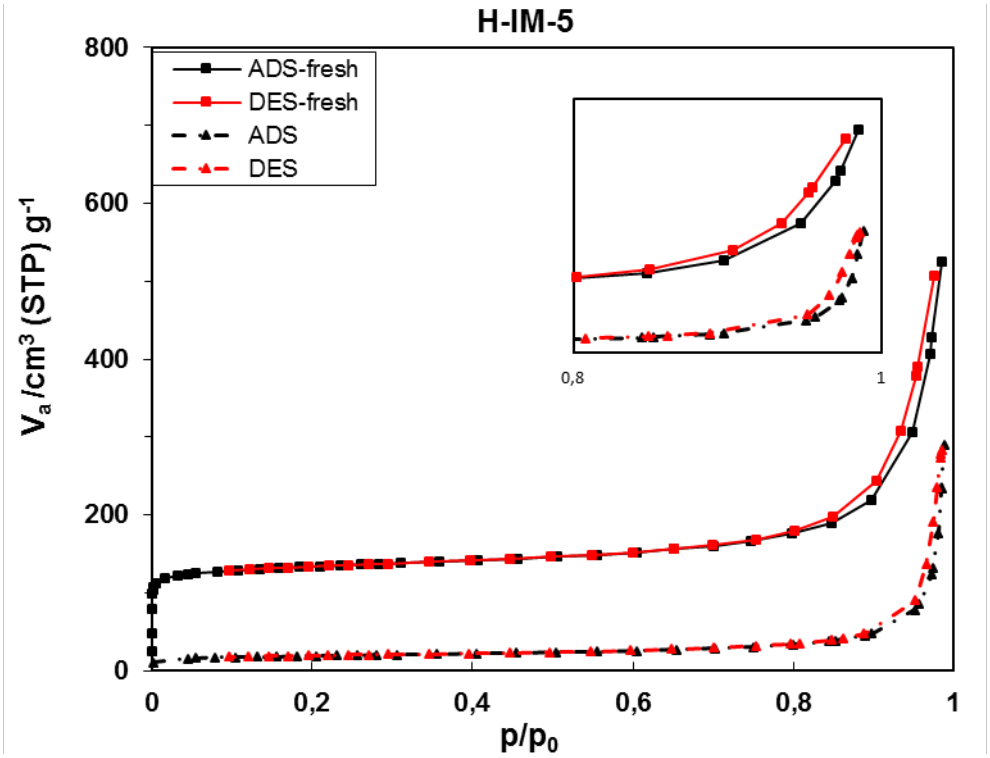

Figure 5.22: N_2 adsorption-desorption isotherm for the fresh (top curve) and totally deactivated H-IM-5 zeolite after MTH reaction at T=400 °C, Pp_{MeOH}=13kPa and WHSV=2 $gg_{cat}^{-1}h^{-1}$ (bottom curve). The insert picture shows the hysteresis region clearly for both tested H-IM-5 samples.

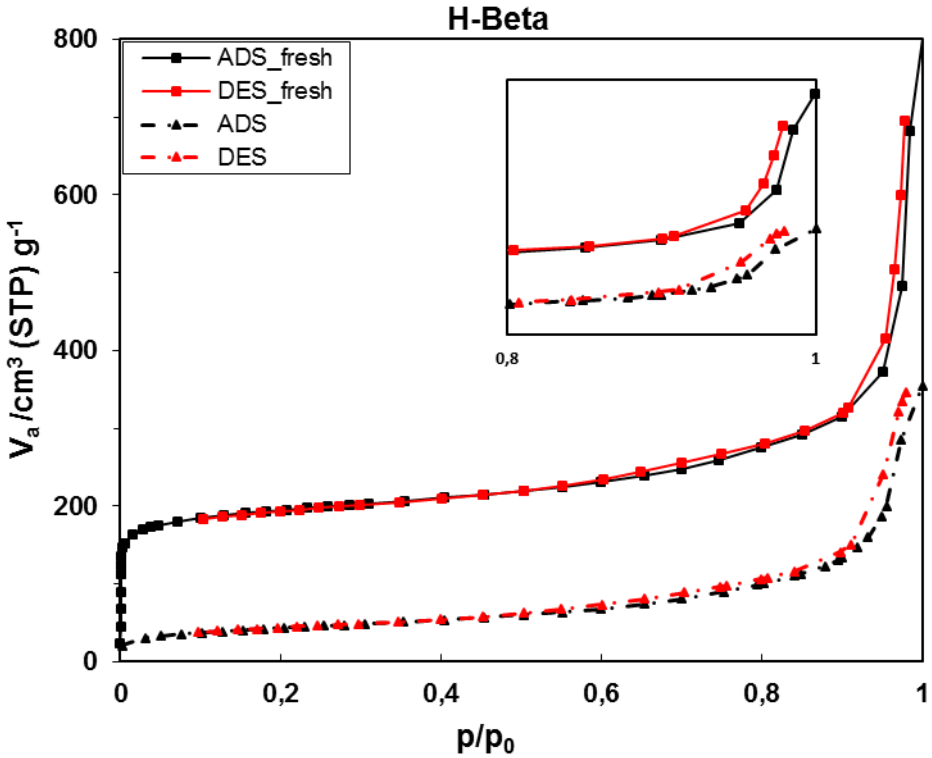

Figure 5.23: N_2 adsorption-desorption isotherm for the fresh (top curve) and totally deactivated H-Beta zeolite after MTH reaction at T=400 °C, Pp_{MeOH}=13kPa and WHSV=2 $gg_{cat}^{-1}h^{-1}$ (bottom curve). The insert picture shows the hysteresis region clearly for both tested H-Beta samples.

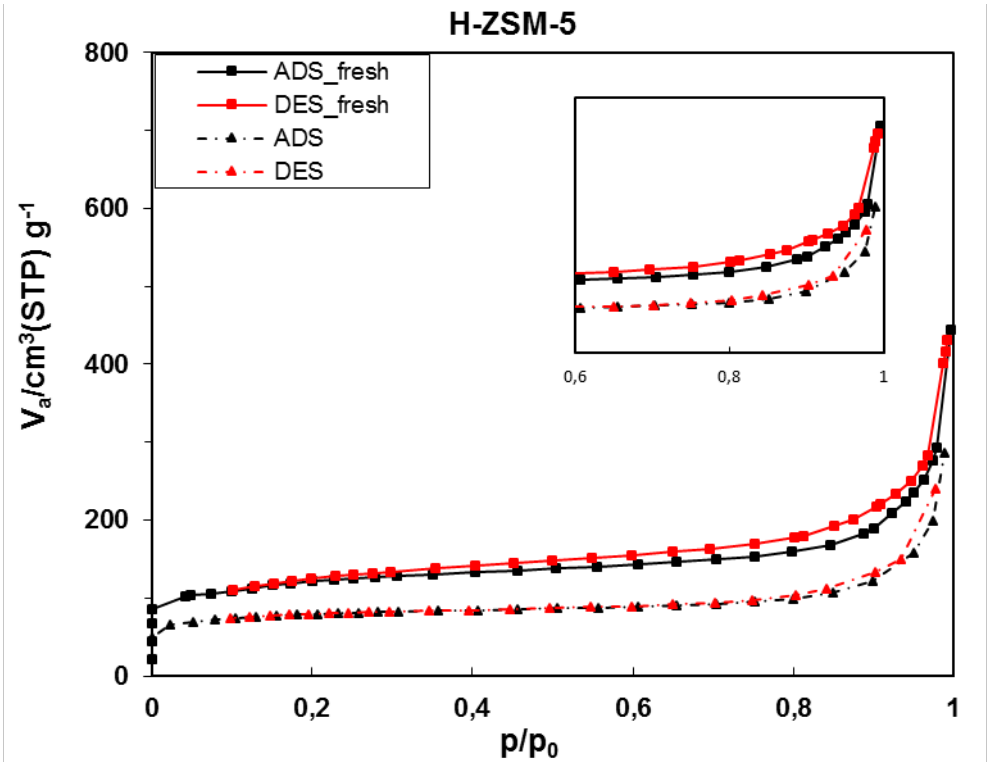

Figure 5.24: ***N_2 adsorption-desorption isotherm for the fresh (top curve) and partly deactivated H-ZSM-5 zeolite after MTH reaction at T=400 °C, Pp_{MeOH}=13kPa and WHSV=10 $gg_{cat}^{-1}h^{-1}$ (bottom curve). The insert picture shows the hysteresis region clearly for both H-ZSM-5 samples.***

5.7.2. Coke content

The total coke deposited inside the catalyst was calculated by only considering the weight loss of the second stage (temperature range between 200-600 °C) in the TGA analysis as follows (see Fig. 3.11):

$$\text{Total coke content (\%)} = \frac{(sample\ weight)_{at\ 200°C} - (sample\ weight)_{end\ of\ TGA}}{(sample\ weight)_{at\ 200°C}} \times 100$$

Accordingly, the coke amounts for the spent catalysts are reported in Table 5.3 and 5.4 for 1D zeolites: H-ZSM-22, H-ZSM-23 and H-Mordenite and 3D zeolites: H-ITQ-13, H-IM-5, H-Beta and H-ZSM-5, respectively. In addition, TGA graphs of all 7 zeolites are presented in Appendix 6.

As it can be seen from Table 5.3, H-ZSM-22 contained ~ 4 % coke after full deactivation. Only a small variation in coke content was observed with changing space velocity. The coke content of H-ZSM-23 was in the range of 3.53-3.8 % with different WHSVs, which is comparable to H-ZSM-22. The samples tested with WHSVs of 1, 1.5, and 2 $gg_{cat}^{-1}h^{-1}$, showed 3.8, 3.9 and 3.53 percent coke. In contrast to the previous samples, H-Mordenite showed much higher coke amount as ~16%. In Mordenite sample, 15.7, 15.8 and 16.1 percent coke was found over Mordenite after the MTH reaction with space velocity of 2, 3 and 4 $gg_{cat}^{-1}h^{-1}$ respectively.

Table 5.3: The total amount of coke for ZSM-22, ZSM-23 and Mordenite zeolites with different WHSVs at 400 °C and Pp_{MeOH} =13kPa

Samples	**H-ZSM-22**			**H-ZSM-23**			**H-Mordenite**		
WHSV($gg_{cat}^{-1}h^{-1}$)	**1**	**1.5**	**2**	**1**	**1.5**	**2**	**2**	**3**	**4**
TOTAL AMOUNT OF COKE (WEIGHT%)	4.6	3.4	3.9	3.8	3.9	3.53	15.7	15.8	16.1

Table 5.4: The total amount of coke of ITQ-13, IM-5, and Beta zeolites with different WHSV, 400 °C and Pp_{MeOH} =13kPa

Samples	**H-ITQ-13**			**H-IM-5**			**H-Beta**			**H-ZSM-5**		
WHSV($gg_{cat}^{-1}h^{-1}$)	**1**	**1.5**	**2**	**2**	**4**	**8**	**1**	**1.5**	**2**	**10**	**12**	**14**
TOTAL AMOUNT OF COKE (WEIGHT%)	6.1	6.0	7.3	10	9.4	9.1	18.4	18.2	18.3	9.6	-	-

Turning to 3D samples, H- ITQ-13 contained ~ 6 % coke with both space velocities of 1 and 1.5 $gg_{cat}^{-1}h^{-1}$. The deposited coke increased to 7.3 % with space velocity of 2 $gg_{cat}^{-1}h^{-1}$. In contrast, H-IM-5 showed a higher coke content (10 %) with lower WHSV=2 $gg_{cat}^{-1}h^{-1}$ compared to its coke values at WHSV= 4 and 8 $gg_{cat}^{-1}h^{-1}$, which were 9.4 and 9.1 % respectively. H-Beta exhibited the highest coke content of ~ 18 %, which was similar over the tested range of space velocity. H-ZSM-5 with a coke content of ~ 10 % tested in the MTH reaction with space velocity of 10 $gg_{cat}^{-1}h^{-1}$ corresponds to the coke deposited up to 20% conversion. The coke value for this catalyst should then be carefully compared to other values which were corresponds to the totally deactivated catalyst.

In total, changing WHSVs or methanol rate did not significantly affect the total deposited coke for the studied zeolites. The relatively higher amounts of coke were obtained over 12-ring zeolites, H-Mordenite and H-Beta, which might suggests different deactivation mechanism of these zeolites.

5.7.3. Pore structure and coke content

The size and shape of cavities/cages and channels intersections (apertures) play an important role in coke formation and deactivation of zeolites. It has been known that most of reactions take place inside the restricted space of zeolites' pores/intersections and coke precursors are mainly formed inside the channels [31, 113]. Therefore it might be interesting to investigate a probable relationship between the coke content and the intersection/channel size of the studied zeolites.

The relation between coke content and cross-section area of the largest channels, which calculated by assuming the perfect elliptical channel shape, is illustrated in Fig. 5.25. A linear relationship between the total coke content and channel size can be obtained for ZSM-22, ZSM-23, Mordenite, ITQ-13, IM-5 and Beta zeolites. Therefore, the zeolites with a larger cross-section area of channels, Beta (34.7 $Å^2$) and Mordenite (35.7 $Å^2$), provide more space for molecules to react where either bulkier final products or non-desorbed by-product/coke precursors might be formed. Previously, the high resistance of ZSM-5 structure to coke formation was assigned to its especial pore structure which surpasses formation of bulkier components that might lead to coke precursors [113].

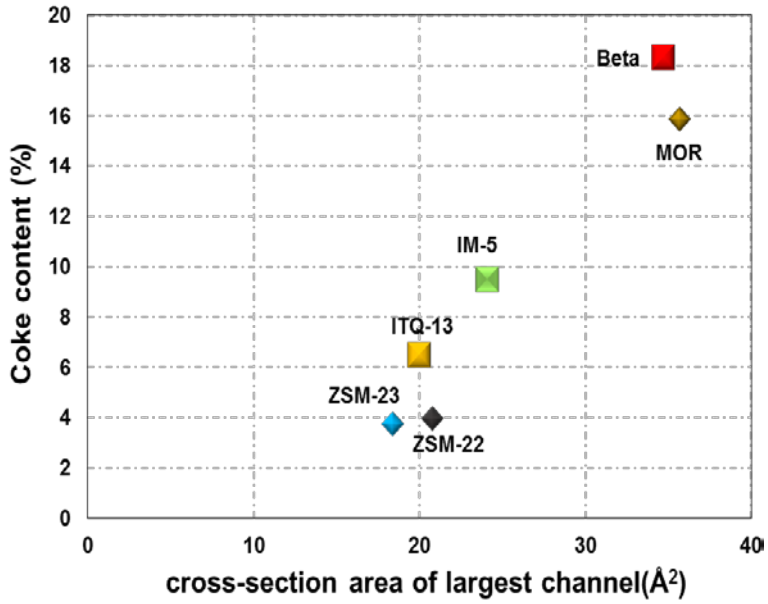

Figure 5.25: coke content versus largest channel size for ZSM-22, ZSM-23, ITQ-13, IM-5, Mordenite and Beta zeolites.

Skistad et al. [79] studied coke formation during the MTH reaction over IM-5, TNU-9 and ZSM-5 with similar channel size (3D, 10-ring) and different channel intersection volume, using UV-Raman spectroscopy. While these samples had similar surface areas, acid site densities (except for ZSM-5 with lower acid density compared to other samples), and crystal sizes, the different deactivation rate were obtained. They could find the correlation between the rate of deactivation and intersection volume for these zeolites meaning that faster deactivation happened over the zeolite with larger intersection volume. Therefore, TNU-9 with largest intersection volume deactivated first followed by IM-5, and ZSM-5 with relatively smaller volume. In addition, the heavier coke components (arenes with more than two rings) were found in zeolite with the larger intersection volume.

5.7.4. Acidity and coke content

The zeolite acidity is known as a parameter which contributes in coke formation [63]. it is tempting to investigate whether any relationship exists between the deposited coke in the studied zeolites and their acid concentrations. As the acid strength values of the zeolites in this work were similar for all samples, hence only the influence of acid site concentration is considered (see section 3.4).

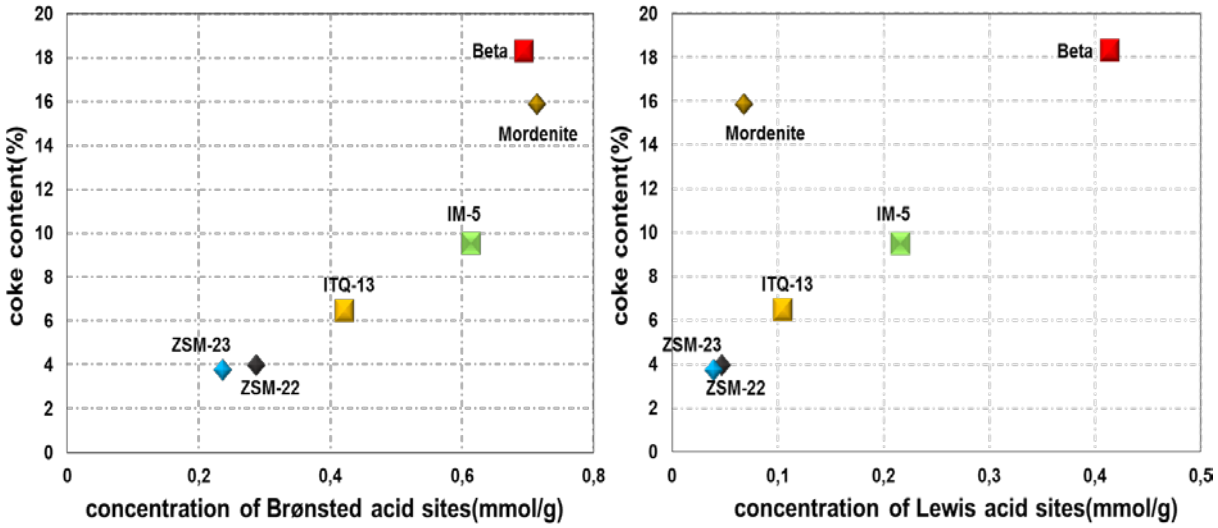

Figure 5.26: coke content versus Brønsted acid site density (left panel) and Lewis acid site density (right panel) for ZSM-22, ZSM-23, ITQ-13, IM-5, Mordenite and Beta zeolites.

Fig. 5.26 depicts the total coke value versus total concentration of Brønsted acid sites (left panel) and Lewis acid sites (right panel), which were obtained by pyridine adsorption measurement performed by S. Kwak [46]. It seems that in both graphs a linear relation between the coke content and density of acid sites can be established, Mordenite is an exception respect to its Lewis acid site concentrations and coke content. ZSM-22 and ZSM-23 with the lowest amount of acid concentrations showed the lowest value of coke content, while ITQ-13 and IM-5 with relatively higher concentration of acid sites appeared with higher coke content. The samples with the highest acid concentration, Mordenite and Beta, occupied the almost top right of the graph with the highest coke values.

5.7.5. Surface area and coke content

Other factors such as acid strength, total surface area of the fresh zeolites, crystal size, the time on stream/catalyst lifetime, and residence time of the components inside the catalysts, might have also impact on coke formation. For instance, slightly higher amount of coke for ZSM-22 (3.9) compared to ZSM-23 (3.53) with WHSV = 2 $gg_{cat}^{-1}h^{-1}$, may be due to the differences in crystal size which is 10 times bigger in the case of ZSM-22. In sample with the bigger sized-crystals, molecules should travel longer distances in order to reach the active sites which increase the probability of further reactions and coke formation [31, 63, 107]. The coke content and surface area are plotted in Fig. 5.27. As seen, the coke content linearly

increased with increasing the specific surface area, Beta and Mordenite with both the highest surface areas and coke contents and ZSM-22 and ZSM-23 with both the smallest surface area and coke content were terminal points.

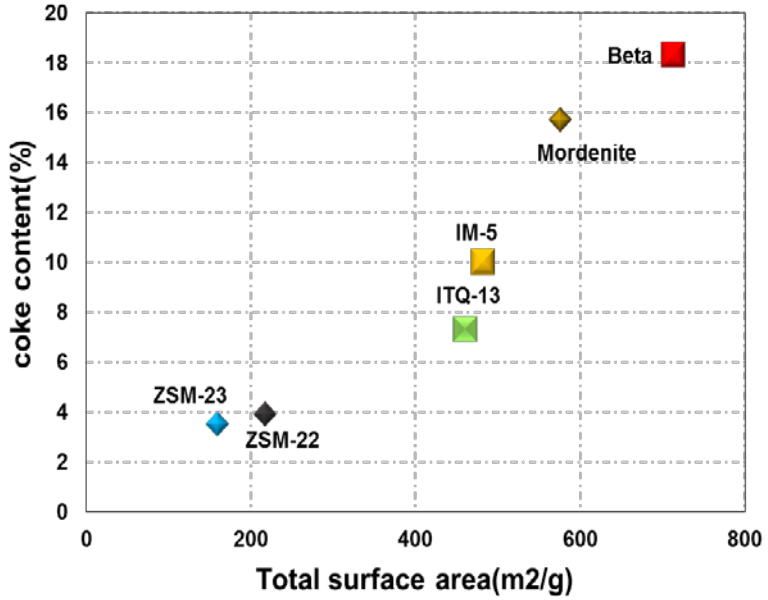

Figure 5.27: coke content versus BET total surface area for ZSM-22, ZSM-23, ITQ-13, IM-5, Mordenite and Beta zeolites.

In conclusion, for the studied zeolites in this work, ZSM-22, ZSM-23, Mordenite, ITQ-13, IM-5, and Beta, the pore structure/intersection size, acid concentration and catalyst surface area are the most important factors which determine the total amount of coke formed inside these zeolites. As these parameters also scale with each other, which means it is difficult to distinguish whether only one, or more, of these parameters contribute to coke formation.

5.8. Catalyst deactivation and theoretical models

Catalyst becomes gradually deactivated with time on stream during the MTH reaction mostly due to coke formation. Coke is referred to any non-desorbed by-products which made of a mixture of low volatility and hydrogen deficient compounds of high molar mass of mono/poly aromatic compounds [31]. Coke species may be originated from reactant(s), product(s) or even both. When the deactivation cause by mainly converting reactant(s) to coke precursors, the deactivation profile is resemble to an inverse S-shaped curve, while if products mainly contribute to coke formation the slope of the deactivation curve would be decreased with time on stream.

A new idea for catalyst deactivation during the MTH reaction was given by Janssens [40] in 2009. He proposed a model based on the reduction of the effective mass of catalyst during MTH reaction with time on stream. The idea came from the observation that product distribution over H-ZSM-5 during the MTH reaction was similar to those caused by increasing the space velocity or feed rate [40]. He assumed that MTH is a first order reaction to methanol, and considered a deactivation rate which is proportional to methanol conversion. By taking into account these assumptions, Janssens found a linear relation between the catalyst lifetime to 50% conversion and the applied contact time (W/F catalyst mass over the total flow of gas) for the MTH catalyst showed the full initial methanol conversion. This deactivating rate which calculated as 1/slope is not depending anymore on the catalyst activity and can be used for direct calculation of catalyst deactivation.

Using the Janssens's model for catalyst deactivation encounters some limitations. First, the deactivation can be assumed as loss of active sites if the deactivation step is a non-selective process meaning that coke formation does not affect the product selectivity (see section 5.1.3 and 5.2.3). Second, if the MTH reaction considered as a first order then the first step of initial hydrocarbon pools formation will be ignored which is not correct as the MTH reaction is known as autocatalytic reaction. Third, in this model only the reactant (methanol) is considered as the main source of coke formation and deactivation.

In order to cover the limitations the new Autocatalytic deactivation model was proposed in 2013 [41]. In contrast to the Janssens model, in this model the methanol conversion assumed to be an autocatalytic reaction in which the hydrocarbon pools formed in the initiation step are

a trigger or supply for the second/autocatalytic step while the hydrocarbon products are mainly formed in the second step as follows:

$R \xrightarrow{k_1} P$	initiation step
$R + P \xrightarrow{k_2} 2P$	autocatalytic/accelerating step

Also in this model, the assumption that the loss of active sites or deactivation rate is proportional to methanol conversion is still valid.

For an autocatalytic reaction such as MTH reaction, plotting the methanol conversion versus contact time will give an S-shaped curve as seen in Fig. 5.28 [41]. In Fig. 5.28, the grey solid line shows the first order reaction in methanol conversion, while the black solid line displays an autocatalytic reaction with an initiation step where the methanol conversion is low. The critical contact time ($\tau_{critical}$) as shown in Fig. 5.28 is the contact time needed to form first hydrocarbon pool species as a trigger for autocatalytic step. This parameter ($\tau_{critical}$) might be varied by catalyst topology and reaction conditions.

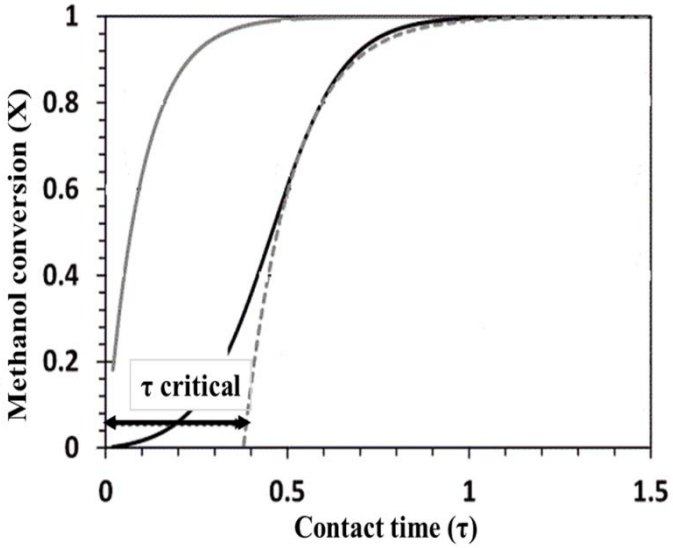

Figure 5.28: Methanol conversion versus contact time for a first-order reaction (grey solid line) and an autocatalytic reaction (black solid line) [41]

In the laboratory scale, it is common to use a plug flow reactor (PFR) for catalysis studyies (see section 4.1.1 and 4.2.1). However, due to a mixing condition in PFR reactor, the catalyst bed can be further divided into different segments, where the concentrations of reactants and products are different. The catalyst bed can be divided into three sections as shown in Fig. 5.29 as follows: The first section is called the initiation zone, where the methanol and its equilibrium products; dimethyl ether (DME) and water, are mainly present while the hydrocarbons' concentration are very low. In the first section the methanol conversion is commonly below 10%. The second zone named as autocatalytic zone where the autocatalytic reaction between the reactant and products rather than solely reactant or products lead to products formation. The methanol conversion in this region is between 10 to 80%. Finally, the last section is the product zone where the reactions between the products are dominated while the methanol is already consumed and methanol conversion is exceeded by 80% [114].

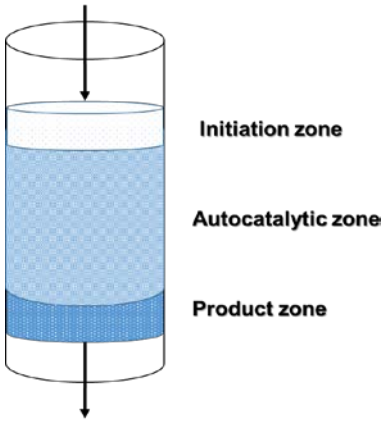

Figure 5.29: Three different zones: initiation, autocatalytic and product zones of catalyst bed placed in PFR reactor [114].

It has been shown that the deactivation of the studied zeolites in this work is a non-selective deactivation (see section 5.1.3 and 5.2.3). Thus, the deactivation can be assumed as loss of active sites according to the Autocatalytic deactivation model. In order to find the possible relation between the catalyst lifetimes to 50% conversion ($t_{0.5}$) and the applied contact time (τ_0) as suggested in the Autocatalytic deactivation model, these parameters are plotted and illustrated in Fig. 5.30 for all of the studied zeolites.

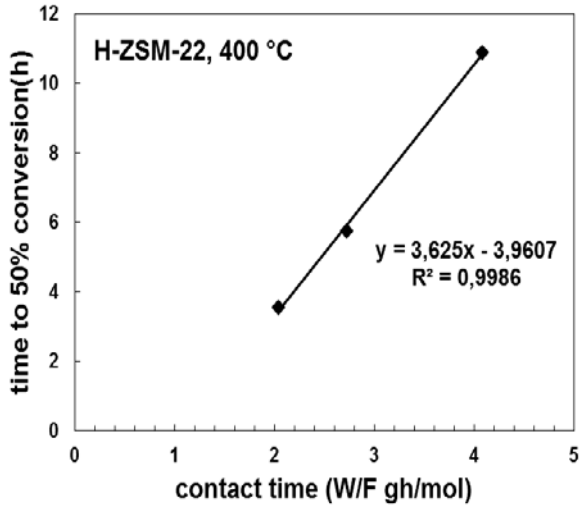
H-ZSM-22, 400 °C
y = 3,625x - 3,9607
R² = 0,9986
time to 50% conversion(h)
contact time (W/F gh/mol)

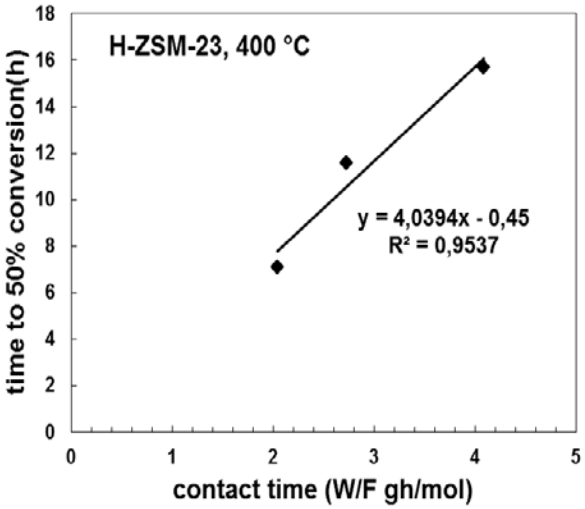
H-ZSM-23, 400 °C
y = 4,0394x - 0,45
R² = 0,9537
time to 50% conversion(h)
contact time (W/F gh/mol)

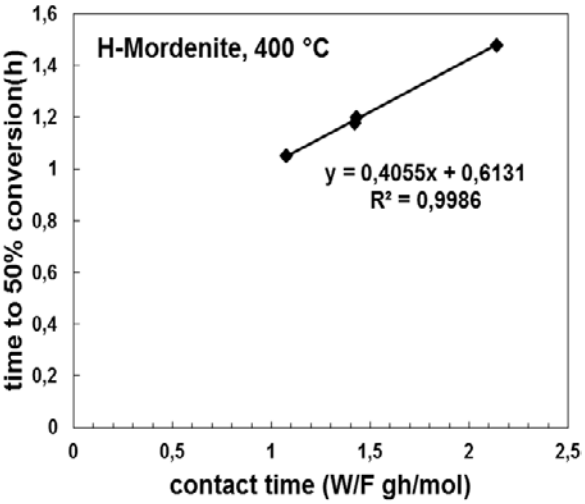
H-Mordenite, 400 °C
y = 0,4055x + 0,6131
R² = 0,9986
time to 50% conversion(h)
contact time (W/F gh/mol)

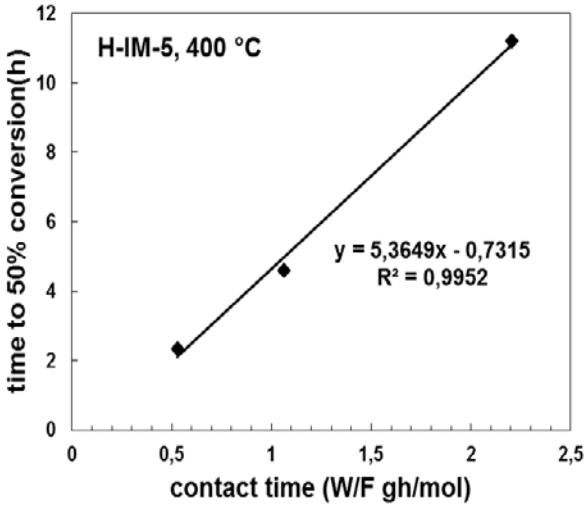
H-IM-5, 400 °C
y = 5,3649x - 0,7315
R² = 0,9952
time to 50% conversion(h)
contact time (W/F gh/mol)

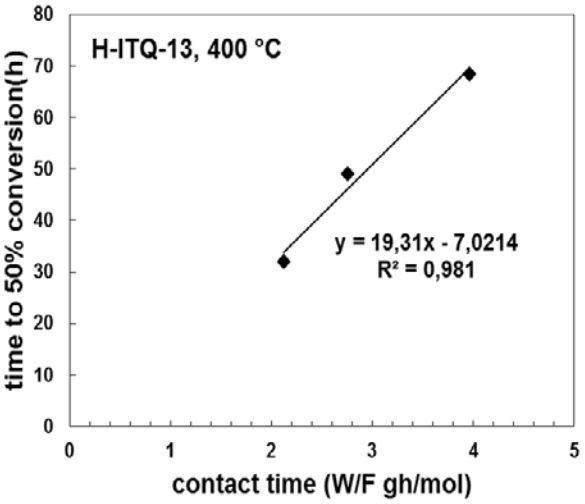
H-ITQ-13, 400 °C
y = 19,31x - 7,0214
R² = 0,981
time to 50% conversion(h)
contact time (W/F gh/mol)

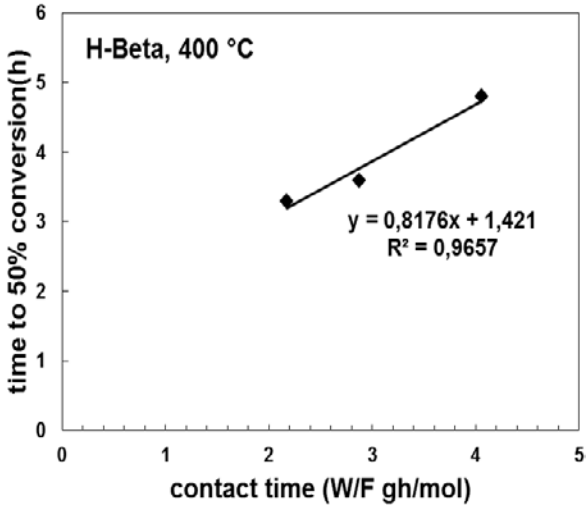
H-Beta, 400 °C
y = 0,8176x + 1,421
R² = 0,9657
time to 50% conversion(h)
contact time (W/F gh/mol)

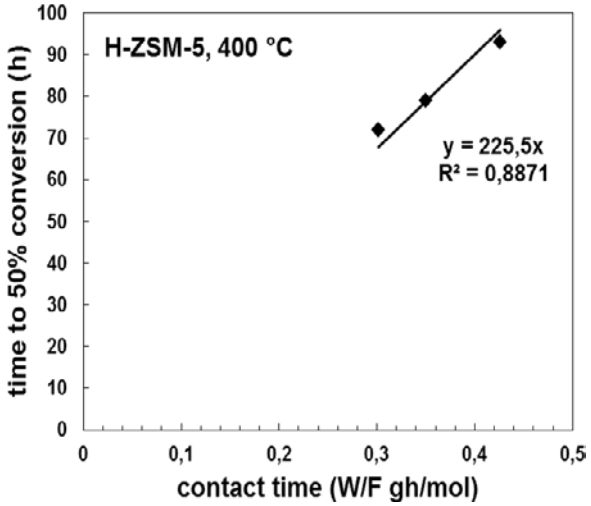

Figure 5.30: The MTH catalyst lifetime to reach 50% conversion as a function of applied contact time(weight-to-total Flow) for; H-ZSM-22, H-ZSM-23, H-Mordenite, H-IM-5, H-ITQ-13, H-Beta and H-ZSM-5 as indicated in the graphs at 400 °C and Pp_{MeOH} =13 kPa.

As seen from Figs. 5.30, a linear correlation between $t_{0.5}$ and τ_0 can be found for all the studied catalysts in agreement with the Autocatalytic deactivation model [41]. Furthermore, the deactivation constants and critical contact times are derived from the graphs and listed in Table 5.5 together with the conversion capacities and coke contents for various contact times for the sake of comparison.

From table 5.5, the highest critical contact time is obtained for H-ZSM-22 (1.11 gh/mol) while for other studied topologies: H-ZSM-23, H-IM-5, H-ITQ-13 and H-ZSM-5 the critical contact time calculated as 0.76, 0.14, 0.36 and 0.00 gh/mol in the same listed order. The critical contact time can be interpreted as the required contact time in order to build the enough concentration of hydrocarbons to trigger the autocatalytic MTH reaction at the reaction condition (see Fig. 5.28). According to the Autocatalytic deactivation model, critical contact time, is only dependant on the rate constants of the initiation and autocatalytic steps as well as the initial concentration of reactant and hydrocarbon products for a given set of reaction conditions [41]. The concentration of reactant (methanol) was set to be constant for all of the MTH reactions; the MTH reactions were performed with Pp_{MeOH} =13 kPa corresponds to 13% methanol concentration in He gas. Prior to each MTH reaction we may assume that all hydrocarbons were removed from each catalyst before testing by on-line pre-treatment. Thus, it can be said that the observed difference between the critical contact times over tested materials originated from the differences in rate constants of initiation and autocatalytic steps.

The ultimate value for critical contact time as zero which was obtained for H-ZSM-5 (see Fig. 5.30 and table 5.5) is in good agreement with the reported value by Janssens [41] for the same topology tested at 350 °C. The critical contact time as zero can be interpreted as almost all the catalyst bed is active during the MTH reaction. When $\tau_{critical}$ is zero, it means that the contact time needed to start accelerating/autocatalytic step is zero and we have a first-order reaction to methanol conversion.

Table 5.5: The critical contact times and deactivation constant derived from the plotted graphs of $t_{0.5}$ vs. τ_0 as shown in Fig. 5.27, together with the conversion capacities and coke content for each zeolite topologies at low, medium and high contact times at 400 °C and Pp_{MeOH}=13 kPa. Note that the values for low, medium and high contact times, which shown as subscript with parenthesis, might be different for some zeolite topologies and the reported total conversion capacity of H-ZSM-5 are assigned to the calculated conversion capacity till 10% methanol conversion. The critical contact time and deactivation constant for H-Beta and H-Mordenite could not be obtained according to the Autocatalytic deactivation model, see bulk text for explanation.

Zeolite	Critical contact time (τ) (gh/mol)	Deactivation constant (a) (g/mol)	Total conversion capacity			Coke content		
			Low contact time	medium contact time	high contact time	Low contact time	medium contact time	high contact time
H-ZSM-22	1.11	0.29	$7.8_{(2.1)}$	$8.2_{(2.8)}$	$9.8_{(4.3)}$	$3.9_{(2.1)}$	$3.4_{(2.8)}$	$4.6_{(4.3)}$
H-ZSM-23	0.76	0.24	$12.8_{(2.1)}$	$15.3_{(2.9)}$	$16.4_{(4.2)}$	$3.53_{(2.1)}$	$3.9_{(2.9)}$	$3.8_{(4.2)}$
H-Mordenite	-	-	$4.9_{(1.1)}$	$4_{(1.4)}$	$3.2_{(2.1)}$	$16.1_{(1.1)}$	$15.8_{(1.4)}$	$15.7_{(2.1)}$
H-IM-5	0.14	0.19	$23.9_{(0.5)}$	$21.1_{(1.1)}$	$23.1_{(2.2)}$	$9.1_{(0.5)}$	$9.4_{(1.1)}$	$10_{(0.5)}$
H-ITQ-13	0.36	0.05	$61.6_{(2.1)}$	$64.9_{(2.7)}$	$62.3_{(4)}$	$7.3_{(2.1)}$	$6.0_{(2.7)}$	$6.1_{(4)}$
H-Beta	-	-	$7.6_{(2.2)}$	$6.2_{(2.9)}$	$5.5_{(4.1)}$	$18.3_{(2.2)}$	$18.2_{(2.9)}$	$18.4_{(4.1)}$
H-ZSM-5	0	0.00	$916_{(0.3)}$	$875_{(0.35)}$	$788_{(0.4)}$	-	-	$9.6_{(0.4)}$

In contrast, a significant critical contact time (1.11 gh/mol) for H-ZSM-22 tested with contact times between 2-4 gh/mol suggests that a part of catalyst is rather inactive which also led to less formation of coke (~ 4%) when the catalyst became totally deactivated (see Table 5.5). With an increasing the contact time between 2-4 gh/mol for H-ZSM-22, the amount of coke in the totally deactivated catalyst also increased as well as the total methanol conversion capacities (see Table 5.5). At lower applied contact times, larger fraction of catalyst bed was inactive which led to less coke and less conversion capacities compared to the longer contact times. The similar trend can be found for H-ZSM-23 as well.

Previously, a critical contact time of 0.7 gh/mol was reported for H-ZSM-22 (Si/Al=50) tested at 400 °C with contact times between 1-2 gh/mol, where the applied and critical contact times were close [41]. In order to be able to compare the deactivation behaviour of the MTH catalysts according to the Autocatalytic deactivation model, $t_{0.5}$ must be calculated well above

the critical contact time as noted by Janssens et al. [41] which seems to be fit better with chosen contact times in this work for H-ZSM-22.

The deactivation constants are derived from Fig. 5.30 according to the Autocatalytic deactivation model as follows:

$$a\ (g_{cat}/mol_{total}) = \frac{\tau(applied\ contact\ time) - \tau(critical\ contact\ time)}{t_{0.5}}$$

In fact this parameter, deactivation constant, is 1/slope of the lines shown in Fig. 5.30. The order of deactivation constant for H-ZSM-22, H-ZSM-23, H-IM-5, H-ITQ-13 and H-ZSM-5 is as follows:

0.29 (H-ZSM-22) > 0.24 (H-ZSM-23) > 0.19 (H-IM-5) > 0.05 (H-ITQ-13) > 0.00 (H-ZSM-5)

From data, it is expected that the H-ZSM-22 with the highest (0.29 g/mol) and H-ZSM-5 with the lowest (0.00 g/mol) deactivation constant became deactivated within shorter and longer times on stream, respectively which is in line with the values obtained during the stability tests (see section 5.1). Furthermore, the similar trend as obtained here has been found for the rest of the zeolites during the stability tests, see section 5.1. Janssen et al. [41] reported a deactivation constant of 0.0192 g/mol for H-ZSM-5 (Si/Al=50) tested at 350 °C which is relatively higher than the obtained value here. However, the differences might be interpreted while considering the temperature differences for these MTH reactions as the H-ZSM-5 deactivate faster at lower reaction temperatures e.g. 350 °C. Since the deactivation constants calculated according to the Autocatalytic deactivation model is only depend on the lifetime to 50% hydrocarbons yields and applied contact times, this parameter can be derived independent of the catalyst activity. Therefore, with the test protocol which used in this work, direct comparison of different rates at different temperatures become possible.

Referring to Table 5.5, while comparing the conversion capacities for H-IM-5 and H-ITQ-13, 3D 10-ring channels with cross sections of 24.1 and 20 $Å^2$ respectively, three times higher value for conversion capacity was achieved over H-ITQ-13 compared to H-IM-5 which might be understood while considering the three times higher deactivation constant for H-IM-5 than H-ITQ-13. As seen from Table 5.5, the autocatalytic model gives the same stability trends as the total conversion capacity data.

In Fig. 5.30, two zeolites; H-Mordenite (1D 12-ring with cross-section of 35.7 $Å^2$) and H-Beta (3D 12-ring with cross-section of 34.7 $Å^2$) crossed the y-axis above zero, thus the calculated critical contact times would be negative which is meaningless. On the other hand, the total conversion capacities values for H-Mordenite and H-Beta decreased with increasing the contact time; the opposite trend was found for the rest of tested zeolites. Note that the reported conversion capacity for H-ZSM-5 also showed the same trend but it should be taken into account that these values of H-ZSM-5 are not the total conversion capacity since the MTH reaction stopped at 10% conversion. However, in the research done by Bleken et al. [45], they found that conversion capacity to 0% conversion was independent of contact time.

The changes in total conversion capacities with contact time for H-Mordenite and H-Beta may suggest that the hydrocarbon products were the main source of coke formed in these zeolite topologies, instead of methanol. Due to the larger channel size of the 12-ring zeolites, H-Mordenite and H-Beta, the products such as aromatic compounds can diffuse in and out of the zeolite channels which can increases the probability of further reactions which led to coke formation. Thus, it can be assumed that for the larger channels sized zeolites, e.g. H-Mordenite and H-Beta, the coke profile would be the opposite of the previous studied zeolites meaning that coke zone formed in the last part of the catalyst bed where concentration of products are rather high and the methanol is depleted (see Fig. 5.29). Therefore, the autocatalytic deactivation model cannot be applied to predict the deactivation behaviour over these two zeolites as one of the main assumptions of this model is rejected by considering the products as main source of deactivation.

5.8.1. Possible mechanisms of coke formation

From literatures, methane (C_1) was proposed to be as a stable primary product which formed directly from methanol and secondary product [110]. One mechanism as pictured in Fig. 5.31, is the reaction between methanol and surface methoxy species which led to methane together with coke species.

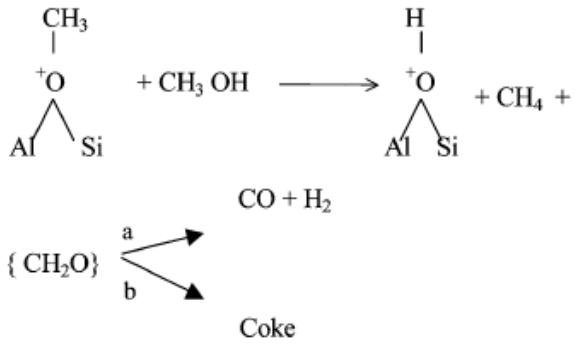

Figure 5.31: mechanism to explain the formation of methane as a primary stable product [110].

However, as a secondary product reaction between methoxy group and large molecules as a hydride source has been proposed for methane formation which also ends up with coke species.

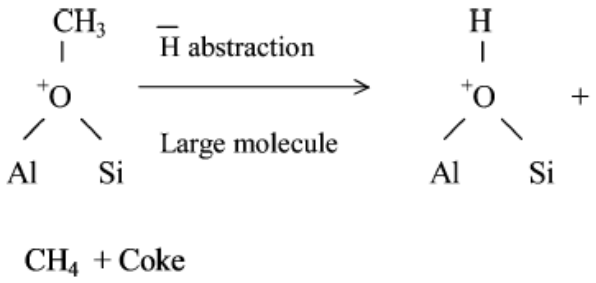

Figure 5.32: Proposed mechanism for methane formation as a secondary product [110].

Thus, the higher selectivity of methane might be connected to higher coke content as well. Looking at product selectivity/yield over H-Mordenite and H-Beta (see section 5.4 and Appendix 5), in both structures a higher selectivity towards C_1 can be found at higher methanol conversion levels compare to the other structures. To have a better view, methanol conversion corresponds to 5% methane selectivity for each tested structure is shown in Fig. 5.33. As seen, for H-Mordenite and H-Beta the corresponding conversions were 98% and 74% respectively which is considerably higher compared to the other structure which were below 20%. Also from selectivity graphs (Appendix 5), selectivity towards methane showed a sharp increasing with time on stream in case of H-Mordenite from 5 to ~ 70% and for H-Beta from 5 to ~ 50% meaning that the heavy coke formation occurred in these two structures in line with data from coke analysis content (see Table 5.5).

As back diffusion can of large aromatics and aliphatics compounds is more probable over H-Mordenite and H-Beta due to their larger channel sizes, coke species may form by proposed mechanism pictured in Fig. 5.32. The simultaneous decrease in C_{6+} aliphatics and aromatics selectivity and increase in methane selectivity might be indicated that large molecules such as C_{6+} aliphatics and aromatics converted to coke species according to the mechanism (Fig. 5.32). However, other possible reactions can be methylation of aromatics with alkene followed by cyclisation and hydride transfer and finally to coke precursors [108].

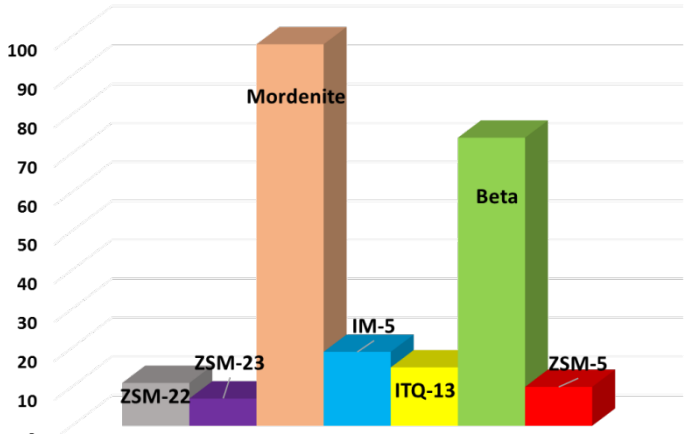

Figure 5.33: Methanol conversion correspond to 5% methane selectivity over different zeolite structures at 400 °C and PpMeOH= 13kPa.

Chapter6: Conclusions and further work

In this study, seven different zeolites structures have been studied in MTH reaction: H-ZSM-22, H-ZSM-23, H-Mordenite, H-IM-5, H-ITQ-13, H-Beta and H-ZSM-5 at 400 °C and Pp_{MeOH}=13 kPa. In general, these zeolites are all active for methanol conversion. However, the catalytic behavior of the materials strongly depends on the zeolite structure as well as concentration of acid sites.

All topologies displayed full initial conversion at 400 °C but lifetimes varied considerably in the order of: ZSM-5 >> ITQ-13 > IM-5 > ZSM-23 > ZSM-22 > Beta > Mordenite. H-Beta and H-Mordenite, 12-ring zeolite structures, have a faster deactivation than 10-rings zeolites structures. 3D 10-ring zeolites presented a higher lifetime than 1D 10-ring structures (ZSM-22 and ZSM-23). Analysis of the relative amount of coke in the spent catalyst after the life-time tests showed heavy coke formation over 12-ring zeolites, H-Mordenite and H-Beta.

Different zeolite structures have a notable influence on the products distribution of the MTH reaction over these catalysts. Considering the dual-cycle mechanism, in 12-rings zeolite structure (H-Beta and H-Moredenite) the arene cycle is more active, resulting in high aromatic yield and lower C_{5+} aliphatics. However, in 10 rings 1D zeolites, ZSM-22 and ZSM-23, the arene cycle is suppressed and an aromatic free C_{6+} fraction is observed. 3D 10-rings zeolite structures showed almost equal values for aromatics, C_{5+} aliphatics and C_2, indicating that both alkene and arene cycle are actives. The product yields at a certain methanol conversion over H-ZSM-22, H-ZSM-23, H-IM-5, H-ITQ-13, H-Beta and H-ZSM-5 showed that the product selectivity is independent of deactivation named as non-selective deactivation. In case of H-Mordenite due to its rapid deactivation the observation was not clear and need more data points. However, the changes in selectivity over time on stream can be interpreted as changes in contact time as previously proposed by Janssens [40, 41].

The deactivation constant for each zeolite structure was calculated according to the autocatalytic kinetic model, plotting the catalyst lifetime to 50% conversion against the applied contact time, in line with the trend found during the stability tests of MTH zeolites. Previously, autocatalytic model has been employed in the experimental data obtained for H-ZSM-22 and H-ZSM-5 and a good relation has been reported.

In this study, the autocatalytic deactivation model was expanded to other 1D and 3D zeolite structures e.g. H-ZSM-23, H-Mordenite, H-ITQ-13, H-IM-5 and H-Beta. For 12-ring zeolites (Beta with 3D and Mordenite with 1D channel) the model could not predict the deactivation behavior. It was suggested that reactions between products while the catalyst was depleted of methanol was responsible for formation of polyaromatics compound which then led to coke formation and finally deactivation of the catalyst. Characterization of the spent catalysts also proved that for H-Beta and H-Mordenite samples, the deactivation model differed from the other samples due to their heavy coke formation.

In conclusion, the autocatalytic deactivation model is only valid for 10-rings zeolite structure (ZSM-22, ZSM-23, ITQ-13, IM-5, ZSM-5), while cannot be applied to 12-rings zeolite structures, H-Beta and H-Mordenite.

In order to possibly verify the conclusions of this work, it is good idea to make some more tests, for instance make separate characterization of different segments of the catalyst bed after testing. It would be also interesting to perform the catalytic tests over other zeolite structures for instance 8-ring channel zeolites to investigate the deactivation Autocatalytic model and find the limitations of this model. As catalysts deactivation as well as product selectivity strongly depends on the acid site density it would be useful to test different zeolites structures with similar acid densities to find other factors that might lead to different catalytic behavior during MTH reaction.

Appendix

Appendix 1

Supplementary information on the fresh catalysts characterisation done by S. Kwak [46].

a) FT-IR spectra with increasing dosage of CO as a probe molecule

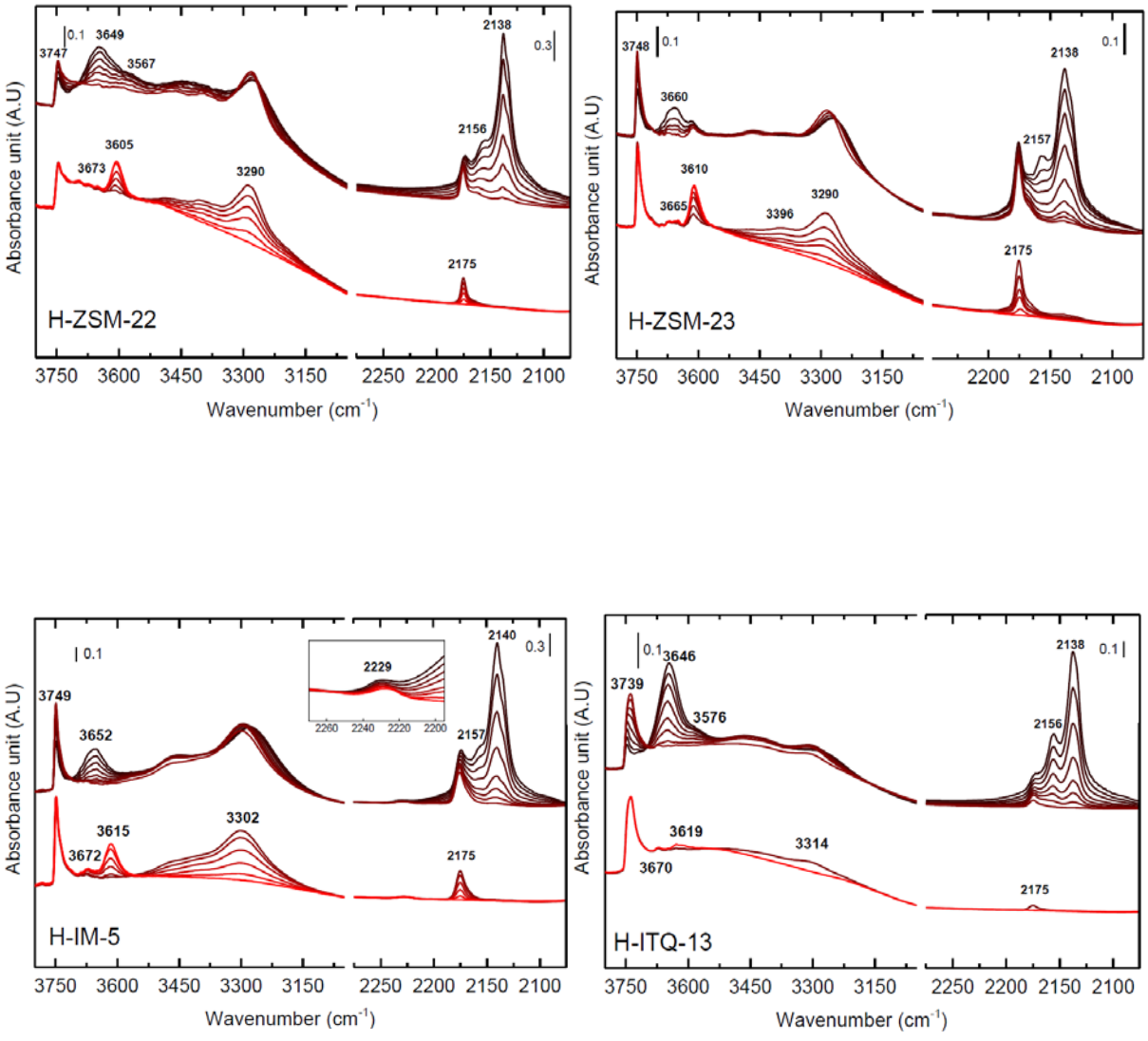

b) XRD patterns

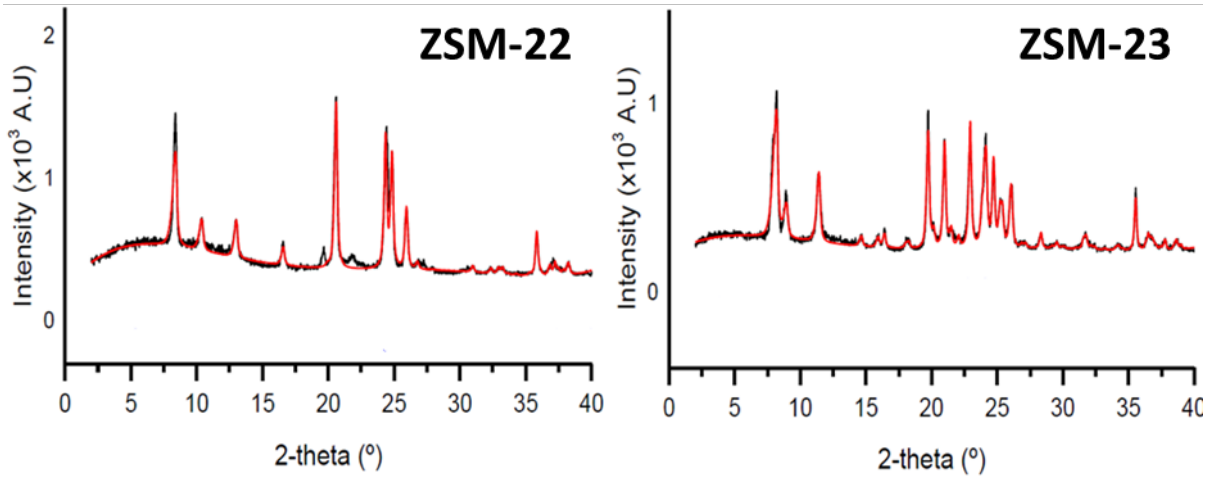

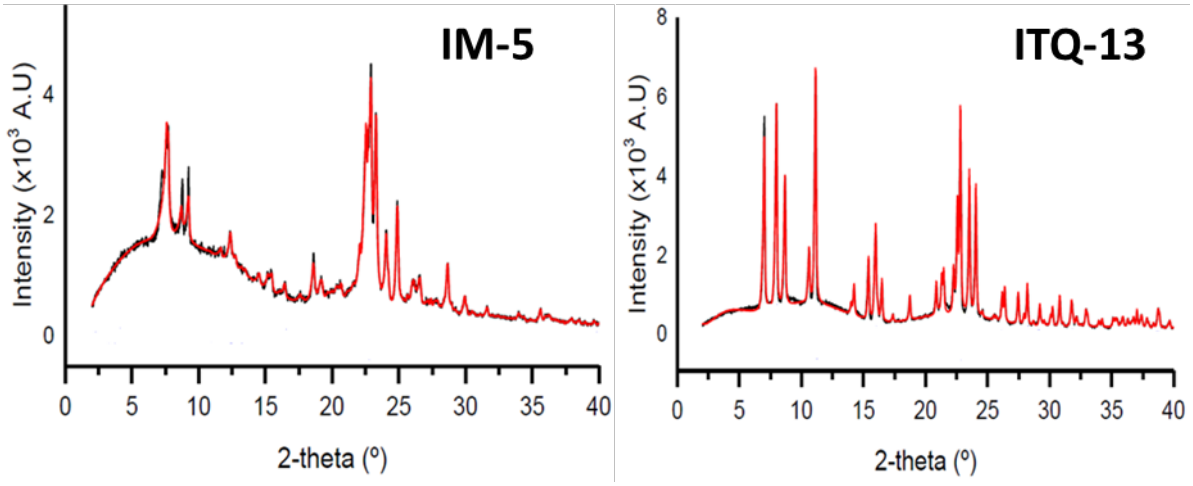

Appendix 2

Temperature profile of the oven

To have a reproducible data and stop further reaction between products, it is necessary to find out the isothermal zone of the oven. The below graph shows temperature versus the distance from the catalyst bed. The U-shaped quartz reactor filled with 100 mg of silica and a thermocouple was placed on the catalyst bed to monitor the temperature. The outlet of reactor was isolated by wool to reduce the heat loss and a flow of He gas was flown through the reactor. A stable range of temperature can read from the catalyst bed up to 2cm above it as per below graph. For all reactions the reactor is always placed in the isothermal zone of the oven.

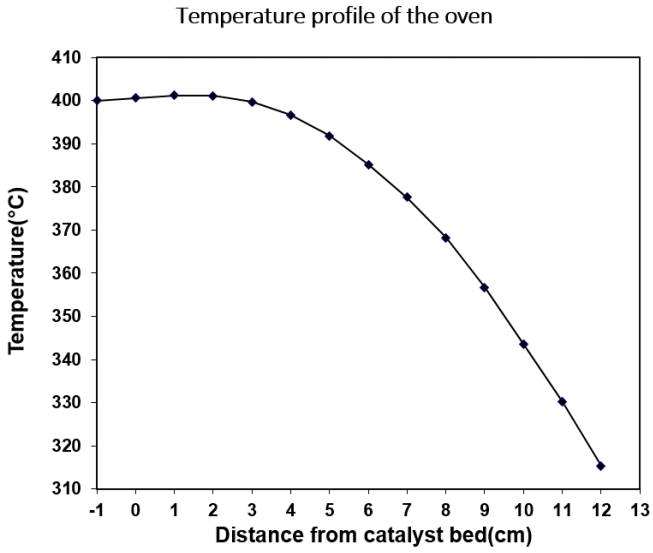

Appendix 3

Reproducibility

Reproducibility of MTH reaction's results for H-ZSM-23 sample was studied at 400 °C and $Pp_{(MeOH)}$ = 13kPa. The first outstanding left curve is related to a reaction in which He was bubbled through the saturator about 15 min before feeding the catalyst in. The other curves are related to a condition in which He was bubbled through the saturator evaporator at least 3 hours before MTH reaction starts. Although a clear difference in catalyst lifetime can be seen for these two conditions, but the product selectivities were almost the same. A good data reproducibility could be achieved when He bubbled through the saturator at least 3 hours prior MTH reaction starts. It might be concluded that after this period of time, a stable condition will be reached in the saturator resulting in a constant and stable partial pressure of methanol.

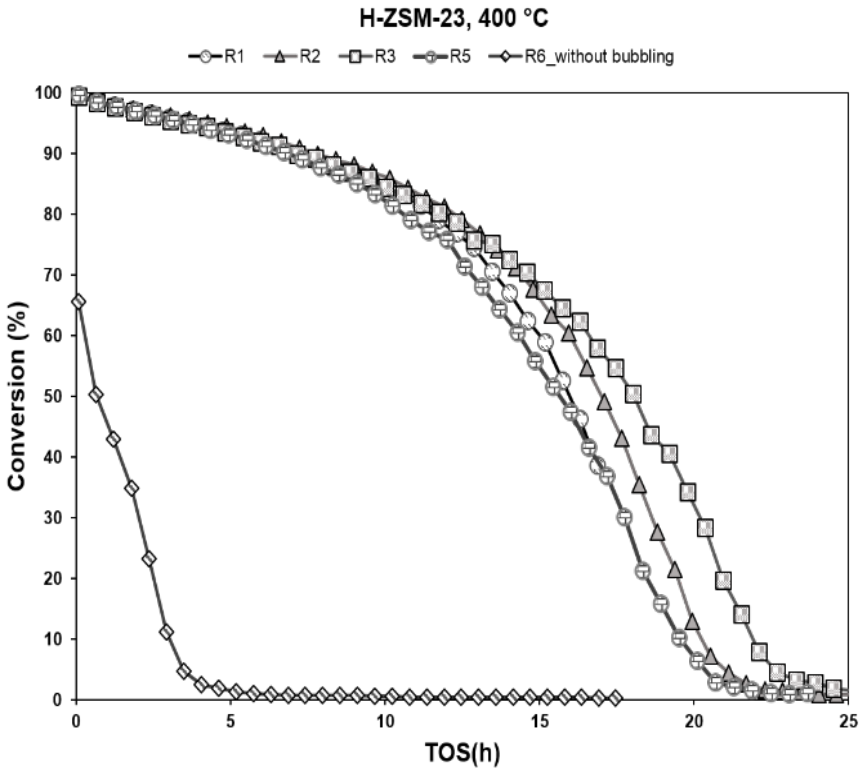

Appendix 4

Absence of by-pass

The reaction quotient ($Q = \frac{[DME] \times [H_2O]}{[MeOH]^2}$) of methanol and the condensation product of methanol (DME) were calculated for each test to ensure the absence of methanol by-pass (below graph). The graph was plotted for H-IM-5 at WHSV=2 ($gg_{cat}^{-1}h^{-1}$) at 400 °C. Each mole of methanol converting to DME and hydrocarbons (products) produces 0.5 and 1 mole of water, respectively.

$$2\,CH_3OH \leftrightarrow CH_3OCH_3 + H_2O$$

The experimental data proved the equilibrium for methanol and DME in catalytic reaction condition within the range of 10-90% methanol conversion.

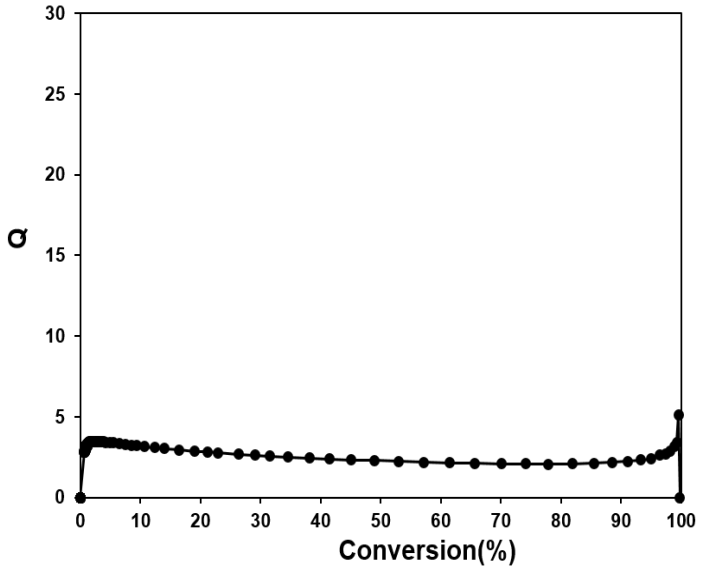

Appendix 5

Product selectivity versus time-on-stream for 7 studied zeolites at 400 °C and Pp_{MeOH}=13 kPa

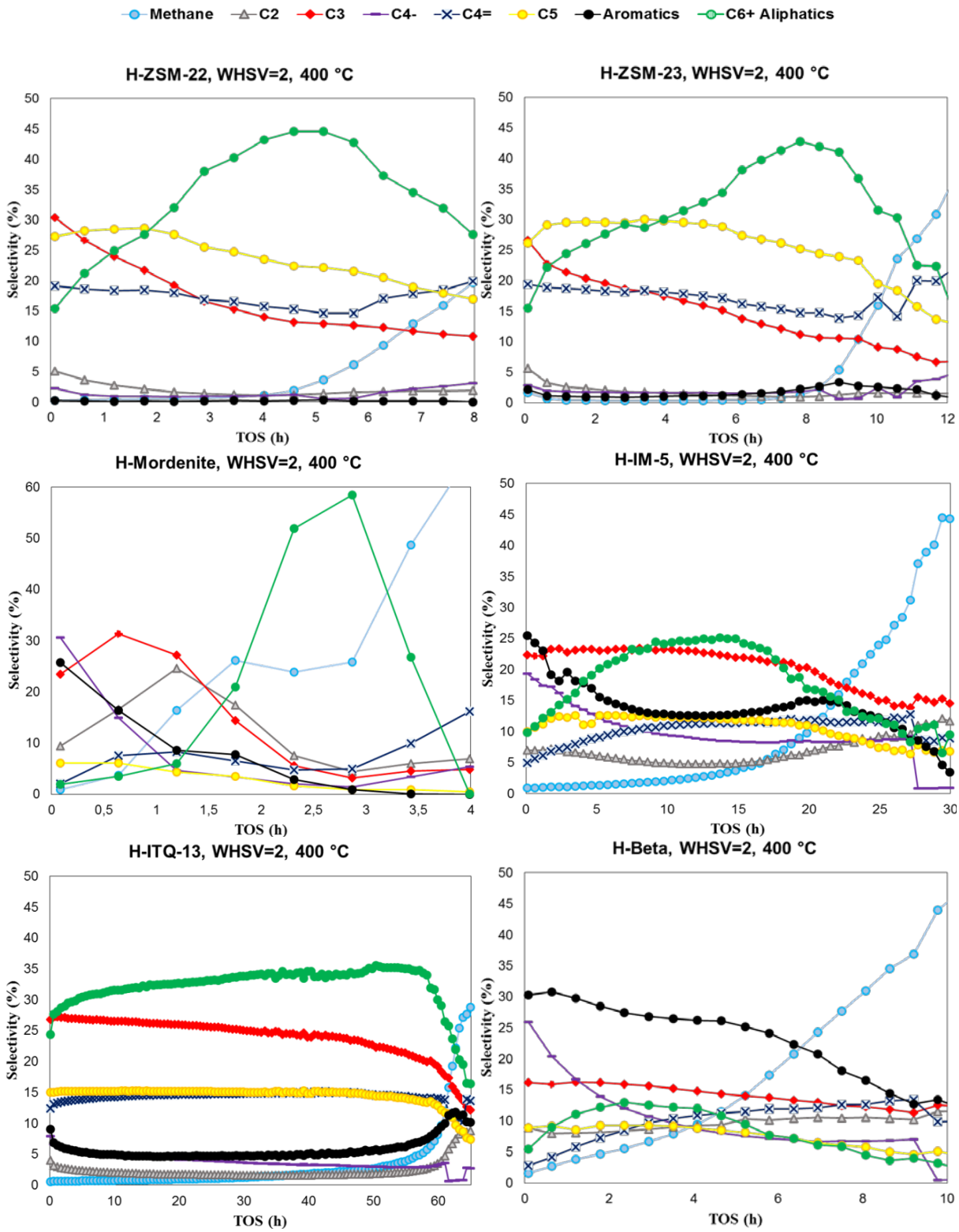

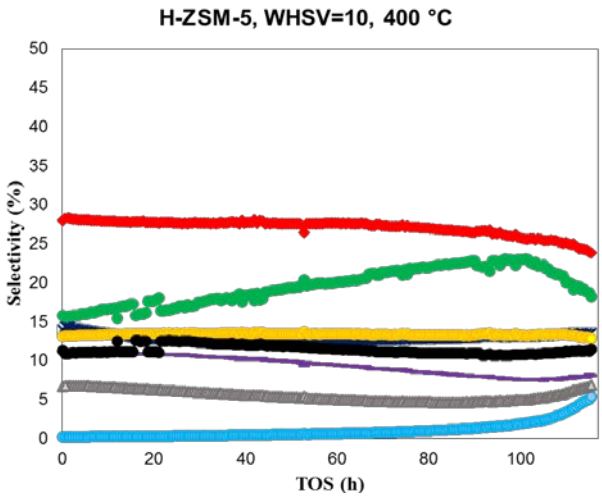
H-ZSM-5, WHSV=10, 400 °C
Selectivity (%)
50
45
40
35
30
25
20
15
10
5
0
0
20
40
60
80
100
TOS (h)

Appendix 6

The TGA plots of the sample are illustrated in below graphs. Accordingly, the mass fraction of coke as a function of time was calculated as follows:

$$\text{Mass fraction of coke (t)} = \frac{(\text{mass of sample})_{\text{at } 200} - (\text{mass of sample})_{t}}{(\text{mass of sample})_{\text{at } 200} - (\text{mass of sample})_{\text{end of TGA}}}$$

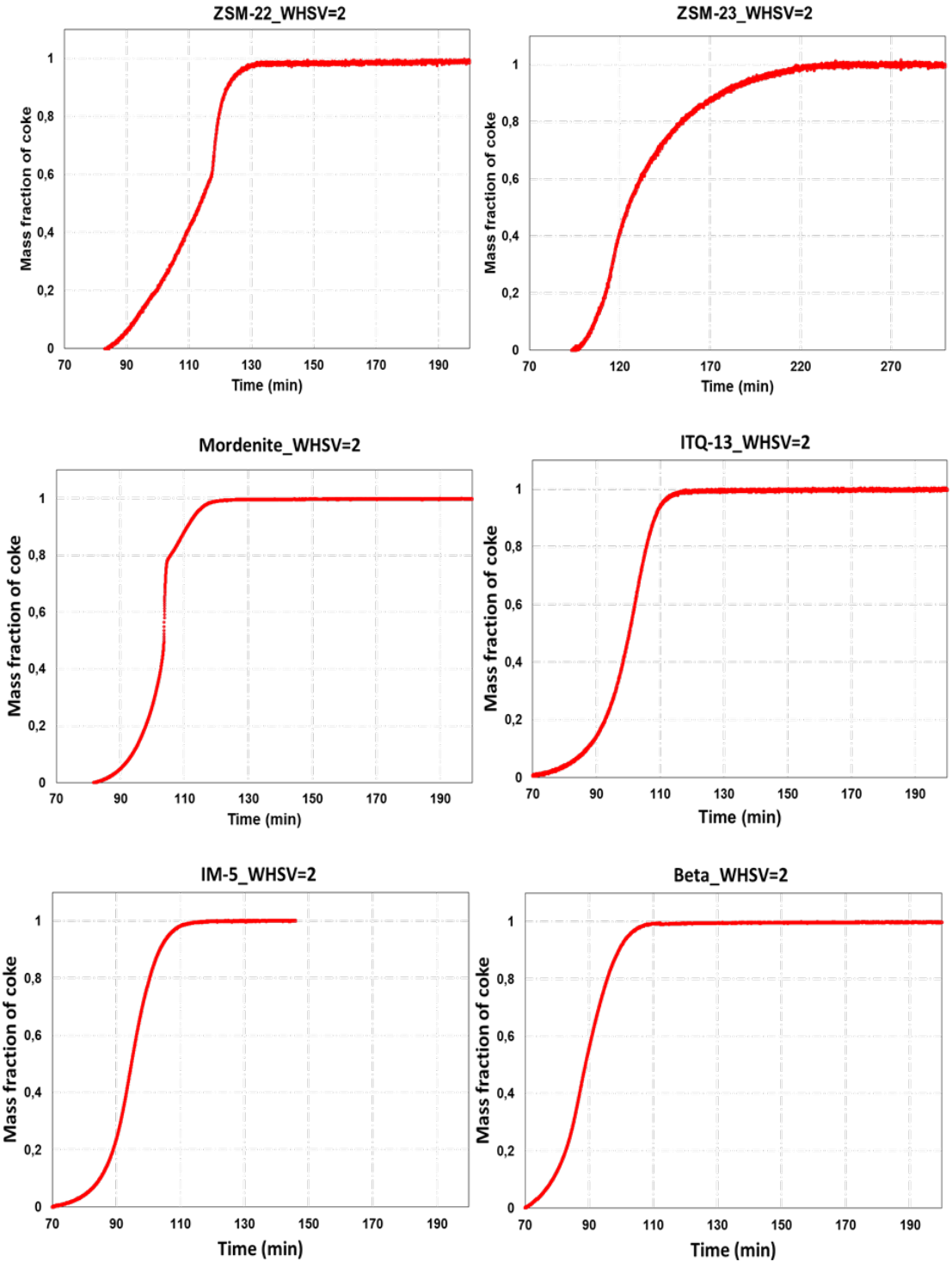

Appendix 7

The temperature of saturation determines the partial pressure of methanol and the following calculations the total flow and weight hourly space velocity can be obtained.

$$\frac{Flow_{total}}{Flow_{MeOH}} = \frac{P_{MeOH}}{P_{total}}$$

The flow rate of methanol can be calculated using the ideal gas law:

$$n_{MeOH}\left(\frac{mol}{h}\right) = \frac{P_{atm} \times Flow_{MeOH}}{RT}$$

The corresponding weight hourly space velocity and applied contact time calculated as follows:

$$WHSV\ (gg_{cat}^{-1}h^{-1}) = \frac{m_{MeOH}\,(g/h)}{m_{cat}}$$

$$contact\ time\ (\frac{gh}{mol}) = \frac{m_{cat}}{Flow_{total}\,(\frac{mol}{h})}$$

References

[1] I. Chorkendorff, J.W. Niemantsverdriet, *Concepts of Modern Catalysis and Kinetics*, 2nd ed., Wiley-VCH Verlag GmbH & Co. KGaA, **2007**.

[2] A. Dyer, *An introduction to Zeolite Molecular Sieves*, 1st ed., John Wiley & sons, **1988**.

[3] C. Baerlocher, L.B. McCusker, D.H. Olson, *Atlas of zeolite framework types*, 6th ed., Elsevier, **2007**.

[4] A. Dyer, *in: Ion-Exchange Properties of Zeolites and Related Materials,* (Eds.: G. Centi) Introduction to zeolite science and practice, Elsevier, **2007**.

[5] B. Shuai, Ph.D thesis, Utrecht university, **2009**

[6] Avelino Corma, Marta Puche, Fernando Rey, Gopinathan Sankar, S.J. Teat, *Angewandte Chemie International Edition*, 42 **(2003)** 1156-1159.

[7] J.A. Lercher, A. Jentys, *Infrared and raman spectroscopy for characterizing zeolites*, Elsevier B. V., **2007**.

[8] S. Teketel, M. Westgård Erichsen, F. Lønstad Bleken, S. Svelle, K.-P. Lillerud, U. Olsbye, 26 **(2014)** 179-217.

[9] J.F. Haw, *Physical Chemistry Chemical Physics*, 4 **(2002)** 5431–5441.

[10] W.O. Haag, R.M. Lago, P.B. Weisz, *Nature*, 309 **(1984)** 589-591.

[11] J.A. Lercher, A. Jentys, *Basic concepts in zeolite acid-base catalysis*, **2011**.

[12] R. Gounder, E. Iglesia, *Chemical Communications*, 49 **(2013)** 3491-3509.

[13] S. Teketel, Ph. D thesis, University of Oslo, **2012**

[14] F.J. Keil, *Microporous and Mesoporous Materials*, 29 **(1999)** 49–66.

[15] C.D. Chang, *Catalysis Reviews*, 26 **(1984)** 323-345.

[16] W. Wang, A. Buchholz, M. Seiler, M. Hunger, *American Chemical Society*, 125 **(2003)** 15260-15267.

[17] R.M. Dessau, R.B. LaPierre, *Journal of Catalysis*, 78 **(1982)** 136-141.

[18] R.M. Dessau, *Journal of Catalysis*, 99 **(1986)** 111-116.

[19] R.F. Sullivan, C.J. Egan, G.E. Langlois, R.P. Sieg, *Journal of the American Chemical Society*, 83 **(1961)** 1156-1160.

[20] T. Mole, G. Bett, D. Seddon, *Journal of Catalysis*, 84 **(1983)** 435-445.

[21] T. Mole, J.A. Whiteside, *Journal of Catalysis*, 82 **(1983)** 261-266.

[22] M. Bjørgen, U. Olsbye, D. Petersen, S. Kolboe, *Journal of Catalysis*, 221 **(2004)** 1-10.

[23] A. Sassi, M.A. Wildman, H.J. Ahn, P. Prasad, J.B. Nicholas, J.F. Haw, *The Journal of Physical Chemistry B*, 106 **(2002)** 2294-2303.

[24] M. Westgård Erichsen, Ph.D thesis, University of Oslo, **2014**

[25] I.M. Dahl, S. Kolboe, *Journal of Catalysis*, 161 **(1996)** 304-309.

[26] M. Bjørgen, S. Svelle, F. Joensen, J. Nerlov, S. Kolboe, F. Bonino, L. Palumbo, S. Bordiga, U. Olsbye, *Journal of Catalysis*, 249 **(2007)** 195-207.

[27] S. Svelle, F. Joensen, J. Nerlov, U. Olsbye, K.-P. Lillerud, S. Kolboe, M. Bjørgen, *Journal of the American Chemical Society*, 128 **(2006)** 14770-14771.

[28] S. Svelle, U. Olsbye, F. Joensen, M. Bjørgen, *The Journal of Physical Chemistry C*, 111 **(2007)** 17981-17984.

[29] M. Bjørgen, F. Joensen, K.-P. Lillerud, U. Olsbye, S. Svelle, *Catalysis Today*, 142 **(2009)** 90-97.

[30] J.F. Haw, W. Song, D.M. Marcus, J.B. Nicholas, *Accounts of Chemical Research*, 36 **(2003)** 317-326.

[31] B. Wang, Ph.D. thesis, University College London, **2007**

[32] C.H. Bartholomew, *Applied Catalysis A: General*, 212 **(2001)** 17-60.

[33] M. Guisnet, P. Magnoux, *in: Deactivation of zeolites by coking. Prevention of Deactivation and Regeneration,* (Eds.: E. Derouane, F. Lemos, C. Naccache, F. Ribeiro) Zeolite Microporous Solids: Synthesis, Structure, and Reactivity, Springer Netherlands, **1992**, pp. 457-474.

[34] D.M. Bibby, N.B. Milestone, J.E. Patterson, L.P. Aldridge, *Journal of Catalysis*, 97 **(1986)** 493-502.

[35] R.H. Meinhold, D.M. Bibby, *Zeolites*, 10 **(1990)** 121-130.

[36] D.M. Bibby, *Applied Catalysis A: General*, 93 **(1992)** 1-34.

[37] X.Y. Guo, Z.W. Liu, B. Zhong, *Microporous and Mesoporous Materials*, 23 **(1998)** 203-209.

[38] A.d. Lucasa, P. Canizaresa, A. Duranb, *Applied Catalysis A: General*, 206 **(2001)** 87-93.

[39] M. Choi, K. Na, J. Kim, Y. Sakamoto, O. Terasaki, R. Ryoo, *Nature*, 461 **(2009)** 246–249.

[40] T.V.W. Janssens, *Journal of Catalysis*, 264 **(2009)** 130-137.

[41] T.V.W. Janssens, S. Svelle, U. Olsbye, *Journal of Catalysis*, 308 **(2013)** 122-130.

[42] H. Schulz, M. Wei, *Top Catal*, 57 **(2014)** 683-692.

[43] G. Qi, Z. Xie, W. Yang, S. Zhong, H. Liu, C. Zhang, Q. Chen, *Fuel Processing Technology*, 88 **(2007)** 437-441.

[44] J. Li, Y. Wei, Y. Qi, P. Tian, B. Li, Y. He, F. Chang, X. Sun, Z. Liu, *Catalysis Today*, 164 **(2011)** 288–292.

[45] F.L. Bleken, T.V.W. Janssens, S. Svelle, U. Olsbye, *Microporous and Mesoporous Materials*, 164 **(2012)** 190-198.

[46] S.H. Kwak, M. Sc. thesis, University of Oslo, **2014**

[47] A.W. Burton, *in: Powder Diffraction in Zeolite Science*, (Eds.: E.G.D. Arthur, W. Chester) Zeolite Characterization and Catalysis, **2010**, pp. 1-64.

[48] M.W. Erichsen, M. Sc. thesis, University of Oslo, **2010**

[49] G.T. Kokotailo, C.A. Fyte, *The Rigaku Jornal*, 12 **(1995)** 3-10.

[50] C. Baerlocher, L. B. McCusker, Database of Zeolite Structures, http://www.izastructure.org/databases/, Accessed: 13.02.2015

[51] K. Kalantar-zadeh, B. Fry, *Nanotechnology-Enabled Sensors*, Springer, **2007**.

[52] J. Goldstein, D.E. Newbury, D.C. Joy, C.E. Lyman, P. Echlin, E. Lifshin, L. Sawyer, J.R. Michael, *Scanning Electron Microscopy and X-ray Microanalysis*, 3rd ed., Springer, **2003**.

[53] P. Klobes, K. Meyer, R.G. Munro, N.I.o. Standards, Technology, *Porosity and Specific Surface Area Measurements for Solid Materials*, U.S. Department of Commerce, Technology Administration, National Institute of Standards and Technology, **2006**.

[54] K.S.W. Sing, D.H. Everett, R.A.W. Haul, L. Moscou, R.A. Pierotti, J. Rouquerol, T. Siemieniewska, *Pure Appl. Chem.* , 57 **(1985)** 603-619.

[55] S. Brunauer, P.H. Emmett, E. Teller, *Journal of the American Chemical Society*, 60 **(1938)** 309-319.

[56] B.C. Lippens, B.G. linsen, J.H.d. Boer, *Journal of Catalysis*, 3 **(1964)** 32-43.

[57] A. Galarneau, F. Villemot, J. Rodriguez, F. Fajula, B. Coasne, *Langmuir*, 30 **(2014)** 13266-13274.

[58] Xinsheng Liu, *in: Infrared and Raman Spectroscopy*, (Eds.: A.W. Chester, E.G. Derouane) Zeolite Characterization and Catalysis, Springer ScienceþBusiness Media B.V **2009**, pp. 197-222.

[59] J.W. Niemantsverdriet, *in: Vibrational Spectroscopy*, Spectroscopy in Catalysis An Introduction, WILEY-VCH Verlag GmbH & Co. KGaA, Weinheim, **2007**, pp. 217-248.

[60] G. Mestl, H. Knozinger, *in: Vibrational spectroscopies,* (Eds.: G. Ertl, H. Knözinger, J. Weitkamp) Handbook of Heterogenous Catalysis, **1997**.

[61] M. Hunger, *in: Catalytically Active Sites: Generation and Characterization,* Zeolites and Catalysis, Wiley-VCH Verlag GmbH & Co. KGaA, **2010**, pp. 493-546.

[62] V.B. Kazansky, *in: Spectral Study of Lewis Acidity of Zeolites and of its Role in Catalysis,* (Eds.: H.P. G. Ohlmann, R. Fricke) Studies in Surface Science and Catalysis, Elsevier, **1991**, pp. 117-131.

[63] B. Wang, G. Manos, *Journal of Catalysis*, 250 **(2007)** 121-127.

[64] S. Chen, G. Manos, *Journal of Catalysis*, 226 **(2004)** 343-350.

[65] J.W. Niemantsverdriet, *in: Diffraction and Extended X-Ray Absorption Fine Structure (EXAFS),* Spectroscopy in Catalysis An Introduction, Wiley-Vch Verlag GmbH & Co. KGaA, Weinheim, **2007**, pp. 147-175.

[66] K. Yu, N. Kumar, J. Roine, M. Pesonen, A. Ivaska, *RSC Advances*, 4 **(2014)** 33120-33126.

[67] K. Shanjiao, G. Yanjun, D. Tao, Z. Ying, Z. Yanying, *Petroleum Science*, 4 **(2007)** 70-74.

[68] M.A. Camblor, A. Corma, S. Valencia, *Microporous and Mesoporous Materials*, 25 **(1998)** 59-74.

[69] P.A. Wright, W. Zhou, J. Perez-Pariente, M. Arranz, *Journal of the American Chemical Society*, 127 **(2004)** 494-495.

[70] A.S. Al-Dughaither, H.d. Lasa, *Industrial & Engineering Chemistry Research*, 53 **(2014)** 15303-15316.

[71] K. Gurholt Evensen, M. Sc. thesis, University of Oslo, **2014**

[72] S. Akbar, *Journal of The Chemical Society of Pakistan*, 32 **(2010)** 592-598.

[73] Q.H. Xia, J. Song, S. Kawi, L.L. Li, *in: Characterization and morphological control of β zeolite synthesized in a fluoride medium,* (Eds.: E. van Steen, I.M. Clay, L.H. Callanan) Studies in Surface Science and Catalysis, Elsevier, **2004**, pp. 195-202.

[74] A. Corma, M.J. Diaz-Cabanas, C. Martinez, F. Rey, *in: Zeolite ITQ-21 as catalyst for the alkylation of benzene with propylene,* (Eds.: A. Gedeon, P. Massiani, F. Babonneau) Studies in Surface Science and Catalysis, Elsevier, **2008**, pp. 1087-1090.

[75] A. Martucci, L. Pasti, M. Nassi, A. Alberti, R. Arletti, R. Bagatin, R. Vignola, R. Sticca, *Microporous and Mesoporous Materials*, 151 **(2012)** 358-367.

[76] F. Bleken, W. Skistad, K. Barbera, M. Kustova, S. Bordiga, P. Beato, K.P. Lillerud, S. Svelle, U. Olsbye, *Physical Chemistry Chemical Physics*, 13 **(2011)** 2539-2549.

[77] S. Teketel, M. Sc. thesis, University of Oslo, **2009**

[78] W. Skistad, S. Teketel, F. Bleken, P. Beato, S. Bordiga, M. Nilsen, U. Olsbye, S. Svelle, K. Lillerud, *Top Catal*, 57 **(2014)** 143-158.

[79] W. Skistad, Ph.D thesis, University of Oslo, **2014**

[80] J. Aguado, D.P. Serrano, J.M. Escola, A. Peral, *Journal of Analytical and Applied Pyrolysis*, 85 **(2009)** 352-358.

[81] M. Bjorgen, S. Kolboe, *Applied Catalysis A: General*, 225 **(2002)** 285-290.

[82] S. Sang, F. Chang, Z. Liu, C. He, Y. He, L. Xu, *Catalysis Today*, 93–95 **(2004)** 729-734.

[83] C.L. S. Bordiga, F. Geobaldo, and A. Zecchina, *Langmuir*, 11 **(1995)** 527-533.

[84] H. Knozinger, S. Huber, *Journal of the Chemical Society, Faraday Transactions*, 94 **(1998)** 2047-2059.

[85] B.H. Ha, D. Barthomeuf, *Journal of the Chemical Society, Faraday Transactions 1: Physical Chemistry in Condensed Phases*, 75 **(1979)** 2366-2376.

[86] V.L. Zholobenko, M.A. Makarova, J. Dwyer, *The Journal of Physical Chemistry*, 97 **(1993)** 5962-5964.

[87] H.P. Boehm, *in: Chemical Identification of Surface Groups,* (Eds.: D.D. Eley, H.P. Paul, B. Weisz) Advances in Catalysis, Academic Press, **1966**, pp. 179-274.

[88] A. Zecchina, F. Geobaldo, C. Lamberti, S. Bordiga, G. Turnes Palomino, C. Otero Arean, *Catal Lett*, 42 **(1996)** 25-33.

[89] M.R. Delgado, C.O. Arean, *Energy*, 36 **(2011)** 5286-5291.

[90] F. Geobaldo, S. Fiorilli, B. Onida, G. Giordano, A. Katovic, E. Garrone, *The Journal of Physical Chemistry B*, 107 **(2003)** 1258-1262.

[91] S. Teketel, W. Skistad, S. Benard, U. Olsbye, K.P. Lillerud, P. Beato, S. Svelle, *ACS Catalysis*, 2 **(2011)** 26-37.

[92] S. Teketel, S. Svelle, K.-P. Lillerud, U. Olsbye, *ChemCatChem*, 1 **(2009)** 78-81.

[93] U. Olsbye, S. Svelle, M. Bjorgen, P. Beato, T.V.W. Janssens, F. Joensen, S. Bordiga, K.P. Lillerud, *Angewandte Chemie International Edition*, 51 **(2012)** 5810-5831.

[94] U. Olsbye, S. Svelle, M. Bjorgen, P. Beato, T.V. Janssens, F. Joensen, S. Bordiga, K.P. Lillerud, *Angewandte Chemie*, 51 **(2012)** 5810-5831.

[95] B.P.C. Hereijgers, F. Bleken, M.H. Nilsen, S. Svelle, K.-P. Lillerud, M. Bjørgen, B.M. Weckhuysen, U. Olsbye, *Journal of Catalysis*, 264 **(2009)** 77-87.

[96] F. Bleken, M. Sc. thesis, University of Oslo, **2007**

[97] W.E. Farneth, R.J. Gorte, *Chemical Reviews*, 95 **(1995)** 615-635.

[98] A. Jentys, J.A. Lercher, *in: Techniques of zeolite characterization*, Introduction to Zeolite Science and Practice, **2001**.

[99] H.G. Karge, *in: Comparative Measurements on Acidity of Zeolites*, (Eds.: G. Ohlmann, H. Pfeifer, R. Fricke) Studies in Surface Science and Catalysis, Elsevier, **1991**, pp. 133-156.

[100] T. Armaroli, L.J. Simon, M. Digne, T. Montanari, M. Bevilacqua, V. Valtchev, J. Patarin, G. Busca, *Applied Catalysis A: General*, 306 **(2006)** 78-84.

[101] J. Kim, M. Choi, R. Ryoo, *Journal of Catalysis*, 269 **(2010)** 219-228.

[102] F. Ngoye, L. Lakiss, Z. Qin, S. Laforge, C. Canaff, M. Tarighi, V. Valtchev, K. Thomas, A. Vicente, J.P. Gilson, Y. Pouilloux, C. Fernandez, L. Pinard, *Journal of Catalysis*, 320 **(2014)** 118-126.

[103] F.M. Dautzenberg, *American Chemical Society*, 411 **(1989)** 99-119.

[104] I.A. Fowlis, *Gas chromatography*, 2nd ed., John Wiley & Sons, **1995**.

[105] H.Y. Tong, F.W. Karasek, *Analytical Chemistry*, 56 **(1984)** 2124-2128.

[106] M. Stocker, *Microporous and Mesoporous Materials*, 29 **(1999)** 3-48.

[107] Z. Wan, C. Wang, H. Yang, D. Zhang, *conference paper, Chemeca 2013: Challenging Tomorrow. Barton, ACT: Engineers Australia*, **(2013)** 885-889.

[108] O. Mikkelsen, S. Kolboe, *Microporous and Mesoporous Materials*, 29 **(1999)** 173-184.

[109] Y. Zhao, F. Wei, Y. Yu, *Chinese Journal of Chemical Engineering*, 16 **(2008)** 726-732.

[110] D. Chen, A. Grønvold, K. Moljord, A. Holmen, *Industrial & Engineering Chemistry Research*, 46 **(2007)** 4116-4123.

[111] A.T. Townsend, J. Abbot, *Applied Catalysis A: General*, 90 **(1992)** 97-115.

[112] R. Zhang, Y. Wang, W. Wu, W.-j. Wang, L.-f. Xiao, G. Wu, *J Fuel Chem Technol*, 40 **(2012)** 1353-1358.

[113] M. Guisnet, P. Magnoux, *Applied Catalysis A: General*, 212 **(2001)** 83-96.

[114] U. Olsbye, S. Svelle, K.P. Lillerud, Z.H. Wei, Y.Y. Chen, J.F. Li, J.G. Wang, W.B. Fan, *Chem Sov Rev*, submitted **(2015)**.